1995

A metallurgical approach toward alloying in rare-earth permanent magnet systems

Daniel James Branagan
Iowa State University

INFORMATION TO USERS

This manuscript has been reproduced from the microfilm master. UMI films the text directly from the original or copy submitted. Thus, some thesis and dissertation copies are in typewriter face, while others may be from any type of computer printer.

The quality of this reproduction is dependent upon the quality of the copy submitted. Broken or indistinct print, colored or poor quality illustrations and photographs, print bleedthrough, substandard margins, and improper alignment can adversely affect reproduction.

In the unlikely event that the author did not send UMI a complete manuscript and there are missing pages, these will be noted. Also, if unauthorized copyright material had to be removed, a note will indicate the deletion.

Oversize materials (e.g., maps, drawings, charts) are reproduced by sectioning the original, beginning at the upper left-hand corner and continuing from left to right in equal sections with small overlaps. Each original is also photographed in one exposure and is included in reduced form at the back of the book.

Photographs included in the original manuscript have been reproduced xerographically in this copy. Higher quality 6" x 9" black and white photographic prints are available for any photographs or illustrations appearing in this copy for an additional charge. Contact UMI directly to order.

UMI

A Bell & Howell Information Company
300 North Zeeb Road, Ann Arbor, MI 48106-1346 USA
313/761-4700 800/521-0600

A metallurgical approach toward alloying in rare-earth permanent magnet systems

by

Daniel James Branagan

A Dissertation Submitted to the

Graduate Faculty in Partial Fulfillment of the

Requirements for the Degree of

DOCTOR OF PHILOSOPHY

Department: Materials Science and Engineering
Major: Metallurgy

Approved:

Signature was redacted for privacy.

In Charge of Major Work

Signature was redacted for privacy.

For the Major Department

Signature was redacted for privacy.

For the Graduate College

Committee Members

Signature was redacted for privacy.

Signature was redacted for privacy.

Signature was redacted for privacy.

Signature was redacted for privacy.

Signature was redacted for privacy.

Iowa State University
Ames, Iowa

1995

To MOM and DAD

TABLE OF CONTENTS

PROLOGUE

"Thus the subject of magnetism becomes of the highest consideration; - in science, as to its mightiness and extent of operation - and in natural theology, as calculated to connect the researches of human intelligence, with Him who hath created these wonders; to elevate the feelings of reverence and adoration in the devotional mind, and to proclaim more clearly, in proportion as these invisible things are understood, 'His eternal power and Godhead'."[1]

William Scoresby 1844

ABSTRACT

A metallurgical approach was developed toward alloying in rare earth permanent magnet systems to allow for microstructural enhancement and control during solidification and subsequent processing. Compound additions of Group IVA, VA, or VIA transition metals (TM) along with carbon were added to the $Nd_2Fe_{14}B$ system (2-14-1). Transition metal carbides will form in the quintary Nd-Fe-B-TM-C system if the phase stability of the precipitates in the alloy is higher than the phase stability of all other phases involving the addit+46Hthe

additive elements and the constituent elements. Transition metal carbide formation was found in the Group IVA (TiC, ZrC, and HfC) and Group VA systems (VC, NbC and TaC). Transition metal carbide precipitates can form at high temperatures in the liquid, during cooling after solidification, or during an appropriate heat treatment. Carbide formation did not occur in the Group VIA system.

The alloying ability of each transition metal carbide system was graded using criteria which dealt with phase stability, liquid and equilibrium solid solubility, and high temperature carbide stability. Titanium with carbon additions satisfied all of the proposed alloying criteria and were chosen as the best system for further study. Titanium and carbon have a significant liquid solubility and an equilibrium solid solubility which was extremely low and below detectable limits. No equilibrium solid solubility means that the titanium and carbon additions will ultimately form TiC after an appropriate heat treatment which allows the development of a composite microstructure consisting of the 2-14-1 phase and TiC. Thus, the excellent intrinsic magnetic properties of the 2-14-1 phase remain unaltered and the extrinsic properties relating to the microstructure are enhanced due to the TiC stabilized microstructure which was found to be much more resistant to grain growth.

When titanium with carbon are dissolved in the liquid melt or solid phases, such as the glass or the 2-14-1 phase, the intrinsic properties of the phases are changed. Favorable intrinsic changes include; large increases in glass forming ability, a significant reduction in the optimum cooling rate, an increase in the optimum energy product, and an enhancement in the nucleation kinetics of crystallization.

GENERAL INTRODUCTION

Dissertation Organization

The thesis begins with a general introduction. In this general introduction section, background information will be given to allow readers, who may not be in the magnetic community but nevertheless have scientific backgrounds, the ability to understand the magnetic properties and the significance of this work to the magnetic industry. The magnetic properties will be defined and the requirements for a magnetic phase to be a permanent magnet will be explicated. A general history of permanent magnetic development will be given to underlay the important advances in the science and industry. Definitions of a materials intrinsic and extrinsic properties are stated in order to set up the approach toward alloying present throughout this work. Additional background information will be given about the material properties and manufacturing methods of NdFeB type magnets. Then a summary of the current permanent magnet industry is given. The coercivity mechanisms will be presented which will help explain the necessary microstructural features for NdFeB magnets made through the rapid solidification route and the powder/sintering route. Following, specific information will be given on the microstructure magnetic property relationships. A quick summary of steel and steel processing will give the reader an appreciation of the possibilities of alloying and metallurgical control. Next, the approach used toward alloying will be explicated to set up the entire paper. In order to satisfy the alloying approach the alloying additions must meet certain requirements which will be identified. The general introduction section concludes with a section on transition metal carbide chemistry which gives general information on the chemistry and physical properties of the transition metal carbides and shows the potential that these additions have for alloy control.

The experimental procedure section deals with the general techniques used in obtaining the data. First the use of a stoichiometric 2-14-1 base alloy is explained in order to best analyze the effects of the transition metal carbide additions. The alloys studied and how the compositions were chosen are explained in the following section. The processing techniques are explicated and the exact processing parameters are given. Then, the characterization techniques are presented according to the physical nature of the measurement. Each part consists of two sections; the first describes the apparatus and the physical property being measured and the second describes the equipment operation and sample preparation techniques.

The main body of this work consists of six parts. Each part deals with the metallurgical approach toward alloying but focuses on a different aspect. First transition metal carbide formation in the 2-14-1 system is shown in PART I. This includes a series of studies evaluating alloy criteria in order to choose the best transition metal carbide system for further study. Based on all available data, TiC additions were chosen as the best system for further study. The remainder of this work (Parts II-VI), focuses on TiC additions to $Nd_2Fe_{14}B$ (2-14-1). Various aspects of the alloying process are looked at in detail including studies of precipitation, studies of solubility, studies of the effects of cooling rate dependance of phase formation, glass forming ability, and crystallization effects. Wherever possible the effects of TiC are contrasted to the effects of Ti and C alone. By this method clear and unambiguous results could be obtained for the effects of TiC addition to the 2-14-1 type magnet.

After the main body, a general conclusion section and an acknowledgment section is given. For additional reference, Appendix A gives information on related papers that have been published or submitted. In this work, all units are given in the centimeter, gram, second (CGS) system. CGS units are used since they are the most common in the

permanent magnet industry. In addition, CGS units offer the advantage of a convenient unit (oersteds) for measuring field strength.

Permanent Magnetic Properties

The search for the *ideal* permanent magnet material continues. For a permanent magnetic material to be technologically successful it must possess a high Curie temperature. The Curie temperature is simply the temperature where the material changes from a ferromagnet to a paramagnet upon heating. Since most applications of permanent magnets are at room temperature or above, the Curie temperature needs to be as high as possible. In addition, due to the temperature dependance of magnetization and the Brillouin Function, the Curie temperature needs to be significantly above the operating temperature. Higher temperature applications of permanent magnets such as in motors or actuators will require materials with increasingly higher values of Curie temperature.

Furthermore, a magnet material must have additional magnetic qualities. After magnetization with an externally applied field, a significant level of magnetization must remain when the field is removed. This property is called remanence and is simply the magnetization remaining after the application of a saturating field. It follows that for a material to have a high remanance it must also have a high value of saturation magnetization. The saturation magnetization is the upper limit of magnetization when all of the magnetic moments are aligned parallel to an applied magnetic field.

Permanent magnets must also have enough coercivity to resist demagnetization. Coercivity is simply the field necessary to reduce the bulk magnetization from the remanent magnetization to zero. Coercivity mechanisms will be talked about in more detail later (see Coercivity Mechanisms) but coercivity is derived from anisotropy. There are many possible modes of anisotropy such as shape, stress and magnetocrystalline

anisotropy. Magnetocrystalline anisotropies can be very large. The anisotropy field can be defined as the maximum field necessary to rotate a magnetic moment from the easy direction to the hard direction of magnetization.

A figure of merit for permanent magnets is the energy product. The maximum energy product is proportional to the largest rectangle that can be drawn in the second quadrant of the demagnetization curve of the B vs H hysteresis loop. This is also called the BH product and can be calculated by the formula: $(H+4\pi M)*H$; where H is the field in Oe and $4\pi M$ is the magnetization in Gauss. The upper limit for the energy product at room temperature is estimated to be 150 MGOe. This is for an alloy consisting of 35% Co and 65% Fe which has the highest known saturation magnetization of 24,500 Gauss.[2] This maximum energy product is estimated from the observed saturation magnetization and the assumption of a square hysteresis loop. The formula for this calculation would thus be $(4\pi M_S)^2/4$; where M_S is the saturation magnetization. In bulk permanent magnets, the microstructure will determine the level of hard magnetic properties actually achieved. Since bulk magnets are always multigrain and multiphase, the above calculation would give only an upper limit for energy product which is usually far above any real measured value.

For a permanent magnetic material to be economically successful, the cost of the magnet must be low. The cost is tied up with the manufacturing and processing costs as well as the cost of the starting elements. Because of the high cost of Co and Ni, Fe based magnets would be the best choice. The *ideal* permanent magnetic material would thus have a high energy product, high Curie temperature, enough coercivity to resist demagnetization and would also be based on iron. The search for this *ideal* permanent magnetic material continues and in the next section, the history of permanent magnetic development will be detailed in this ever ongoing quest.

Permanent Magnet Development

For over 4000 years, the phenomenon of magnetic attraction has been a part of human life. The history of magnetism is entertwined with mysticism, black magic and the occult. In this section, the major advances in permanent magnetic development will be traced. Much progress over time has been made throughout the history of permanent magnets.

The first use of magnets was by the Chinese in approximately 2700 B.C.[3] The first magnetic material consisted of naturally occurring chunks of the ore magnetite (Fe_3O_4). These magnetic rocks later became known as lodestones. Pieces of naturally occurring lodestone were placed on straw and formed a compass when floated in water. This use of permanent magnets in China was chronicled almost two thousand years ago by T'sang Chang.[4]

In western civilization, the use of magnets goes back to the Greek Era. Lucretis of Rome at about 50 B.C. wrote about the lodestone in his book "Nature of Things".[5] The lodestone means waystone and guided sailors to the lodestar.[6] The lodestone was given the name 'Magnes Lapis' because it was commonly found in Magnesia, a district of Thessaly which is now modern day Turkey.[7] Magnes is the root word which later became magnet and magnetism.

The first strong permanent magnets which outperformed the lodestone were made by Servington Savery. His magnets were compound magnets consisting of 37 magnetized steel wires enclosed in a hexagonal bundle and secured with soft iron pole pieces.[6] In the middle 1700's, Gowin Knight achieved fame for his permanent magnets. He further developed the compound magnet. He called it a magnetic magazine. It consisted of two halves, like a horseshoe pattern. Each half consisted of 240 magnets; four magnets long, six deep and ten wide. His magnetic magazine could lift twenty-eight times its own

weight.[6] He also developed a new kind of permanent magnet consisting of iron oxide. He would oxidize pieces of iron fillings in a slurry, mold this into a shape and then bake this in an oven.[7]

In 1867, German handbooks listed a number of magnetic alloys made from nonmagnetic elements. In 1880, it was found that the addition of tungsten to carbon steel increased the permanent magnetic properties. The coercive force increased due to the formation of tungsten carbide.[7] Later chromium was added to steel but although being cheaper was a less effective addition than tungsten. In 1901, in Germany the Heusler alloys were developed which had far better properties than any previous alloys. The typical composition was 10-30% manganese, 9-15% aluminum and the balance was copper.[7] In 1917, cobalt steels or Honda steels were developed in Japan.[8] This magnet was a good magnet material for the time but didn't have many applications because cobalt was so expensive.

In 1932, alloys based on iron, nickel and aluminum were discovered in Japan.[8] A series of AlNiCo alloys were soon developed. In 1934, MK steel was developed by Mishima with the addition of cobalt. It was one third the price of Honda steel and gave better performance with a coercivity more than double that of the cobalt containing steel. This alloy gave improvements in performance due to precipitation hardening after a carefully controlled heat treatment. Pinning sites to domain wall motion are provided by a weakly magnetic nickel-aluminum phase.[9] The magnetic anisotropy was obtained from long rod-shaped grains of iron-cobalt present in the microstucture.[9] This microstructure was further controlled leading to the Ticonal II magnet. This alloy was later optimized in composition and processing to give the Ticonal G magnet. In this alloy, anisotropic properties were obtained by heat treating in the presence of a magnetic field. Further improvements were seen by solidification and grain orientation.[8]

The Alnico type alloys dominated the magnet industry from the mid 1940's to 1970 when ferrite became the most widely used material. The rapid development of these alloys was due to superior properties with excellent metallurgical stability. One disadvantage is the physical properties are poor and they are extremely hard and brittle.[7]

In 1938 in Japan, Kato and Taken made magnets from powdered oxides but they essentially rediscovered Knight's process used 150 years earlier.[7] Due to the development of the Stoner-Wolfarth theory in 1948, it was realized that larger values of magnetic anisotropy was needed to achieve higher coercive forces. A new class of permanent magnet materials was developed in 1952 by Went based on barium oxide.[7] These types of magnets are known as ferrites or sometimes oxide or ceramic magnets. The ferrites are based on the hexagonal oxides of barium or strontium and have the stoichiometry $BaFe_{12}O_{19}$ and $SrFe_{12}O_{19}$ respectively. The ferrites have uniaxial magnetocrystalline anisotropy which allows the development of high coercivity. The hexagonal ferrites have low values of saturation magnetization which limits the maximum energy product to 5 MGOe. Ferrites are produced by powder metallurgy. Strontium ferrite has the highest coercive force and is the largest production ferrite. The raw materials are cheap and nonstrategically located which makes it possible to produce a good magnet at a cheap price.[7] In contrast, at about the same time, platinum cobalt magnets were developed. These magnets had better properties than the ferrites but were so expensive that they were not developed commercially.[9]

After the discovery of the ferrites, investigations were launched on rare earth transition metal alloys. Rare earth (R) transition metal alloys showed great promise due to a combination of properties. The rare earth component due to the anisotropy of the 4f shell, should provide the necessary magnetocrystalline anisotropy. The bulk of the magnetization would then come from the transition metals and their 3d electrons.

Investigations of rare earth transition metal alloys began in the early 1960's by Nesbitt et al and Hubbard et al.[10] The first phase found that had very high magnetocrystalline anisotropy was RCo_5 and was discovered by Karl Strnat et al[11] at the Air Force Materials Laboratory. Later investigations revealed that $SmCo_5$ had the best magnetic properties. In $SmCo_5$ there is parallel coupling between the samarium and cobalt moments. Samarium cobalt has a very high Curie temperature and a low temperature coefficient so it can be used over a wide range of temperatures. Energy products through a powder and sintering process have been obtained in the 16-28 MGOe range.[10]

The R_2Co_{17} phase with a rhombohedral Th_2Zr_{17} structure was also investigated due to the possibility of higher magnetization due to the higher cobalt content. The problem with this material is that the cobalt sublattice has basal plane anisotropy. The anisotropy problem was overcome through a precipitation hardening heat treatment which resulted in bipyramidal particles of 2-17 phase along with a lamellae phase. The high coercivity obtained is achieved by domain wall pinning by the lamellae.[8] Energy products as high as 31 MGOe have been obtained through the development of the two phase cellular microstructure.[10]

A lot of research was done on developing a rare-earth iron binary alloy since the early 1970's. This was driven by the search for cheaper magnets based on iron. Cobalt needed to be replaced due to it's high cost and it's strategically located reserves. The world's most important cobalt producer (Zaïre) was embroiled in a civil war which threatened supplies. No R_2Fe_{17} type alloys were commercially developed. This was because, in the rare-earth iron 2-17 series, the Curie temperatures are all slightly above room temperature. This makes the binary alloys unusable at room temperature and above.

In 1973, Arthur Clark of the Naval Surface Weapons Center studied RFe_2 with R= Tb, Dy, Sm.[11] He found much improved coercivities in alloys crystallized from an

amorphous precursor. In the early 1980s, Norman Koon and Badri Das at the Naval Research Center began a series of studies of rare earth iron alloys through melt-spinning. Since boron was known as a glass forming addition, they studied boron additions to Fe-Tb and Fe-Tb-La.[12,13] About the same time period, Croat et al.[11] at General Motors, worked on binary light rare earth iron or cobalt alloys. In addition, Hans Stadelmaier[11] at North Carolina State University was investigating the ternary light rare earth iron boron alloys. It is said that he began his study after reading a 1979 paper in a Soviet Journal by Lvov Ivan Franko which reported the formation of a new ternary Nd-Fe-B compound with an unknown structure.

Two principle areas of research in the rare-earth iron boron based magnets matured at the same time at the November 1983 29th Annual Conference on Magnetism and Magnetic Materials in Pittsburgh. One processing technique relied on rapid solidification while the other used existing powder and sintering technology present from $SmCo_5$. The rapid solidification work was headed by Croat et al, Koon and Das, Hadjipanayis et al, Selmyer et al, and Becker.[10] The powder and sintering route was headed by Sagawa.[10]

The $Nd_2Fe_{14}B$ phase has currently the highest measured value of energy product than any material known. Fuerst et al.[14] reported an energy product of 48.5 MGOe in die upset samples. Sagawa et al.[15] have reported an energy product of 50.6 MGOe in sintered samples.

As shown, there has been a steady progress in property development over the years with an almost logarithmic increase in energy product in recent times (Figure 1). Research continues on developing ternary and higher order iron based magnetic phases. Since 1987, much effort has been on developing the $R(Fe_{1-x}M_x)_{12}$ phase. The $SmTiFe_{11}$ phase has shown the most promise with a Curie temperature of 600K but it is limited by a low saturation magnetization.[16] In 1990, Coey and Sun showed that R_2Fe_{17} compounds

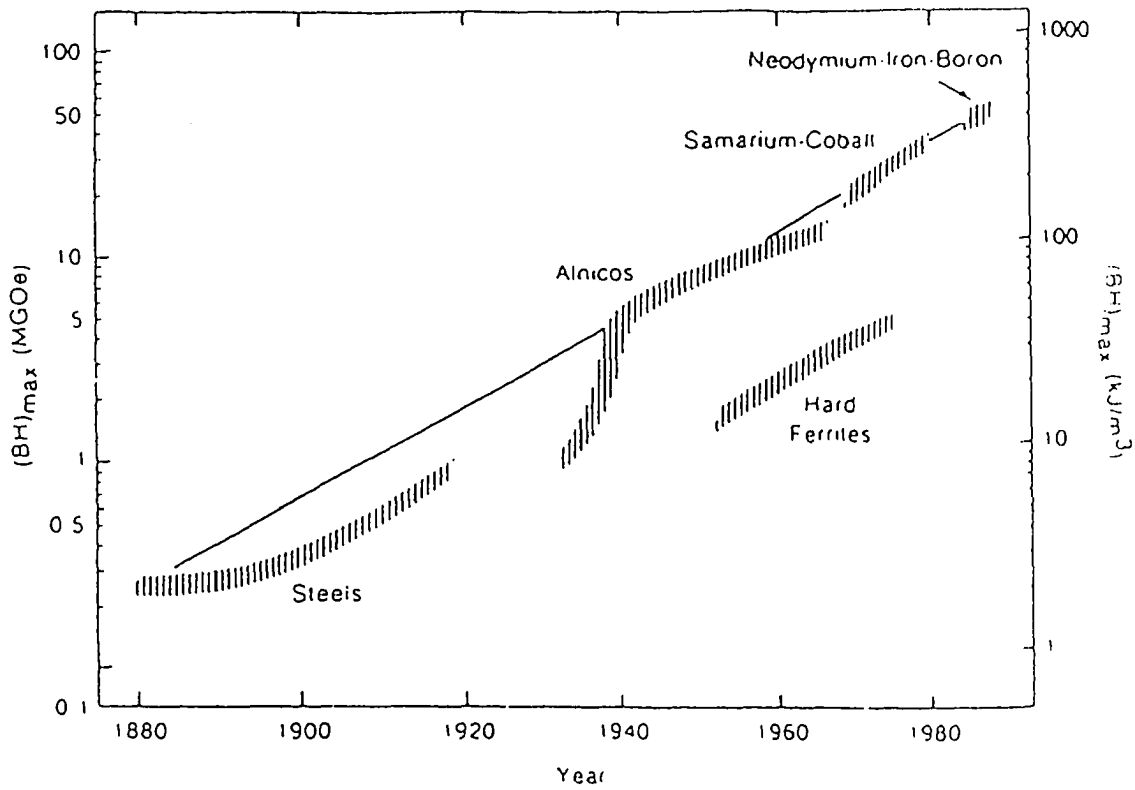

Figure 1 The progress in property development of different magnet materials. The increase in the energy product in years shows a logarithmic increase.[10]

could absorb nitrogen if heat treated at 500°C in gaseous N_2 or NH_3.[17] Since that time, various researchers have worked on nitriding the 2-17 and 1-12 structures. In the $Sm_2Fe_{17}N_X$ compound, nitrogen absorption increases the Curie temperature from 395K to 747K.[18] This increase in Curie temperature is due to an increase in the nearest Fe-Fe distance from the expansion of the unit cell volume. Also nitrogen absorption changes the magnetocrystalline anisotropy from planar to uniaxial. Both of these effects make $Sm_2Fe_{17}N_X$ a technologically viable compound. Other researchers have diffused nitrogen into the $SmTiFe_{11}$ and $NdTiFe_{11}$ compounds and have found similar results.[16,18]

Another area of current research is in isotropic high remanence permanent magnets.[19,20] The magnetic properties arise from a magnetic coupling between the soft magnetic phases Fe_3B and α-Fe with the hard magnetic $Nd_2Fe_{14}B$ phase. Since α-Fe has a very high saturation magnetization of 21,580 Gauss[21], this leads to the development of high remanence magnets more suitable for electric motor applications. Energy products of 14.5 MGOe have been obtained with remanences as high as 11,500 Gauss.[20] Continued research is necessary to develop the optimum microstructure to improve the coercivity.

Intrinsic vs. Extrinsic Properties

The properties of a material can be broken down into two broad categories; intrinsic and extrinsic properties. Intrinsic properties are properties related to the crystal structure of a specific phase. In permanent magnets, the intrinsic magnetic properties would include magnetocrystalline anisotropy, saturation magnetization, and Curie and spin reorientation temperatures. The intrinsic magnetic properties thus determine the potential of a magnetic phase as a permanent magnet. As mentioned earlier, from the saturation magnetization the maximum energy product can be estimated.

Extrinsic properties are properties dependant on the microstructure. Thus the extrinsic properties are very sensitive to processing conditions. Extrinsic magnetic

properties would include susceptibility, permeability, coercivity, and the energy product. One may ask why the extrinsic properties are important at all if the maximum magnetic properties are determined by the intrinsic properties. However, no commercial permanent magnet is single phase or single crystal, and thus the bulk magnetic properties are controlled by the microstructure. The percentage of the optimum energy product actually reached in a permanent magnet on a bulk scale will depend on the microstructure. Thus, the intrinsic properties of a hard magnetic phase determine the potential of the phase for permanent magnet applications while the microstructure determines the level of the properties that are actually achieved in a bulk magnet.

Material Properties - $Nd_2Fe_{14}B$

Since the discovery of $Nd_2Fe_{14}B$ (2-14-1) a short 10 years ago, it has developed rapidly into a technologically important material. It's rapid development is due to very favorable magnetic and economic properties. The crystal structure of the $Nd_2Fe_{14}B$ phase is shown in Figure 2.[22] The structure is stabilized by trigonal prisms with boron as a central atom (Figure 3).[22] The unit cell is tetragonal with a $P4_2/mnm$ space group. There are four formula units per unit cell for a total of 68 atoms. It is important to note that there are 6 crystallographically inequivalent iron sites, 2 inequivalent neodymium sites and 1 type of boron site.

What gives the $Nd_2Fe_{14}B$ phase high potential as a permanent magnetic material is it's intrinsic properties. It has an extremely high anisotropy field of 73,000 Oe at 295K.[23] This allows the potential to develop high coercivity. In $Nd_2Fe_{14}B$, the total angular momentum of the 3d electrons of the iron and the 4f electrons of the neodymium couple in a parallel fashion. This parallel coupling allows a high saturation magnetization of 16,200 Gauss.[24] This gives the phase a potential maximum energy product of 65.6 MGOe.

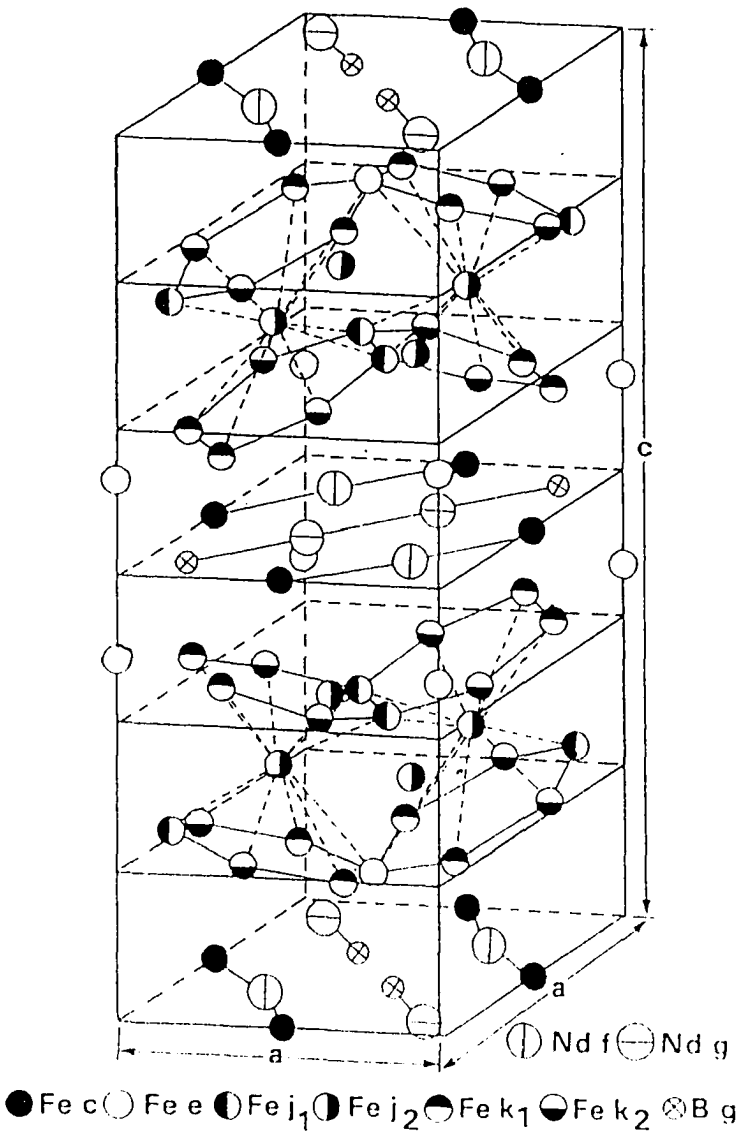

Figure 2 The tetragonal unit cell of the $Nd_2Fe_{14}B$ phase with a $P4_2/mnm$ space group.[22]

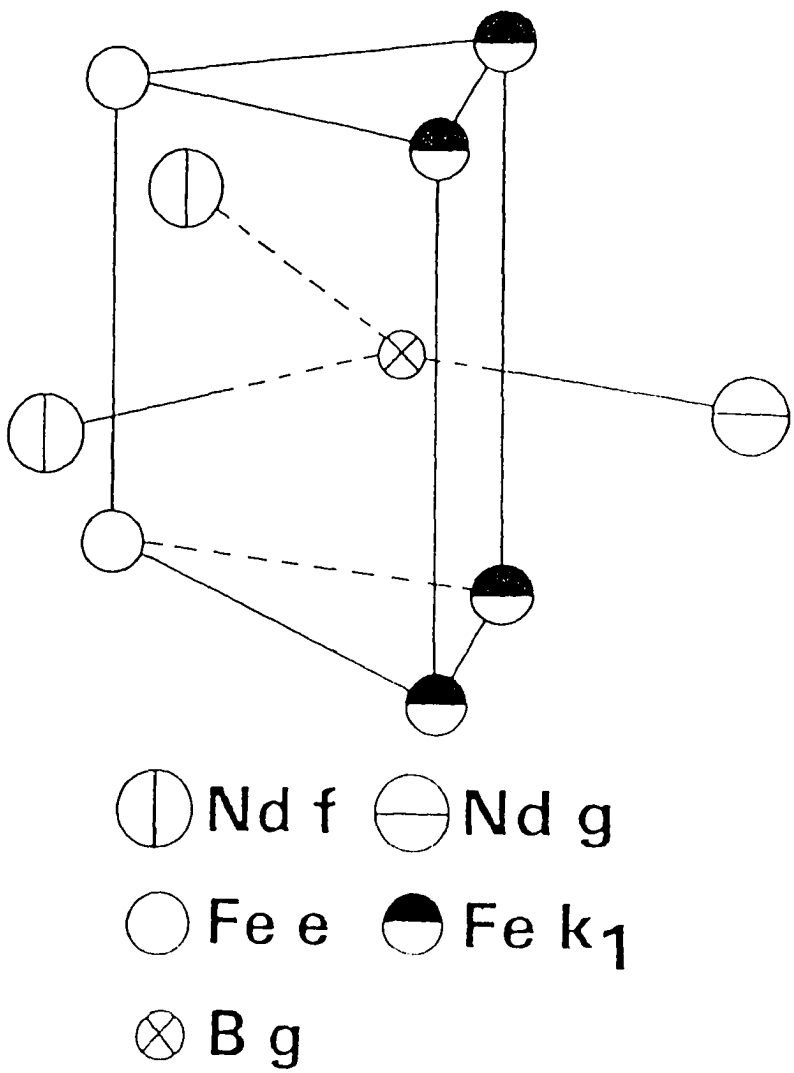

Figure 3 A trigonal prism that is located in the crystal structure of the $Nd_2Fe_{14}B$ phase. The boron atom stabilizes the unit cell and the hexagonal iron nets.[22]

What makes the material technologically important is the cost and abundance of the starting materials. The 2-14-1 phase consists of approximately 72 wt% Fe which is very cheap and nonstrategic. Neodymium while being a rare earth element is still more abundant than many common metals such as niobium, lead, tin, and silver. In addition, neodymium is 5 times as abundant as samarium. Boron is expensive but is used in only small amounts. It is important to note that only 10 to 25% of the cost of NdFeB type magnets is from the starting elements themselves.[25] Processing is still the biggest cost of the magnet.

The $Nd_2Fe_{14}B$ phase is not the *ideal* hard magnetic material. It has a low Curie temperature of 312°C.[26] In addition, it has a high temperature coefficient of coercivity (-0.86 %/°C).[27] Both of these effects limit the maximum operating temperature to 120°C.[28] In addition, the 2-14-1 phase is extremely hard and brittle which limits processability. Also, since it contains neodymium, the 2-14-1 phase is susceptible to corrosion and must be protected in service.

Manufacturing Methods

There are two important commercial manufacturing methods for making $Nd_2Fe_{14}B$ type permanent magnets. One route involves a powder metallurgy process. This process was first utilized for the Sm-Co type magnets. The first step is to vacuum cast the alloy. The ingot is then milled and ground into approximately 3 μm sized powders. Due to the large initial grain size in the ingots, the ground powder particles are essentially single crystal. The particles are next aligned in a magnetic field of approximately 1 Tesla.[15] The C-axis which is also the easy axis aligns parallel to the applied magnetic field. The aligned powder is then cold compacted with 200 MPa pressure to approximately 70 % density so that their is enough particle to particle contact to prevent rotation.[15] The

magnet part is then sintered at approximately 1100°C in an argon protected atmosphere to full density. Usually a post heat treatment in the 700° - 900°C range is necessary to get the proper grain boundary phases.[29] The final microstructure is very anisotropic with grain sizes between 5 to 10 μm.[29] Energy products of 50.6 MGOe have been achieved through this powder metallurgy process by Sagawa et al.[15]

The second general processing route is rapid solidification. Rapid solidification processing (RSP) is done by melt-spinning or gas atomization. Melt-spinning has been the most commercially successful so far but the gas atomization approach may allow for cheaper production and larger batches. The RSP technique offers some advantages. First of all, the microsegregation occurring during solidification from the peritectic and eutectic reactions can be avoided. This allows the production of a uniform glass if overquenched or a nanograin sized polycrystalline material if optimally quenched. The microstructure and grain size are very sensitive to the cooling rate which can be controlled by varying the wheel tangential velocity during melt-spinning. The melt-spinning process will be described in more detail in the experimental section.

After melt-spinning, the melt-spun ribbon can be processed into a magnet in many ways. One method is to form bonded type magnets. The ribbons are first coarsely ground to 150 μm diameter and are mixed with an epoxy. Bonding can occur by mixing the ribbons with a dry epoxy before pressing or by impregnating a liquid epoxy under vacuum after pressing. The ribbons can also be mixed with epoxy and compression or injection molded which gives excellent shape control. Gas atomized powder due to its spherical shape would be an excellent feedstock for this approach. The maximum density in bonded magnets is 85 % due to the highly anisotropic packing of the flat ribbons.[30] This along with the isotropic nature of the grains within the ribbons limits the maximum energy product to about 9 MGOe.[30]

Melt-spun ribbons can also be processed thermomechanically. This is done by hot pressing or hot extruding. One hundred percent density can be obtained through the simultaneous application of heat and pressure. Grain growth during consolidation can be a problem. A typical hot pressing cycle would start with overquenched material hot pressed at 725°C for 2 minutes at 20 ksi.[30] Approximately 10 % alignment is possible which leads to energy products between 10 to 20 MGOe.[30]

A third method of processing is called die upsetting. The first step involves hot pressing to full density followed by a second hot press in a die having a greater diameter. Typically magnets are die upset from 50 to 70 % of their original thickness which causes bulk lateral plastic flow.[31] Grain rotation, grain boundary sliding, and boundary migration cause an approximate 85% alignment.[31] This level of alignment gives a remanence over 14,000 Gauss which is close to 90% of the saturation magnetization. Energy products through this route have obtained up to 48.5 MGOe.[14]

Permanent Magnetic Industry

This section will attempt to give a brief overview on the current large and growing permanent magnet industry. In the last twenty years, new materials such as the Sm-Co and the Nd-Fe-B type magnets have begun to revolutionize the industry. Since these new types of materials utilize lanthanides it is important to first examine the rare earth industry.

The US Bureau of Mines estimates the world's reserves of rare earths to be 45 million tons.[32] This large amount of reserves should last 400 years at the current rate of consumption. The largest amount of rare earth containing ores are located in China which has 75 % of the worlds reserves. The USA has 13% of the world's reserves followed by India and Australia at 4% and 1.5% respectively.[32] The main suppliers of rare earths are Molycorp in the USA and Rhone-Poulenc in France. Other suppliers are located in Japan

and China. Rare earths are currently being used in many types of industries including the optic, magnetic, electronic, ceramic, glass, catalysis, and steel industries. Currently the world's annual capacity to produce rare earths is 70,000 tons of rare earth oxide which is an oversupply of 50%.[32] Since neodymium and samarium are present in large amounts in rare earth containing ores, the expansion of the magnetic industry is not limited by the availability of these elements.

There are four major types of permanent magnetic materials currently being produced. These four types and their percent usage are ferrite (59.9%), NdFeB (17.3%), ReCo (11.1%), and AlNiCo (9.2%) with the remaining 2.3 % in other types of magnets such as Fe-Cr-Co and Mn-Al-C.[33] A figure of merit for judging the different materials is the cost of the magnet material per joule of energy that it supplies (Figure 4). It can be seen that ferrite is by far the cheapest hard magnetic material. Another factor is the weight and size reduction possible from utilizing magnets with a higher energy product. The mass of magnet material required for one joule of energy supplied from the various permanent magnet materials is shown in Figure 5.[34] NdFeB type magnets give the best savings in weight per joule of energy supplied.

Ferrite magnets are expected to continue to dominate the industry because of their low cost. They are currently experiencing an annual growth rate of 9%.[35] For high energy applications, the rare earth based permanent magnets will be the material of choice. NdFeB magnets are cheaper to produce than Sm-Co type magnets and are replacing Sm-Co in many applications. Currently, sintered NdFeB represents roughly 75% of the NdFeB produced.[25] The NdFeB marketplace is growing at the rate of 17.5% annually.[35] In addition, the cost of production of NdFeB type magnets is going down from an average price of 125 $/lb in 1987 to 85$/lb in 1992.[34] They have a projected cost of 65 $/lb in 1997.[34] By the year 2000, NdFeB type magnets are expected to be worth

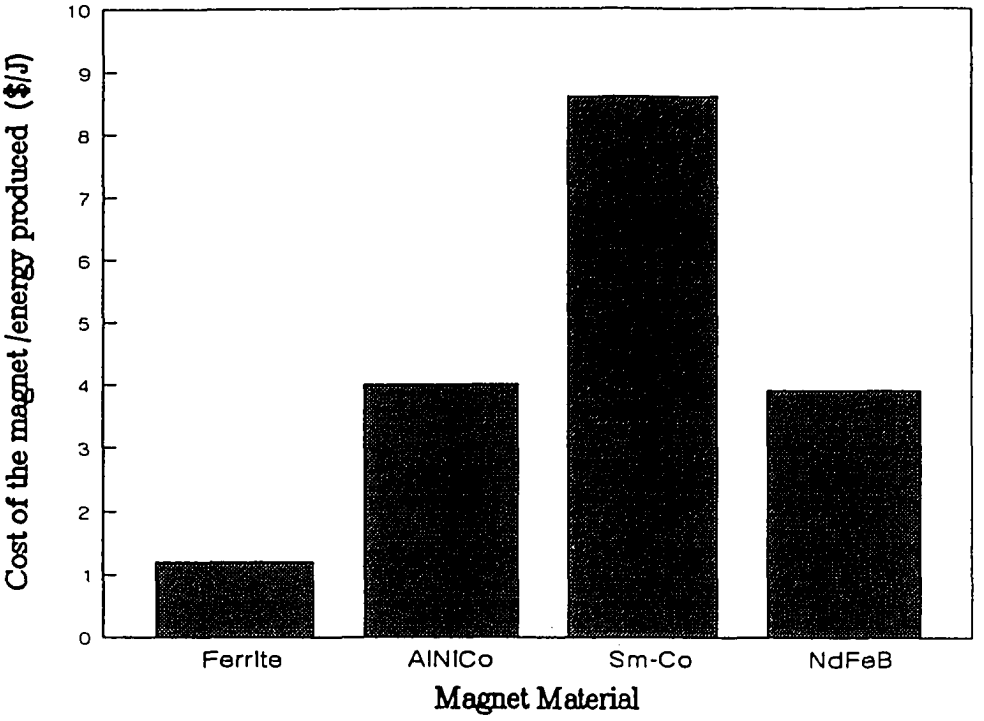

Figure 4 The cost of the magnet material per energy produced for the most common types of magnet materials.[34]

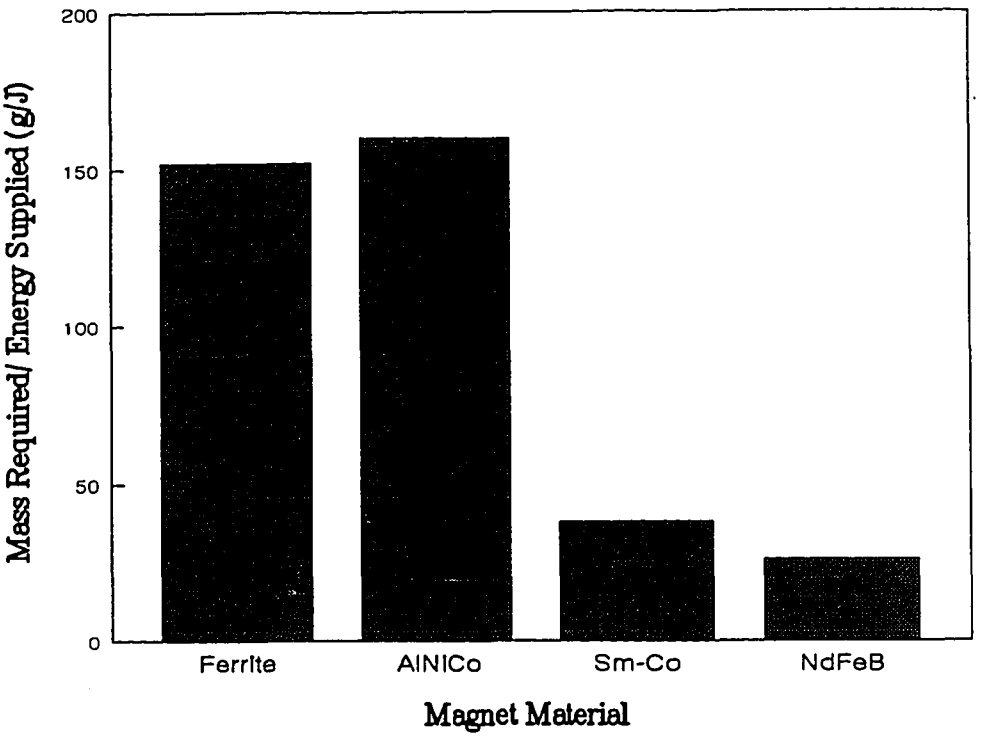

Figure 5 The mass required per energy supplied for the most common types of magnet materials.[34]

2.7 billion dollars annually[33] and are expected to capture 40 % of the total magnet market.[34] The Sm-Co marketplace is in decline but will continue to be the material of choice for high energy applications at elevated temperature. The AlNiCo type magnets are also in decline due to the development of NdFeB and the fluctuation of the Co and Ni markets. It will continue to be the material of choice for high temperature sensors and instruments due to its low temperature coefficient.[36]

The USA magnetic market is experiencing a 10.9% annual growth which is projected to be worth 763 million in 1997.[35] The world magnet marketplace is growing rapidly as well and is expected to be worth 6.5 billion by the year 2000.[33]

The largest market for permanent magnetic materials is in electromechanical devices. In 1990, 40% of the permanent magnets produced were utilized in motors and generators.[34] Other significant uses were actuators in data technology (20%), acoustic devices (15%), magnetomechanical devices (10%), beam control systems (10%), and nuclear magnetic resonance systems (5%).[34] The effect to which NdFeB type magnets will permeate the various marketplaces remains to be seen. Even though NdFeB is significantly more expensive than ferrite, a complete cost analysis must consider the savings from design simplification and the reduction in size and weight of the associated components. There is projected to be considerable growth in the development of high or variable speed motors for the pump, fan, and compressor industries.[35] The electric motor demand for permanent magnets overall is experiencing a 15% annual growth due to the increasing need for small and lightweight electric motors in the automobile and other industries.[36] Other rapidly developing applications include headphones, loudspeakers and disk drives.

Coercivity Mechanisms

As mentioned earlier, coercivity is an important property of a permanent magnet. Without significant coercivity, the magnet would be easily demagnetized and therefore would not be useful. A ferromagnet can reverse its direction of magnetization in one of two modes; continuously or discontinuously. A change in the direction of magnetization in a continuous fashion occurs through coherent or incoherent rotational processes. A discontinuous change in magnetization occurs through domain processes. Domain processes may depend on either domain nucleation or domain growth. The level of coercivity measured in a magnetic material is always determined by the mechanism which occurs at the lowest field energy.

In order to have coercivity, the magnetic material must have anisotropy. There are three main types of anisotropy; magnetocrystalline, shape, and stress anisotropy. The most important types for permanent magnets are shape and magnetocrystalline anisotropy. The important coercivity mechanisms for magnets with shape or magnetocrystalline anisotropies will next be explained.

Shape anisotropy comes from the bulk shape of the magnetic material. It is related to the ratio of the length to the width of the particle. In the presence of a magnetic field, the magnetic moments will want to lie along the long axis due to a smaller demagnetization field. To develop significant coercivity from shape anisotropy, the particles must have a fine size to exclude the possibility of domain processes. Kittel and Galt[37] have calculated the coercive force for coherent rotation of a prolate spheroid. The coercive force is equal to; $Hc = (N_t - N_o)M_s$ where N_t and N_o are the demagnetization factors for the narrow and long directions respectively. Experimental coercivities are always found to be much less than that predicted from the above model of coherent rotation. This may be due to the activation of incoherent rotation modes such as fanning, curling, or buckling which require

less field energy. Depending on the particle size and distribution, interactions between particles and domain processes may be additional factors reducing the coercive field in shape anisotropy type magnets.

Magnetocrystalline anisotropies arise from the difference in energy between the easy and hard magnetization directions. The origin of magnetocrystalline anisotropy is mainly from spin-orbit coupling. When an external field is applied, the spin moments try to align but are constrained by the orbital motion of the electrons. The orbital motion is strongly coupled to the lattice. The energy of the spin-orbit coupling must be overcome in order to change the direction of magnetization.[38] Magnetocrystalline anisotropies can be very large especially for rare earth containing materials.

W.F. Brown in 1945[39], showed that if coherent rotation is the only mechanism occurring for a material with uniaxial magnetocrystalline anisotropy then the intrinsic coercivity would equal the anisotropy field. The intrinsic coercivity is given by; $H_{ci} = H_a - N(4\pi M_s)$ where H_{ci} is the intrinsic coercivity, H_a is the anisotropy field and N is a demagnetization factor. The theoretical nucleation field, which is the field which must be overcome before the start of coherent rotation would thus equal; $H_n = 2K_1/(4\pi M_s)$ where K_1 is the uniaxial anisotropy constant.

Stoner and Wohlfarth[40], extended Brown's theory to any material in single domain form that has shape or magnetocrystalline anisotropy. They assumed an isotropic and noninteracting assembly of single domain particles. Depending on the angle of the applied field to the anisotropy, they developed model hysteresis curves which represented combinations of coherent and incoherent rotation.

In real materials, the coercivity is always found to be much less than the theoretical nucleation field. This is often called "Brown's Paradox". As pointed out by Chikazumi[41], incoherent rotation processes can only occur for materials in which the

principle anisotropy is from shape anisotropy. Therefore, in materials with very high magnetocrystalline anisotropies, magnetization reversal is occurring by domain processes. Either domain nucleation or domain growth can be the limiting factors determining coercivity.

Domain nucleation occurs first in areas that contain chemical or physical defects. Chemical defects can arise from impurity soft magnetic phases that have lower magnetocrystalline anisotropies. Physical defects, which are sites for demagnetizing fields, can occur from physical irregularities occurring on oddly shaped grains, from dislocations, or from phase boundaries. Nucleation controlled coercivity can be increased by minimizing the number of defect sites. This is most easily done by subdividing into small regions. In bulk magnets, this is achieved by reducing the grain size. The smaller the grain size the less the probability that any given grain will contain any defects.

If the grain or particle size is reduced to very small proportions, a single domain particle can be formed. The single domain grain or particle size can be calculated from a balance of energies. A small particle that suddenly contains two domains will experience a decrease in the magnetostatic energy but will also experience an increase in the domain wall energy. The critical single domain grain size can be calculated from the saturation magnetization and the domain wall energy (Γ) by the relation; $D_c = 1.48\Gamma/(4\pi M_s)^2$.[42] Thus, in the absence of an applied field, a particle or grain with a diameter below D_c would be single domain. It is important to note that in the presence of an applied field, domain processes can and do occur even in these single domain particles.[43]

Domains once nucleated, can be prevented from growing by an interaction with defects. These defects are often second phase particles which can interact and pin the domain walls due to a reduction in total amount of wall energy. The most effective defects must have a size within the same order of magnitude of the domain wall thickness. The

coercivity in pinning controlled magnets will depend on the distribution and size of the pinning centers and on the flexibility of the domain walls.

Microstructure / Magnetic Property Relationships

There is much discrepancy and controversy about the exact mechanisms determining the coercivity of NdFeB type magnets. It is apparent that the fundamental origin of coercivity comes from the large magnetocrystalline anisotropy of the $Nd_2Fe_{14}B$ phase (73 KOe at 295 K)[23]. However the maximum coercivity achieved in aligned NdFeB type magnets is approximately 20 KOe.[10] This is a reduction by more than a factor of three then predicted by the theoretical nucleation model. Obviously, other coercivity modes besides coherent rotation are taking place. This fact underlies the importance of domain processes.

Differences exist in the microstructures found in NdFeB type magnets produced by the melt-spinning and sintering routes. In sintered magnets, 80 to 85 vol% of the magnet is made up of 2-14-1 phase while in melt-spun (Magnequench) magnets over 95 % of the volume is 2-14-1 phase.[44] The single domain particle diameter is found to be 0.3 μm.[42] In sintered magnets the ideal grain sizes are found to be between 10 to 20 μm which is significantly above the single domain particle diameter. In melt-spun magnets, the ideal grain diameter is found to be between 0.02 to 0.1 μm which is below the single domain particle diameter. Therefore significant microstructural differences exist between the magnets produced by the two different manufacturing processes which could lead to differences in domain processes.

Most researchers[10,26,41] agree that the prevailing coercivity mechanism in sintered magnets is one that is nucleation controlled and domain wall pinning is only a minor mechanism. The ideal microstructure for sintered magnets would be one that inhibits the

nucleation of reverse domains. The grain size needs to be small (10μm) because larger grains have a greater amount of surface area and a greater probability of defects. Chemical defects include impurity soft magnetic phases and physical defects such as misaligned or oddly shaped grains. In addition a nonmagnetic rare-earth eutectic phase should surround each grain. This grain boundary phase magnetically insulates each grain to prevent the nucleation of one grain from spreading to adjacent grains. Further microstructural improvements of sintering magnets will focus on reducing the number of defects, reducing the post sintering grain size, and reducing the magnetic coupling between the grains.[45]

The mechanisms of coercivity in melt-spun material are much less clear. There is much evidence to support a pinning controlled coercivity in which the domain walls are contained in and are pinned by the grain boundaries. There are differences in the initial magnetization curves of pinning and nucleation controlled magnets. In nucleation controlled magnets, after thermal demagnetization, the initial susceptibility is high since the existing domain walls can move easily. In pinning controlled magnets, after thermal demagnetization, domain walls are pinned and cannot move easily, which leads to a low initial susceptibility until fields approaching coercivity are reached.

In melt-spun ribbons of NdFeB type magnets, the initial susceptibilities are much lower than in sintered magnets of the same type. In addition, in melt-spun ribbons, coercivity only develops at high applied fields. Both of these factors favor a strong pinning model.[46,47,48] However, many other researchers[49,50], have obtained evidence favoring a nucleation controlled coercivity. However, the coercivity mechanisms of nucleation control and pinning control are not entirely independent. For instance, in a nucleation controlled magnet, pinning of domain walls does occur. Otherwise, a reverse domain once nucleated would sweep across the entire magnet. Livingston[51] pointed out

that coercivity models based on domain wall pinning at the grain boundaries and nucleation models are very difficult to distinguish experimentally.

Regardless of the exact coercivity model, the following quote by F.E. Pinkerton addresses the magnetization behavior in melt-spun magnets:

'Single-domain behavior provides the starting framework for describing the magnetization, but it must be modified to include domain wall motion and magnetic interactions between grains.'[52]

In magnequench melt-spun ribbons, the optimum grain size is found to be approximately 30 nm which makes the grains single domains.[44] The grains are found to be isotropic and have a polyhedral shape. Single domain grain size means that in the absence of an applied field, it is energetically unfavorable for the grains to have domain walls. However, during the application of an applied field the magnetization and demagnetization processes occur through the movement of domain walls. The domain walls are pinned during all stages of sample magnetization at the grain boundaries. Since there are little or no defects within the grains, once a reverse domain is nucleated, it sweeps right across the grain. Upon demagnetization each domain reverses as a unit. The demagnetization process occurs by reversing one grain or at most a small group of grains at a time.[52] An intergranular phase 2 nm thick surrounds the grains.[44] This intergranular phase is usually amorphous and helps to magnetically decouple adjacent grains.

Steel Analogy

The following definition by Tom E. Scott is for steel.

"Any iron-based alloy in which no other single element is present in excess of 30 weight percent and for which the iron content amounts to, at least, 55 weight percent and carbon is limited to a maximum of 2 weight percent."[53]

The hard magnetic $Nd_2Fe_{14}B$ phase consists of 72 wt% Fe, 27 wt% Nd, and 1 wt% B. Thus, the 2-14-1 phase fits the very definition of steel. Since the 2-14-1 phase is a ternary tetragonal compound and is not based on one of the allotromorphs of iron, it may not truly be considered a steel. However, the analogy is useful because it gives a different perspective on the material. This viewpoint of treating the 2-14-1 system as a steel system is used throughout this work.

Steels are the most technology important material and more is known about the properties of steel than any other material. Through an appreciation and a proper understanding of steel and steel processing, many other systems could be better understood. There are many intricate games played with alloying and processing. Also, in the steel industry the entire gambit of processing techniques available to materials are utilized.

After solidification and homogenization, the first step in the heat treatment of steels is usually austenization. Austenization is a high temperature heat treatment which transforms the bcc iron phase (ferrite) into the fcc iron phase (austenite) and dissolves the bulk of the iron carbides and alloy carbides. Upon subsequent cooling, the equilibrium microstructure will consist of cementite (Fe_3C) and α-Fe. However, the distribution, sizes, morphologies and the orientation relationships of these phases will determine the properties. The same steel alloy can be made soft and ductile or hard and brittle simply by varying the cooling rate or cooling cycle after austenitization.

The science of steels is developed to a level which not only gives the phases specific names but also microstructures specific names as well. Pearlite, upper and lower bainite, martensite and combinations of these microstructures are only a few of the possibilities. Time, temperature, transformation (TTT) and continuous cooling transformation (CCT) diagrams have been developed to trace the formation of specific phases and combinations

of specific microstructures under controlled processing conditions. Through utilizing the knowledge gained in the 2000 year old history of steels, other industries including the permanent magnetic industry could benefit greatly.

Alloy Theory

The alloying theory used in this work involves both intrinsic and extrinsic effects through precipitation and compound formation. Many researchers[54-58] have studied the intrinsic substitution of elements for the Nd, Fe, or B sites. Many gains have been made through intrinsic substitution but most have centered on the optimization of certain properties or processing conditions. Intrinsic substitution ultimately involves a tradeoff of properties. That is, enhancing one property comes at the price of decreasing another. The approach used in this work is entirely different because it involves compound additions of at least two elements. These elemental additions consist of a Group IVa, Va, and VIa transition metal along with carbon. Thus, alloying involves adding two elements together that will form stable compounds while maintaining the formation of the 2-14-1 phase.

When the transition metals and carbon are dissolved in the liquid or solid phases, the intrinsic properties of these phases are changed. If they exist in the phase in a supersaturated condition, transition metal carbide precipitates can be formed. Getting the added elements into the liquid is done by simply raising the temperature until melting occurs. Getting the added elements into supersaturated solid solution is achieved through solidification. Solidification is always a nonequilibrium process. Depending on the cooling rate, elements can be trapped in the solidified phase or lattice since diffusion out of a phase is very time dependant as well as temperature activated. Through rapid solidification, crystallization can be avoided, and solid solubility can be extended.

The transition metal carbide precipitates can form at high temperatures in the liquid, during cooling after solidification, and during heat treatment. The carbides formed in the liquid are called primary carbides. The carbides formed during cooling after solidification and during heat treatment are called secondary carbides. They are usually similar in size and nature. If the solid phase contains dissolved transition metals and carbon in a supersaturated nonequilibrium condition, additional precipitation will occur during an intermediate temperature heat treatment. Carbide precipitation occurs at faults in the microstructure and almost always heterogeneously. Precipitation sites would include phase boundaries, grain boundaries, dislocations, twins etc. Due to the large amount of grain boundary area per unit volume, the grain boundaries are generally the principle sites for precipitation.

The ideal transition metal carbide system would have no equilibrium solubility in the 2-14-1 phase. Then all of the dissolved transition metal and carbon could be precipitated out from supersaturated solid solution. Thus, the ideal equilibrium microstructure would be a composite consisting of 2-14-1 phase and transition metal carbide. Then, the excellent intrinsic magnetic properties of the 2-14-1 phase would be retained while the extrinsic properties of the material would be enhanced due to a carbide stabilized microstructure.

Alloying Requirements

In order to utilize this approach toward alloying, the transition metal and carbon additions must meet certain requirements. The first requirement is that the additions must form transition metal carbides. If no carbides form then this proposed alloying approach can not work. In addition, the phase stability of the precipitates in the specific multicomponent system must be higher than the phase stability of the phases involving the

additive elements and the constituent elements. If any additional phases form with Nd, Fe, or B, the amount of 2-14-1 phase will be reduced which will cause a decrease in the hard magnetic properties. The elemental additions should also have significant solubility in the liquid melt at high temperatures. If the additions have no liquid solubility or if they form immiscible liquids then their ability to affect the subsequent microstructure will be low. Furthermore, the elemental additions should have significant and only nonequilibrium solubility in the 2-14-1 phase. Significant solubility is necessary so that the additions can be precipitated out of supersaturated solid solution. Only in this way can an effective dispersion of precipitates be formed able to prevent grain growth. Only nonequilibrium solubility is desired so that the total amount of dissolved additions can be precipitated out of the 2-14-1 phase leaving the excellent intrinsic magnetic properties of the 2-14-1 phase unaltered. Moreover, the precipitates that form must be stable to high temperatures and should resist coarsening and dissolution. This is so grain growth can be prevented at high temperatures which allows elevated temperature processing such as hot pressing or hot extrusion.

Transition Metal Carbide Chemistry

As stated in the previous sections, in order for the transition metal carbide to be successful as alloying additions to the 2-14-1 system they must meet certain solubility, stability, and physical metallurgical requirements. In order to appreciate the potential of the transition metal carbides as alloying additions, this section attempts to give a brief study of some of their most important properties. The transition metal carbides are an important class of compounds with some very interesting physical, electrical and mechanical properties. The focus of this paper will be for titanium carbide (TiC) for reasons that will become apparent later in the main body of this work.

Most transition metal carbides belong to a class of compounds called Hägg compounds. Hägg found that the structure of metal carbides (as well as borides, nitrides and hydrides) is determined by the radius ratio of the interstitial atoms to the transition metal atoms.[59] He found that usually if this ratio is less than 0.59 then simple structures are formed. If the ratio is greater than 0.59 then complicated structures result.

The crystal chemistry of transition metal carbides is complex due to their defect structure. Deviations from stoichiometry are far more common than stoichiometry. The compounds of transition metal carbides and their exothermic heats of formation can be seen in Table 1. Most of these carbides have simple structures such as hexagonal or cubic (B1). TiC has the B1 or rock salt structure. It is face centered cubic with a Fm-3m space group. TiC is stable over a wide range of interstitial weight fractions which illustrate the possible nonstoichiometric defect structure.

Carbides have extremely high melting points which are usually greater than the transition metal itself (Figure 6). Only the Group VIA transition metal carbides have melting temperatures lower than their respective transition metal. Because of these high melting points, they are often referred to as refractory carbides. High melting points are an indication of the strength of the bonding. The bonding in transition metal carbides is complex and not completely understood. There is localized metal to metal and metal to nonmetal interactions. These localized bonds have both covalent and metallic character with a small amount of ionic character. The most recent theories for bonding in these compounds take into account strong metal to metal and metal to nonmetal bonds.

Transition metal carbides are used in steels and cemented carbides because of their extreme hardness. Their hardness values vary between 1300 to 2900 Kg/mm^2.[59] TiC is extremely hard with a microhardness of 2900 Kg/mm^2. In addition, the carbides retain their strength up to very high temperatures. An important mechanical property of

Table 1 Transition Metal Carbide Phases and Standard Enthalpies of Formation

Carbide (MC)	$-\triangle H_f°$ (kcal/g-at)	Reference
TiC	22.0	61
ZrC	24.2	61
HfC	30.0	61
V_2C	11.7	62
VC	12.0	62
Nb_2C	15.1	61
NbC	16.6	61
Ta_2C	17	61
TaC	18	61
$Cr_{23}C_6$	3.0	1
Cr_7C_3	3.9	61
Cr_3C_2	3.9	61
Mo_2C	3.6	61
Mo_3C_2	----	--
MoC	1.2	1
W_2C	2.1	1
W_3C_2	----	--
WC	4.85	1

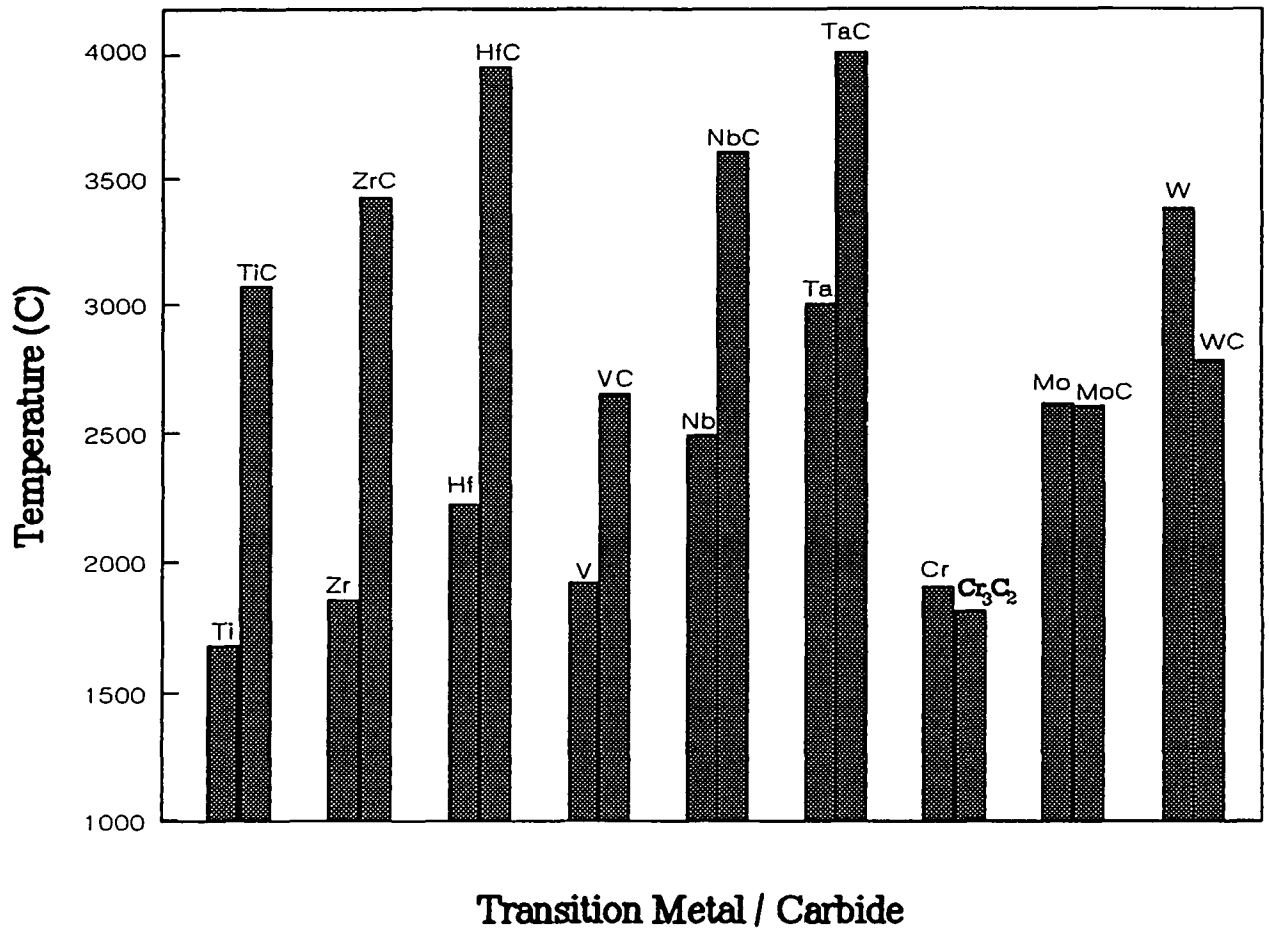

Figure 6 The melting temperatures of the Group IVA, VA, and VIA transition metals and transition metal carbides.[59]

the carbides with the B1 structure is that above 800°C they undergo a brittle to ductile transition.[59] Above the transition temperature, the carbides plastically deform on slip systems analogous to face centered cubic metals. TiC plastically deforms through a (111)*<110> slip system and exhibits 30% ductility at 1500°C.[59]

Carbides of transition metals have metallic character in their electrical, magnetic, and optical properties. Transition metal carbides also exhibit superconductivity at low temperatures. At one time, they had some of the highest known critical superconducting temperatures. They also have high critical field strengths, and were once considered very promising superconductor materials. They have never been used for superconducting applications due to the development of new and better superconducting materials.

There are a number of methods used for synthesizing transition metal carbides. The exact preparation procedure varies with alloy system. In the laboratory, the most common method is direct reaction of the metals or metal hydrides with carbon. Fine spherical powders from the vapor phase are important precursors in ceramic forming. TiC is prepared industrially by the reduction of TiO_2 by carbon. This oxide reduction starts at 935°C and proceeds through four stages between 1000°C and 1500°C; $TiO_2 > Ti_3O_5 > Ti_2O_3 > TiO > TiC$.[60] Transition metal carbides can also be formed through solid state reaction in the form of precipitates in many materials. This precipitation route is widely known in the steel industry. As mentioned earlier, solid state precipitation of transition metal carbides in the NdFeB system will be studied throughout this work.

EXPERIMENTAL PROCEDURE

Data Analysis

The base alloy used in this work is a stoichiometric $Nd_2Fe_{14}B$ alloy. This starting composition is different than in commercial alloys which are generally rare earth and boron rich. Extra rare earth is often added to form eutectic phases which act as a liquid phase sintering aid and as a grain boundary phase to magnetically decouple adjacent grains. Extra boron is added to prevent the formation of free iron and to promote glass forming ability. Stoichiometric compositions were chosen for simplification. Through starting with stoichiometric compositions, the study of the intrinsic and extrinsic metallurgical changes can be simplified. The effects of the additions in commercial alloys can be easily studied once their effects on the stoichiometric compositions are understood.

In order to get clear and unambiguous results, all data concerning transition metal carbide additions are always compared to the base alloy. The goal of this work was to provide fundamental understanding of basic metallurgical properties in the 2-14-1 system. Through basic research leading toward microstructural control, it is hoped to take the *art* out of permanent magnet manufacturing. Often work in the permanent magnetic field is driven by the industry and centers on optimization of the processing and alloying compositions. The data in this work is not optimized but instead focuses on basic research and uses comparable studies with a base alloy in order to give real and significant results.

Alloy Designation

The composition of the alloys studied are of the form $(Nd_{2/17}Fe_{14/17}B_{1/17})_{100-2x} + TM_xC_x$. TM is a representative of the Group IVA, VA, or VIA transition metals. The alloys are designated by the value of X. This designation system is used to avoid

confusion between using atomic%, mole% and weight% additions. As an example, the compositions of TiC added alloys written in terms of different designation systems are shown in Table 2. Using the wt% system is valid, however comparing different transition metal carbide systems is important and vastly different weight percentages are needed in

Table 2 Designation system for TiC additions in $(Nd_{2/17}Fe_{14/17}B_{1/17})_{100-2X} + Ti_XC_X$

Alloy	Wt %			At %		Mol %
X =	% Ti	% C	% TiC	% Ti	% C	% TiC
0.50	0.38	0.09	0.47	0.50	0.50	7.93
0.75	0.57	0.14	0.71	0.75	0.75	11.67
1	0.76	0.19	0.95	1.00	1.00	14.76
2	1.54	0.39	1.93	2.00	2.00	26.19
3	2.33	0.59	2.91	3.00	3.00	35.14
4	3.14	0.79	3.93	4.00	4.00	42.46
5	3.98	1.00	4.98	5.00	5.00	48.60
6	4.82	1.21	6.03	6.00	6.00	53.66
7	5.70	1.43	7.13	7.00	7.00	58.08

order to get the same number of precipitating elements. For instance a 6.0 wt% TiC addition would be equivalent on an atomic scale to a 17.4 wt% WC addition. Atomic percent additions may also be a valid designation system but it causes additional confusion. For instance, an alloy with a 4 at% addition of Ti and a 4 at% addition of C would represent an 8 at% total addition. Mole percent addition is a valid system to represent the additions and comparisons between different transition metal carbide systems can be made.

However, from Table 2, it can be seen that the mole percent additions for some alloys are over 50% which is awkward to work with. Also, depending on the processing conditions, some, all, or none of the TM and C additions may be present as TMC. Mole percent seems to signify that a certain amount of carbide phase is forming. The X designation seems to be the best system. It conveys the composition unambiguously and is useful for comparison of the effects of the transition metal or carbon alone. For instance, a X=4 Ti alloy contains 4 at% Ti and a X=4 TiC alloy contain 4 at% Ti and 4 At% C.

Alloy Purity

All alloy were made from high purity elements. The purity of the starting elements used can be seen in Table 3. The rare earth elements were obtained from Ames

Table 3 Purity of Starting Elements

Element (wt%)	Purity
Nd	99.95
Fe	99.99
Ti	99.97
Zr	99.9
Hf	99.95
V	99.93
Nb	99.9
Ta	99.9
Cr	99.99
W	99.9
B	99.5
C	spectro

Laboratory. All starting alloy compositions were arc-melted from the elements. Transition metal carbides were added to $Nd_2Fe_{14}B$ in the form of transition metals and carbon and if any transition metal carbides subsequently formed it was through liquid or solid state reaction.

Processing Techniques

The processing techniques used in this work are tailored for working with rare earth containing compounds. The light rare earth elements oxidize rapidly and have a significant corrosion rate even at room temperature. Samples were stored in either nitrogen or helium glove boxes to minimize contamination. Melt-spun ribbons due to their extremely fine microstructure were found to be much less susceptible to oxidation at room temperature than arc-melted ingots. Any time the alloys were subject to temperatures above room temperature, they were contained in a protected environment with ultra high purity (UHP) argon. Samples of melt-spun ribbon or ingot were always ground in a nitrogen or helium glovebox. The ground powder was only slightly susceptible to oxidation in a reasonable time period. The grinding process needs to be done in a protected environment because the grinding seems to promote oxidation, probably due to localized heating. Any time corrosion damage was found on ribbons or ingots, at any stage of processing, the samples were discarded and new samples were made.

Arc-Melting

Alloys were prepared from the elements with a lab built arc-melter. Arc-melting is a process where elements are melted on a water cooled copper hearth with electrons. The electrode is maintained at a high potential while the copper hearth is at a low potential. Typical operating values were 125 to 310 amps from a Miller Dialarc Hf power supply.

All arc-melting was done under UHP argon. Ingots of variable sizes could be formed up to 25 g with the typical weight being 10 g. Each ingot was melted, flipped, and remelted a minimum of 4 times to minimize macrosegregation in the as-cast ingot. Samples were weighed before and after arc-melting and only saved if the weight loss was $<= 0.2$ wt%.

Melt-Spinning

Melt-spinning was used as the primary processing tool. Through melt-spinning, an alloy can be rapidly solidified at cooling rates up to 10^6°C/s.[63] By changing the wheel tangential velocity, the cooling rate could be changed. Faster wheel speeds correspond to higher cooling rates. To a first approximation, the mean cooling rate in the vicinity of the solidification point varies linearly with wheel tangential velocity.[64]

The exact cooling rate achieved at a constant wheel speed depends on a number of processing and alloy parameters. The ejection pressure and temperature, chamber gas and pressure, crucible tip diameter and distance above the wheel and superheat temperature all have effects on the cooling rate. In addition, the alloy characteristics such as melting temperature, viscosity, thermal conductivity, and heat capacity influence the amount of and rate of heat transfer during cooling.

The exact numerical value of cooling rate is not required. Reproducible and consistent cooling rates are important. At the level of additions used in this study, the alloy characteristics are going to be affected only insignificantly and are assumed constant. By holding as many of the melt-spinning parameters constant as far as possible, reproducible and consistent cooling rates could be obtained at a particular wheel tangential velocity. Thus, the microstructure and magnetic properties of different alloys cooled at the same wheel speed (cooling rate) could be compared in a direct fashion.

Melt-spinning was done with a custom built melt-spinner. The front and back sides of the melt-spinner can be seen in Figures 7 and 8 respectively. The sample is contained in a quartz crucible with 16mm inside and 18mm outside diameters. The orifice hole diameter is standardized at 0.81 mm +-0.03mm. The flow rates through the orifice of the quartz crucibles were standardized by matching the flow rates for water at two different head pressures. The crucible was placed perpendicular to and 5 mm above the copper melt-spinning wheel.

The melt-spinning parameters are listed in Table 4. Before operation, the melt-spinning chamber was pumped down and backfilled several times with UHP Ar to approximately 10 mT to insure a clean and inert chamber atmosphere. Typically melt-spinning was done at ambient pressure but lower pressure melt-spinning was possible. The crucible pressure was monitored relative to the chamber pressure with a differential pressure gauge. The ejection pressure was set with a Matheson low pressure line regulator and was usually 125 Torr. The sample was heated up through high frequency (450 KHz) Rf induction with a Pillar/Cyle Dyne B-150. A two color Mikron infrared thermometer was used to monitor melt temperature. Heat up times to the standard 1375°C ejection temperature were less than one minute. This fast heat up time minimized contamination from the crucible. The wheel tangential velocity could be varied from 0 to 67 m/s. System vibration limited the upper operating speed to approximately 50 m/s. A DC servo motor gave precise control over the wheel velocity to the limit of the tachometer (+-1 RPM = +-0.01 m/sec). The size of the melt-spun ribbon varied widely at the different wheel speeds. At slow wheel speeds (~10m/s), long ribbons in excess of a meter could be obtained while at the high wheel speeds (~45 m/s) ribbon lengths were typically a couple centimeters.

Figure 7 Front view of the lab built melt-spinner.

Figure 8 Back view of the lab built melt-spinner.

Table 4 Melt-Spinning Parameters

Wheel Speed:	Variable
Ejection Temp:	1375°C
Ejection Pressure:	+125 Torr
Chamber Pressure:	1 Atm
Crucible Tip/Wheel:	5 mm
Chamber Gas:	UHP Ar
Crucible Type:	Quartz
Crucible Tip Diam:	0.81 mm
Wheel:	Copper
Wheel Diameter:	19.1 cm*
	*(1000 rpm = 10m/sec)

In building a melt-spinner, a number of things must be considered and a few special options make the melt-spinner a much more useful and reliable machine. First of all, extra ports and feedthroughs into the main chamber should be added because they will invariably be needed. The melt-spinning wheel size should be chosen carefully depending on the particular application. The wheel size that was used here was 19.1 cm. This was chosen for convenience since 1000 rpm would equal 10 m/s. An operating schematic for the melt-spinner canbe seen in Figure 9. During melt-spinning, a steady melt-stream is necessary. In order to achieve this, a crucible ballast with a large volume is hooked up to the line regulator. In this way, a steady constant ejection pressure can be maintained. In order to stabilize the melt-stream an air break is placed around the wheel (See Figure 8). In order to obtain shiny ribbons and to prevent clogs the chamber atmosphere must be maintained as clean and inert as possible. It was found that under a high vacuum (millitorr range), the electric operated solenoids leaked so they were replaced with high vacuum gas

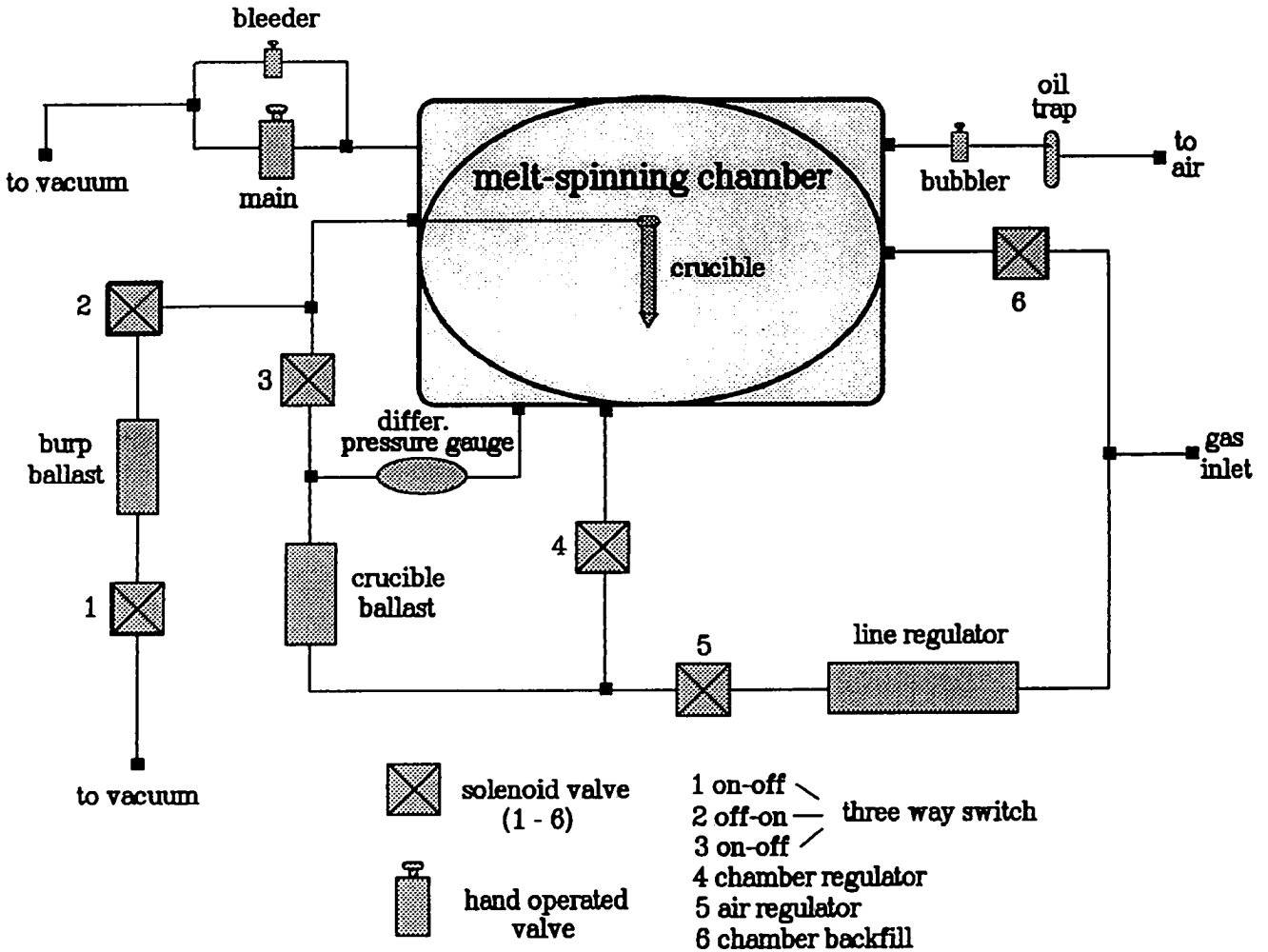

Figure 9 Operation schematic for the lab built melt-spinner.

operated solenoids. The gas operated solenoids were then controlled by the electric solenoids. Aburp ballast has also been added to the melt-spinner. The burp ballast is always maintained in a vacuum. If the molten alloy fails to eject, the burp ballast is turned on which causes the molten liquid to rise up momentarily. This feature often cleared any clogged crucible tips and saved many melt-spinning runs. Through development of a airtight vacuum melt-spinning chamber giving a clean and inert atmosphere and with the above design adaptations, the overall melt-spinning success rate was over 95%.

Heat Treating

Heat Treating was done by first wrapping the ingots or melt-spun ribbons in tantalum foil. The foil packets containing the samples were put in a quartz tube. The tantalum foil protected the sample from the surface of the quartz tube and acted as a getter of any residual oxygen or nitrogen. The quartz tube was pumped down to the millitorr range and back filled a minimum of 3 times to minimize oxygen contamination. Then, the quartz tube was backfilled to one half atmosphere argon and sealed off with a hydrogen torch. For some of the long time anneals of melt-spun ribbons at high temperature, pieces of La metal were sealed in the quartz tube to provide additional gettering.

Heat treating was done in a box or tube furnace. Box furnace anneals were only used for homogenization where precise control over the temperature was not necessary. Heat treating was usually done in a two zone tube furnace calibrated with a NIST traceable standard thermocouple. In all cases, samples were placed into a hot furnace at the appropriate temperature. After the appropriate time, the quartz tube containing the samples was removed from the furnace and allowed to normalize in the air.

Characterization and Sample Preparation

A variety of characterization techniques were used in this work. The sample preparation and operating conditions were standardized as far as possible so that comparisons between alloys could be readily made.

Magnetic

The primary magnetic measuring tool was a DC SQUID magnetometer. A vibrating sample magnetometer was used chiefly for elevated temperature Curie temperature measurements.

SQUID Magnetometer

Superconducting magnetometers utilize superconducting quantum interference devices (SQUID) and are the most sensitive instruments to measure field changes. There are two basic types, DC SQUIDs and RF SQUIDs.[65] DC or direct current SQUIDs contain a superconducting loop with two Josephson junctions while RF or radio frequency SQUIDs contain only one Josephson junction. The Josephson junction is simply a weak link connecting two superconducting wires. This work has utilized the more sensitive DC Squid and the remaining section will focus on DC SQUID operation.

The DC SQUID operates on two basic physical principles. The first is that flux in a closed superconducting loop is quantized. This is a property of superconductors called the Meissner effect which says that once a material goes into the superconducting state the magnetic flux in the material cannot be changed. The second principle is called Josephson Tunnelling. In the Josephson junction, two superconducting wires are separated by a weak link consisting of a very thin insulating layer. Superconducting Cooper pair electrons (or holes) are able to tunnel through the weak link and maintain their phase coherence.[66]

The weak links are important for allowing the quantized flux to change. The presence of the weak links restricts the value of the supercurrent opposing changes in magnetic flux. This weak link allows outside flux to enter the loop. The DC SQUID is biased with a constant current and as the flux increases, the voltage across the SQUID oscillates. Thus, the SQUID produces an output voltage in response to a small input flux. It is essentially a flux to voltage transducer. The DC SQUID magnetometer is an extremely sensitive device providing and output voltage that is periodic to the applied flux within a period of one flux quantum ($2.07 * 10^{-15}$ Wb).[66]

Magnetic measurements were performed using a Quantum Design DC Squid Magnetometer equipped with an extended range capability to measure samples with magnetizations up to 375 emu. It had a normal operating range from 3 K to 400 K with the capability of measuring up to 800K with an optional furnace. The maximum field obtainable was 5.5 Tesla. For magnetic measurements, approximately forty ribbons, with a total mass of approximately 10 to 40 mg, were laid parallel and in two layers on double sided Scotch Tape. The tape was then wrapped onto a quartz rod. The long axis of the ribbons were situated parallel to the applied magnetic field to minimize demagnetizing effects. No demagnetization corrections were used in any of the reported magnetic properties.

Vibrating Sample Magnetometer

The vibrating sample magnetometer (VSM) measures the total magnetic moment of a sample regardless of magnetic origin or physical characteristics of the sample. The sample is hung between the pole pieces of an electromagnet. The sample is vibrated in and out of the field with a sinusoidal vertical vibration. This causes a change in the magnetic induction of the sample which is independent of the applied field and dependant on the

magnetization. Coils mounted in the pole pieces of the electromagnet pick up the signal given off from the sample vibration. The AC signal of the vibration frequency is proportional to the magnitude of the moment induced in the sample. The AC single is also proportional to the vibration amplitude and frequency which are subtracted from the ac signal through the use of a vibrating capacitor.[67]

The VSM used was a model 4500 Princeton Applied Research VSM. It had the capability to measure samples up 10,000 emu (electromagnetic unit) and temperatures up to 1000°C. It was coupled with a Harvey Wells electromagnet with a maximum field of 2.5 Tesla. The VSM furnace temperature was calibrated with a high purity nickel standard. Samples of melt-spun ribbon or ingot were first coarsely ground in a nitrogen glove box with a mortal and pestle. The powder was contained in boron nitride crucibles. The sample chamber was pumped out and backfilled with UHP argon to prevent contamination. The Curie temperatures were determined by the Arrot method.[68]

Microscopy

Microscopy was a very important tool utilized in order to understand the transition metal carbides effects on the microstructure and magnetic properties. The principle microscopy tools were scanning and transmission electron microscopy. Auger microscopy was also done on melt-spun ribbons to observe primary transition metal carbides in as-spun and heat treated ribbons. Optical microscopy was also done on ingots. The problem with optical microscopy was that etching is needed in order to observe the grain and phase boundaries. The acid etch normally used dissolved the transition metal carbides partially or completely which limited the usefulness of the technique.

Scanning Electron Microscopy

The scanning electron microscope (SEM) is an analytical tool which uses a collimated electron beam that is rastered over the specimen surface. When the electron beam strikes the sample it penetrates the crystal lattice and interacts with the lattice and atoms elastically and inelastically. The depth probed depends on the material observed and the accelerating voltage but is typically less than 1 μm. Elastic collisions lead to backscattering and electron diffraction. Inelastic collisions lead to the emission of secondary electrons, Auger electrons, or characteristic X-rays.[69] Secondary electrons are primarily used for imaging and they provide good topological contrast. Backscattered electrons are used for imaging as well but they are more sensitive to atomic number differences and give better phase contrast. Chemical information can be obtained as well from the SEM. Once an inner shell electron is knocked out by an electron from the beam, two general processes occur. A higher shell electron can drop down in energy to fill the vacancy and release characteristic radiation. Elemental identification can be obtained by collecting the characteristic radiation in a SiLi semiconductor.[69] This chemical identification by characteristic radiation is called energy dispersive spectroscopy (EDS). EDS can be used for all elements with atomic number greater than 5, and depending on the element and the alloy has a trace capability of 500 ppm. The second general process that occurs after a inner shell electron is knocked out, is that an outer shell electron can fill the vacancy and another outer shell electron is emitted. The emitted electron or Auger electron has a characteristic kinetic energy and chemical information can be obtained. This phenomenon is used in the Auger electron microscope.

SEM was done with Jeol JSM 6100 or a Cambridge S-200 microscope. The Jeol had a Oxford Link Pentaset EDS system. Semiquantitative analysis was done using a titanium standard with the appropriate ZAF corrections on Microplus Software made by

Dapple. The Cambridge had a Norton EDS system. Semiquantitative analysis was done using MicroQ Software with the appropriate ZAF corrections. Accelerating voltages were typically 15 KV and the working distance was 18 mm. Samples were prepared by the traditional mounting and polishing techniques. Samples were first mounted in dially phylate with a Leco mounting press. The mounted sample was then coarsely ground and polishing was done in steps finishing with a 0.125 μm diamond polish.

Transmission Electron Microscopy

Transmission electron microscopy (TEM) is a microscopy technique where electrons are transmitted through the sample. The transmitted image can be observed directly on a fluorescent screen. Images can be obtained through the brightfield or darkfield modes. A brightfield image is formed from the directly transmitted beam and the scattered and diffracted electrons are not used. A darkfield image is formed in an opposite manner through imaging of the scattered and diffracted electrons. The TEM has a much higher resolution than the SEM and magnifications close to 10^6 power can be achieved. Besides a tool for observing images, the TEM has some additional capability. Generally, TEM have an EDS detector analogous to the SEM. In addition, they have electron energy loss spectrometers (EELS). In EELS, the transmitted electrons are passed through a spectrometer which measures the changes in energy from specimen beam interactions. The losses in energy can be measured and used for elemental identification and also for information about bonding. The technique can be used for elements with atomic number less than 30 and is particularly sensitive to the light elements which complements EDS. Electron diffraction can also be done directly in the TEM to yield structural information. Depending on aperature and detector configurations, microdiffraction, convergent beam electron diffraction, and selected area diffraction can be performed.[69]

TEM was done on a Philips CM-30 microscope. The typical operating voltage was 300 KV after conditioning the filament at 330 Kv. It had a Link Analytical X-Ray EDS detector and a Gatan parallel EELS (PEELS) detector. Samples of melt-spun ribbon were cemented onto copper disks with a 1 mm by 0.5 mm rectangular hole. They were ion milled with argon for approximately 4 hours or until properly thinned in a Ion Tech ion mill. Grain diameters were measured by taking the average value of the chord lengths that connect opposite sides of the grain. One hundred grains were measured for each grain size distribution.

Thermal

Thermal events were measured primarily with a DTA. DTA scans were obtained for each new alloy made and typically were used as an initial source of information. The DSC was used primarily for looking at crystallization enthalpies.

Differential Thermal Analysis

Differential thermal analysis (DTA) is concerned with the rate of change of the temperature of a sample undergoing a constant rate of heat input. Any physical changes in the sample such as melting, crystallization, phase transformations etc. will cause heat to be absorbed or given off which can be measured against an inert reference. For instance, if the sample undergoes an endothermic reaction such as a melting event, it will absorb heat but it's temperature will not increase. When compared to the reference, the sample will be at a lower temperature. An analogous situation occurs for exothermic events. By scanning through a chosen temperature range, any thermal events can be measured.

DTA was performed on a Perkin Elmer DTA 7. Samples were first prepared by grinding melt-spun ribbon or cast ingots in a nitrogen glove box. Samples of

approximately 30 mg were weighed to a precision of 0.001 mg. The DTA furnace was pumped down and backfilled several times and then purged with UHP Ar for a minimum of 15 minutes to prevent oxygen contamination. Heating rates were at 10°C/min with a UHP Ar flow rate of 50 cc/min. Alumina (Al_2O_3) was used as a standard. Typical scans were from room temperature to 1300°C. DTA events were reported as peak onsets due to the heating rate dependance of the peak temperatures.

Differential Scanning Calorimetry

Differential scanning calorimetry (DSC) is a technique which unlike DTA provides quantitative information about thermal events. A thermocouple system is attached to the sample and the standard reference crucibles. When a thermal event occurs in the sample, the sample temperature and the reference temperature become unbalanced. This generates a current in the thermocouple connection. The current produced can be related to the amount of calories released or absorbed.[70]

DSC was performed on a Perkin Elmer DTA 7. Samples were first prepared by grinding melt-spun ribbon or cast ingots in a nitrogen glove box. Samples of powder approximately 30 mg in size were weighed to a precision of 0.001 mg. The samples were placed in a crucible and covered with Al_2O_3 powder to provide thermal insulation. Heating rates were at 10°C/min with an UHP Ar flowrate of 20 cc/min. Alumina (Al_2O_3) was used as a standard. To minimize sampling errors, for each DSC sample, the data is reported as an average of two independent measurements. At the highest wheel speed measured (45 m/s), some melt instability occurred due to system vibration. The DSC measurements at 45 m/s were reported as the highest measured value.

Structural

Structural information was achieved primarily through X-ray diffraction (XRD). The interpretation of XRD scans of 2-14-1 type material was extremely difficult due to the complexity and the number of peaks from the $Nd_2Fe_{14}B$ phase. Phases expected but not found in the XRD scans were often found through electron microscopy. Thus, the identification of second phases through XRD was very difficult and only possible if the second phases existed in significant amounts. As a standard procedure, XRD scans were obtained from each sample of as-spun and heat treated ribbons. Homogenized ingots and each new composition of as-casted ingot were generally X-rayed.

X-Ray Diffraction

X-ray diffraction is a very powerful structure determining tool. The first step is the production of a monochromatic X-ray beam. The beam is made by accelerating electrons from a heated tungsten filament with a high potential towards a metal target (generally copper). The accelerated electrons knock out inner shell electrons, which after outer shell electrons fall in energy, characteristic radiation is released. The characteristic radiation is then filtered to produce a monochromatic beam.[71]

X-ray diffraction is based on Bragg's Law; $n\tau = 2d\sin\Theta$ where n is the order of diffraction, τ is the wavelength of the X-ray beam, d is the distance between crystal planes, and Θ is the diffraction angle. A diffraction scan is first performed over a range of angles. The intensity of the radiation given off is measured at each angular increment. Diffraction only occurs when Bragg's Law is satisfied. Since τ is known and the diffracting Θ values are measured, the d spacings of the crystal planes undergoing diffraction can be calculated. In the JCPDS reference library, standard diffraction patterns are stored which can be compared to the samples pattern which allows the identification of phases.

X-ray diffraction was done on a Phillips diffractometer equipped with a vertical $\Theta/2\Theta$ goniometer. Copper Kα characteristic radiation was filtered with a graphite monochromator and used for diffraction. Typical operating values were 40 KV and 20 mA. Melt-spun ribbons or ingots were first finely ground into powder with a mortal and pestle. The powder was then spread flat on a glass slide which contained a sand blasted square depression. The top of the powder was leveled off to the top of the slide. Typical two theta runs were from 20 to 85°. Typical counting times and step widths were 3.0s and 0.05° respectively.

PART I TRANSITION METAL CARBIDE FORMATION IN THE $Nd_2Fe_{14}B$ SYSTEM AND POTENTIAL AS ALLOYING ADDITIONS

INTRODUCTION

Transition metal carbide formation in the $Nd_2Fe_{14}B$ system (2-14-1) is being studied. Compound additions of the group IVA, VA, and VIA transition metals (TM) along with carbon are being studied due to their formation of very high stability carbides with melting points in some systems approaching 4000°C.[59] The $Nd_2Fe_{14}B$ phase consists of approximately 72 wt% Fe which is a higher percentage of iron than in many common alloy and stainless steels. Since the 2-14-1 system is an iron based system the formation of carbides analogous to conventional steels might be possible as well. Grain growth of rapidly solidified samples during thermomechanical processing is an important problem in the permanent magnet industry.[63,72] If an effective dispersion of precipitates are formed, the grain growth could be inhibited or prevented allowing compaction of melt-spun ribbon or gas atomized powder to full density without the diminution of magnetic properties.

The transition metal carbides are interesting for their potential grain refining ability. The precipitate pinning force resisting grain growth increases as the size of the precipitates decreases and as the volume fraction increases. Grain growth is driven by the reduction in surface energy from the reduction in total grain boundary area per unit volume. It can occur in a normal fashion with a steady increase in the mean grain size while maintaining the grain size distribution.[73] In addition, grain growth can occur in an abnormal fashion, where a small number of grains, due to incomplete pinning or favorable orientation relationships, grow at a much faster rate than the average sized grains.[74] Once the abnormal grains become large, their growth rate is slowed and eventually, the average grain size will catch up.[74] The prevention of grain growth through carbide or nitride

precipitation has been widely studied in the steel industry.[75-78] In steels, the prevention of grain growth is important in order to increase the toughness and the yield strength. In the Hall-Petch[79,80] relationship, the yield strength is found to be inversely proportional to the mean grain diameter to the one half power. In magnetic alloys, grain size is important for the extrinsic magnetic properties. In rapidly solidified Nd-Fe-B type magnets, the optimum grain size is found to be between 20 to 100 nm.[81] This optimum grain size is below the single domain particle radius of 200 nm.[82] In the absence of an applied magnetic field, the grains are single domain particles and the grain boundaries act as pinning sites for the domain wall boundaries. The nucleation controlled demagnetization process occurs by flipping one grain or a small group of grains at a time.[83]

Table 1, shows that the group IVA elements only form one type of binary carbide with a stoichiometry of TMC. The group VA transition metals form carbides with either a TMC or TM_2C stoichiometry. In the group VIA, each transition metal forms three types of carbides with differing stoichiometries. The stoichiometry of the precipitates formed in the 2-14-1 system should depend on the specific transition metal carbide system. In steel processing during tempering, after austenitization, a wide variety of carbide stoichiometries are observed. The stoichiometry of the carbides are found to depend on the TM/C ratio and the rate of formation is dependant on the activation energy of diffusion of the TM through the ferritic or austenitic matrix. For instance, in many stainless steel alloys the carbide formation sequence is as follows; $(FeCr)_3C > (Cr,Fe)_7C_3 > (CrFe)_{23}C_6$.[84] Due to the similarities of the properties and transition metal carbide chemistry within a group, the analysis in this paper will be simplified by using group headings wherever possible.

It is known that when Ti, Hf, or Zr are added to the 2-14-1 system TMB_2 precipitates form due to the extremely high free energies of formation of the borides.[84-86]

The standard enthalpies of formation for the most stable boride and carbide phases of the Group IVA transition metals are in Table 5. It can be seen that the binary transition metal borides are more stable than the binary transition metal carbides. However, if Ti and C are present in solution in the Nd-Fe-B-Ti-C system TiC will form (see PART II). This is because in a multicomponent system phase formation is achieved through a balance of free energies. The formation of the TiC phase can be attributed to the alloy's phase equilibrium and also to the low stability of the $Nd_2Fe_{14}C$ phase.

Table 5 Group IVA Carbide and Boride Standard Enthalpy of Formation[61]

Carbide/ Boride	$-\triangle H_f^\circ$ (kcal/mol)
TiC	22.0
TiB_2	25.8
ZrC	24.2
ZrB_2	26.0
HfC	30.0
HfB_2	26.8

If the transition metal carbides are going to be useful as alloying additions in the 2-14-1 system, they must satisfy certain criteria besides carbide formation. The following criteria will be used throughout this paper to grade the TMC alloys as potential alloying additions. Criterion 1: The phase stability of the precipitates in the specific multicomponent system must be higher than the phase stability of all other phases involving the additive elements and the constituent elements. This also includes not forming any soft magnetic phases or reducing the total amount of hard magnetic phase. Criterion 2: The elemental additions should have significant solubility in the liquid melt at high temperature.

If the additions form immiscible liquids or if they precipitate out entirely as primary precipitates then they have very little ability to affect the microstructure. Criterion 3: The elemental additions should have significant and only nonequilibrium solubility in the 2-14-1 phase. Only by precipitating from supersaturated solid solution can an effective dispersion of precipitates be formed able to prevent grain growth. Also, only nonequilibrium solubility is desired so after an appropriate heat treatment the additions can be precipitated out of supersaturated solid solution leaving the excellent intrinsic magnetic properties of the 2-14-1 phase unaltered. Criterion 4: The transition metal carbide precipitates once formed must be stable to high temperatures and should resist coarsening and dissolution. This is so the ability to prevent grain growth can be maintained at high temperatures.

EXPERIMENTAL APPROACH

The composition of the alloys studied in this section was: $(Nd_{2/17}Fe_{14/17}B_{1/17})_{100-2X} + TM_XC_X$ with X=6. TM is representative of the group IVA, VA, or VIA transition metals. The base alloy was a stoichiometric $Nd_2Fe_{14}B$ alloy and was used for comparison. The transition metal carbides were added on an atomic percent basis for direct comparison of their alloying ability, however, the weight percentages of additions varied widely (Table 6). The high levels of additions were chosen so that changes in the alloying behavior could be easily measured. The level of additions are much greater than

Table 6 Wt% TMC Addition

Alloy	Wt% TMC
X=6 TiC	6.0
X=6 ZrC	10.0
X=6 HfC	17.0
X=6 VC	6.3
X=6 NbC	10.1
X=6 TaC	17.1
X=6 CrC	6.4
X=6 MoC	10.4
X=6 WC	17.4

would be practically used in alloying, so the changes in the measured magnetic properties must be considered carefully since they are not optimized. The alloying ability of the transition metal carbides will be analyzed subject to the previously stated criteria. If the criteria are satisfied then the development of a composite 2-14-1 phase + TMC microstructure will be possible. This will allow the extrinsic properties relating to the

microstructure to be enhanced while maintaining the excellent intrinsic magnetic properties of the 2-14-1 phase. First the transition metal precipitate phases will be identified. In addition, DTA scans will be used to look at changes in alloy behavior and phase formation which can be related to Criterion 1. Through using XRD, energy dispersive means, and visual examination of melt-spun ribbons and arc-melted ingots through Auger and SEM respectively, Criterion 2 can be studied. The equilibrium solubility of the transition metals in the 2-14-1 phase will be measured by studying homogenized cast ingots which will be used for Criterion 3. Through using the data obtained in Criteria 1-3, the as-crystallized magnetic properties will be analyzed. A measure of grain growth will be done by measuring the decrease in magnetic properties after a high temperature long time isothermal anneal which will be used for Criterion 4. After an analysis of the alloying ability, the best TMC system will be chosen for further study and compared to the base alloy in the transmission electron microscopy (TEM).

RESULTS AND DISCUSSION

Alloy Chemistry

Differential Thermal Analysis

If the transition metal carbide system behaves ideally and satisfies Criterion 1, the equilibrium microstructure should be a composite consisting of 2-14-1 phase and transition metal carbide. If no additional phases are formed between the constituent elements and the additive elements, the DTA scans of the TMC alloys should be similar to the base alloy. The DTA peak onsets for each alloy are shown in Table 7. The DTA scans for the base alloy, group IVA alloys, group VA alloys, and group VIA alloys can be seen in Figures 10-13

Table 7 DTA Peak Onsets

Alloy	Peak Onsets									
	Exothermic				Endothermic					
2-14-1	559				1099	1175				
X=6 TiC	632				1161					
X=6 ZrC	612				1090	1163				
X=6 HfC	593				1167					
X=6 VC	597	717			1018	1056	1188			
X=6 NbC	639				1065	1079	1088	1146		
X=6 TaC	616				1099	1146				
X=6 CrC	607	713			1089					
X=6 MoC	613	649	709	743	1058	1072	1086	1107	1175	
X=6 WC	643				1040	1061	1082	1107	1233	

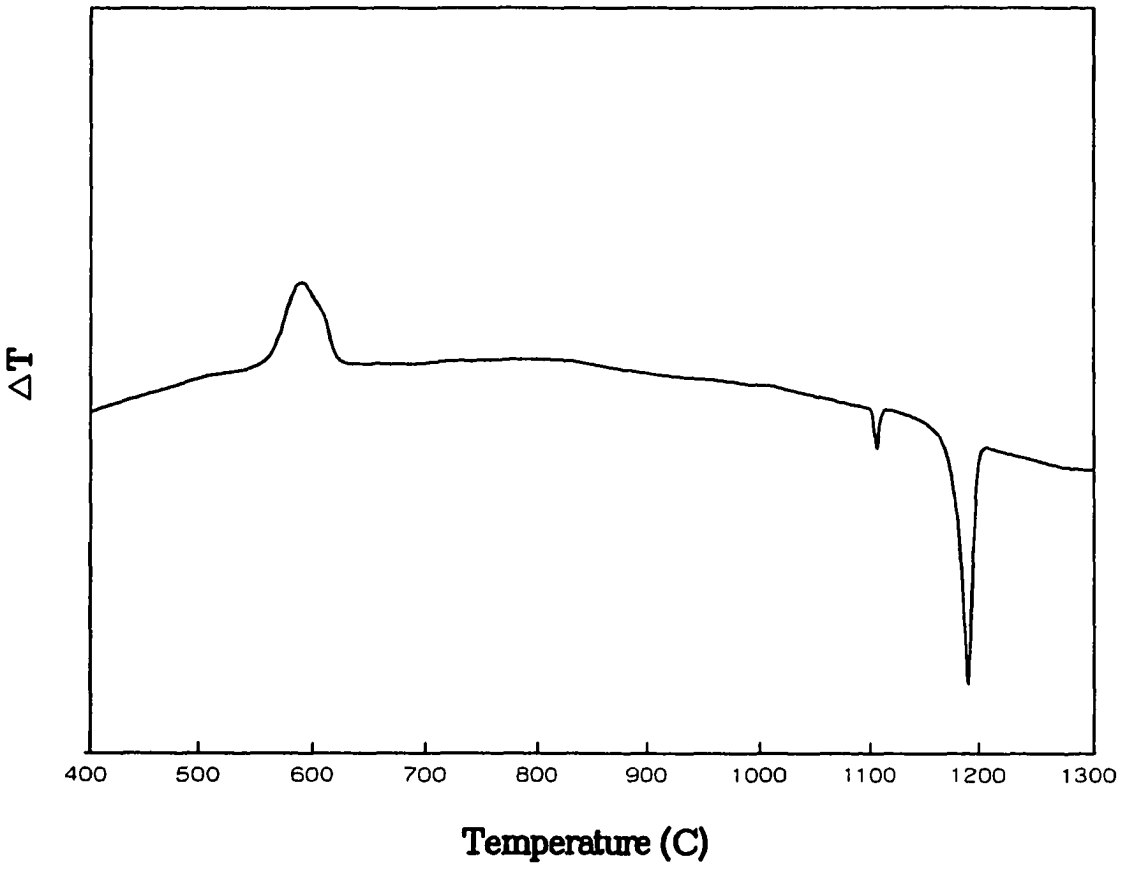

Figure 10 DTA scan of the base alloy which has been melt-spun at 45 m/s.

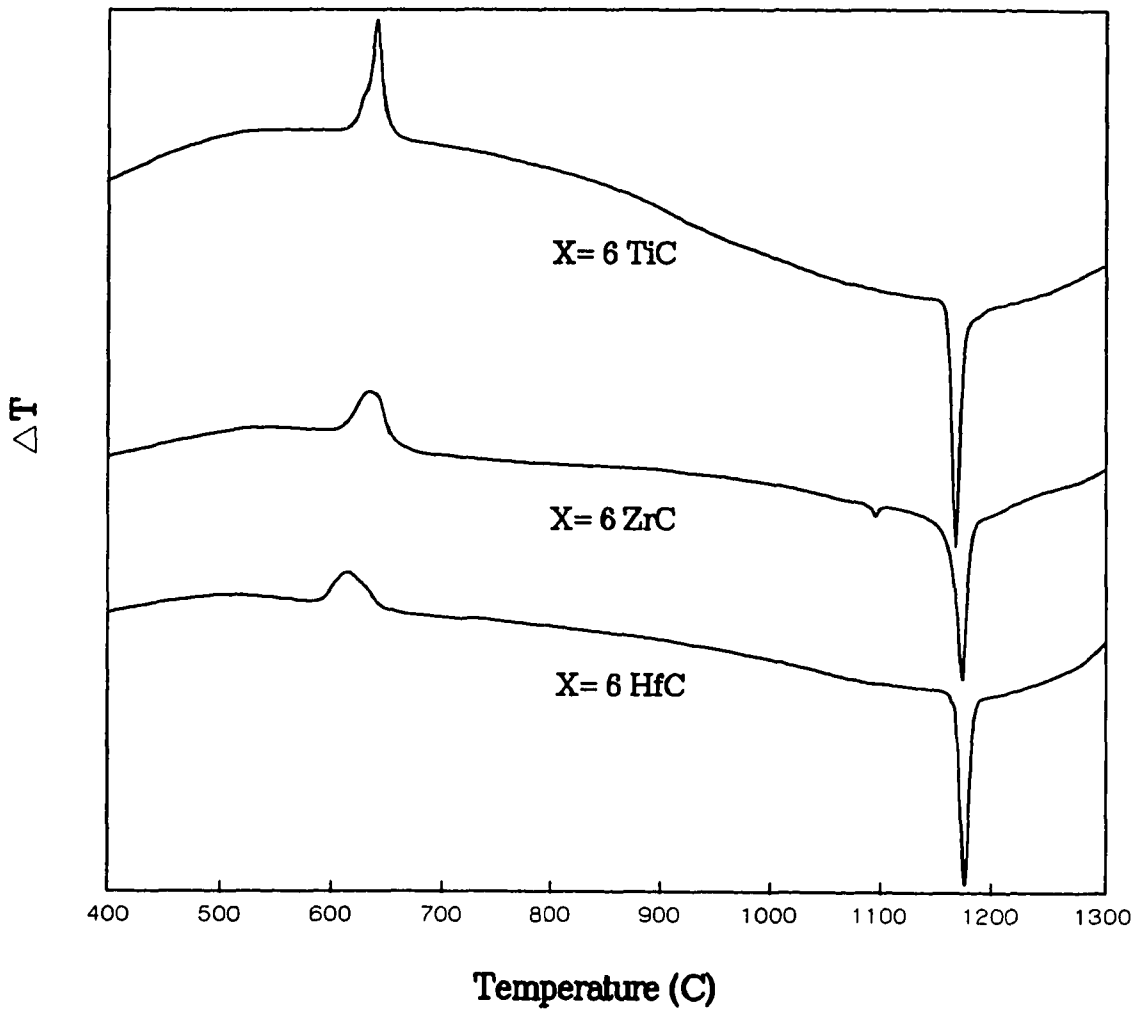

Figure 11 DTA scans for the Group IVA alloys which have been melt-spun at 45 m/s.

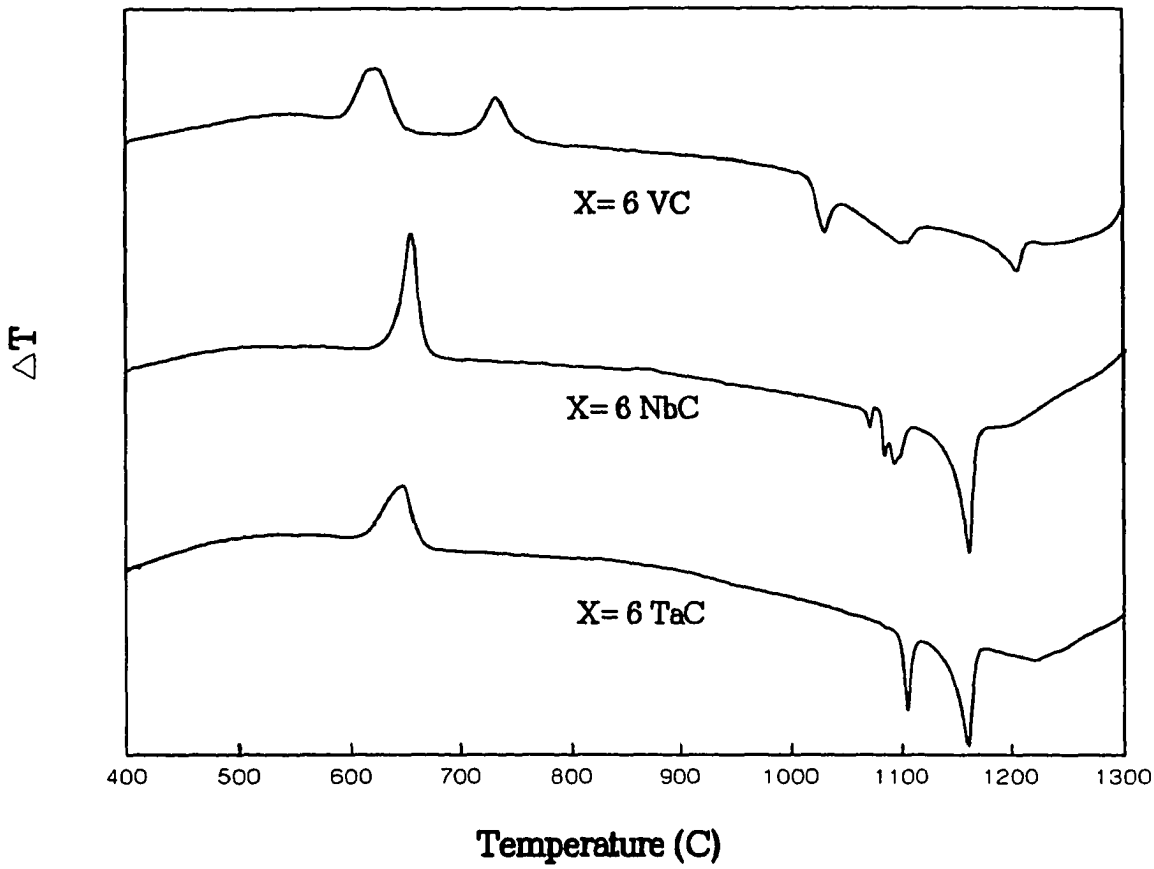

Figure 12 DTA scans for the Group VA alloys which have been melt-spun at 45 m/s.

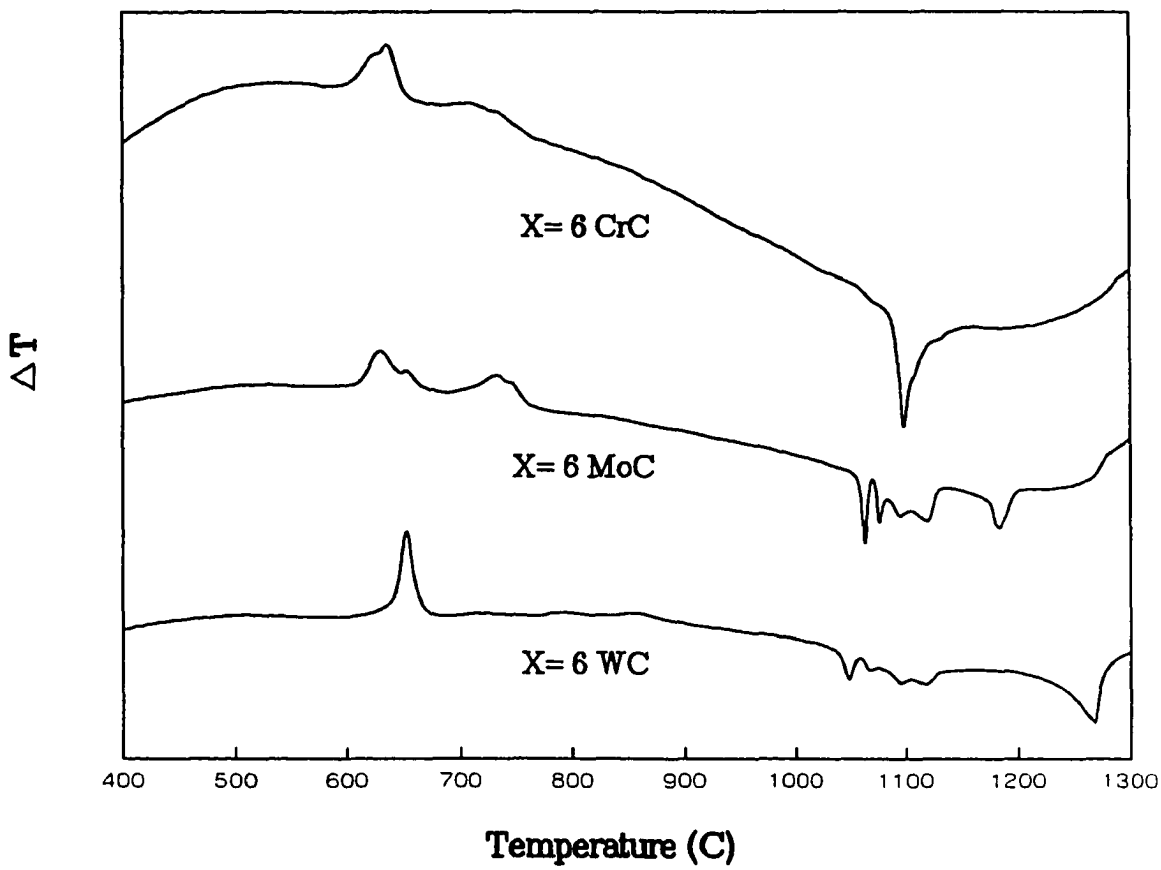

Figure 13 DTA scans for the Group VIA alloys which have been melt-spun at 45 m/s.

respectively. The Group IVA transition metals exhibit very similar behavior when compared to the base alloy. They exhibit only one crystallization event and one major melting event. Also note that the crystallization temperature of the 2-14-1 phase is raised by these additions. In the group VA alloys, the crystallization behavior is similar to the base alloy except for the VC alloy which exhibits two crystallization events. However, the melting peaks indicate that additional phases are being formed. Finally the group VIA alloys seem to exhibit much different crystallization and melting behavior indicating that the Criterion 1 for phase stability has not been met.

Phase Stability

Due to the variety and complexity of the different DTA scans an analysis of the complete phase stability has not been done. The focus in this PART is on the criteria for alloying ability and will concentrate on transition metal precipitate formation. The phases identified in the XRD scans of the as-spun and heat treated ribbons (750°C for 1 hour) can be seen in Table 8. It can be seen that carbide formation occurs in the Group IVA and VA alloys but not in the Group VIA alloys. This is consistent with the enthalpies of formation found in Table 1 and the general trend in chemistry that the strength of carbide formation decreases in going across a series from left to right. It also is important to note no transition metal boride phases were found and that the $Nd_2Fe_{14}B$ phase formed in every alloy. Also, it can be seen that α-Fe coprecipitation with the 2-14-1 phase is commonly observed. This is because small compositional changes or transition metal solubility will cause iron formation since the starting composition is at the stoichiometric composition.

Since melt spinning was done at very high cooling rates($>10^6$°C/s), there should not be enough time for carbide formation during solidification. The carbides present in the as-spun alloys formed in the liquid because the liquid solubility had been exceeded. The

presence of primary TiC, ZrC, HfC, NbC, and TaC precipitates were verified optically and by energy dispersive means in the melt-spun ribbons and homogenized ingots by Auger and SEM respectively. No primary precipitates were found in the cast or melt-spun VC alloys indicating that the liquid solubility had not been exceeded. The primary precipitates were found to be cubic or partially cubic shaped and were found to be between 15 to 25 μm long and 0.5 to 5 μm long in the ingots and melt-spun ribbons respectively. The primary carbides are found to be finer in the melt-spun ribbons and this is attributed to better mixing in the Rf field of the melt-spinner and less time for ripening during cooling after solidification. Due to the large size of the primary precipitates and the small nanograin size of the polycrystalline 2-14-1 phase, the grain refining ability of the primary TMC will be negligent for rapidly solidified material.

Table 8 Phases Identified in Melt-Spun Ribbon

Alloy	Phases	
	As-spun	750°C for 1 Hr
base	none	α-Fe + 2-14-1
X=6 TiC	TiC	α-Fe + 2-14-1 + TiC
X=6 ZrC	ZrC	2-14-1 + ZrC
X=6 HfC	HfC	2-14-1 + HfC
X=6 VC	α-Fe	α-Fe + 2-14-1 + VC
X=6 NbC	NbC	α-Fe + 2-14-1 + NbC
X=6 TaC	TaC	α-Fe + 2-14-1 + TaC
X=6 CrC	α-Fe	α-Fe + 2-14-1
X=6 MoC	α-Fe	α-Fe + 2-14-1
X=6 WC	none	α-Fe + 2-14-1

Equilibrium Solubility

The solubility of the transition metals was measured in samples of arc-melted ingots that were heat treated at 1000°C for one week. The heat treatment temperature and time was chosen from previous work that showed that homogenization was complete after 1000°C for one week for the stoichiometric $Nd_2Fe_{14}B$ alloy. (see PART II) Since diffusion at 1000°C should be rapid, the measured solubilities should be near equilibrium. Small acicular shaped carbides on the order of 0.5 to 1 μm were found in all the group IVA, and VA alloys. Due to the sluggish kinetics of precipitation and the high cooling rate on the water cooled copper hearth of the arc-melter, very few of the secondary precipitates are expected to have formed during solidification. The bulk of the secondary precipitation has presumably occurred during the homogenization heat treatment. This indicates that the group IVA and VA transition metals have significant nonequilibrium solubility since the precipitates must have formed from supersaturated solid solution. However, the formation of a composite 2-14-1 phase and carbide microstructure was only realized for the group IVA alloys. In the group VIA and X=6 VC alloys, there remained a large amount of free iron. A significant amount of transition metal remained dissolved in the iron phase. In addition, in the group VA and VIA alloys there was some rare earth eutectic present and small amounts of other unidentified phases. In the MoC and WC alloys there appears to be significant amounts of second phases that are TM and Fe rich. Although not verified by XRD, it is expected that the phases are the Mo_2FeB_2 and the WFeB phases which have been identified elsewhere in the 2-14-1 system.[87,88]

The measured solubilities for transition metals dissolved in the 2-14-1 phase are shown in Table 9. The group IVA alloys are characterized by no or very low solubility. Only Zr has solubility in the 2-14-1 phase which may be due to favorable size or electronic

Table 9 Wt% TM Dissolved

Alloy (TMC)	2-14-1 (Wt% TM)
X=6 TiC	0.00
X=6 ZrC	0.50
X=6 HfC	0.00
X=6 VC	1.97
X=6 NbC	0.71
X=6 TaC	0.00
X=6 CrC	3.87
X=6 MoC	2.55
X=6 WC	0.90

effects. Capehart et al[89], using extended X-ray absorption fine structure found that Zr substituted for Nd in $Nd_2Fe_{14}B$. In the group VA alloys, high solubility in the 2-14-1 phase is found for V which decreases rapidly down the group with no solubility of Ta. In the group VIA alloys, much higher solubility of the TM in the 2-14-1 phase is found.

The solubilities of the transition metal are consistent with the stability of the carbide phase. This indicates that carbon essentially draws out the transition metal from supersaturated solid solution forming a precipitate. The precipitate should form through heterogeneous nucleation at faults in the microstructure to minimize the lattice strain energy. In the heat treated ingots, secondary carbide formation is found on the iron phase boundaries and on the 2-14-1 grain boundaries. In the melt-spun samples, due to the large amount of grain boundary area per unit volume, the grain boundaries should be the primary site for carbide precipitation. The secondary precipitates were not resolvable in the melt-spun ribbon by Auger analysis or SEM.

As-Crystallized Magnetic Properties

The magnetic properties for samples of as-spun ribbon heat treated at 750°C for one hour can be seen in Table 10. Figure 14 shows the as-crystallized energy products versus the alloying additions. For the purposes of comparison, the mass corrected values

Table 10 Magnetic Properties (750°C for 1 Hr)

Alloy (X=6)	Msat (gauss)	Mrem (gauss)	Coerc. (Oe)	BHmax (MGOe)
2-14-1	14,630	8890	6370	13.5
TiC	14,270	8830	9670	14.5
ZrC	13,390	8150	8900	13.1
HfC	11,880	5920	8720	4.0
VC	12,840	7850	6710	10.7
NbC	13,140	8140	11,350	12.6
TaC	12,270	7510	9250	10.8
CrC	12,070	6620	4630	4.8
MoC	13,440	7600	5540	6.2
WC	10,290	6200	10,550	6.1

of energy product (normalized to starting wt% of magnetic phase) are also plotted in Figure 14. In the group IVA alloys, the coercivity is found to be much higher than in the base alloy. This can be attributed to the fact that the crystallization temperature has been raised. Since the nucleation rate has an Arrehnius temperature dependance, a finer as-crystallized grain size should result in increased levels of energy product. In the HfC alloy a low energy product was obtained. Since no iron was found in the XRD scan, the low value of energy product was attributed to an underdeveloped grain microstructure

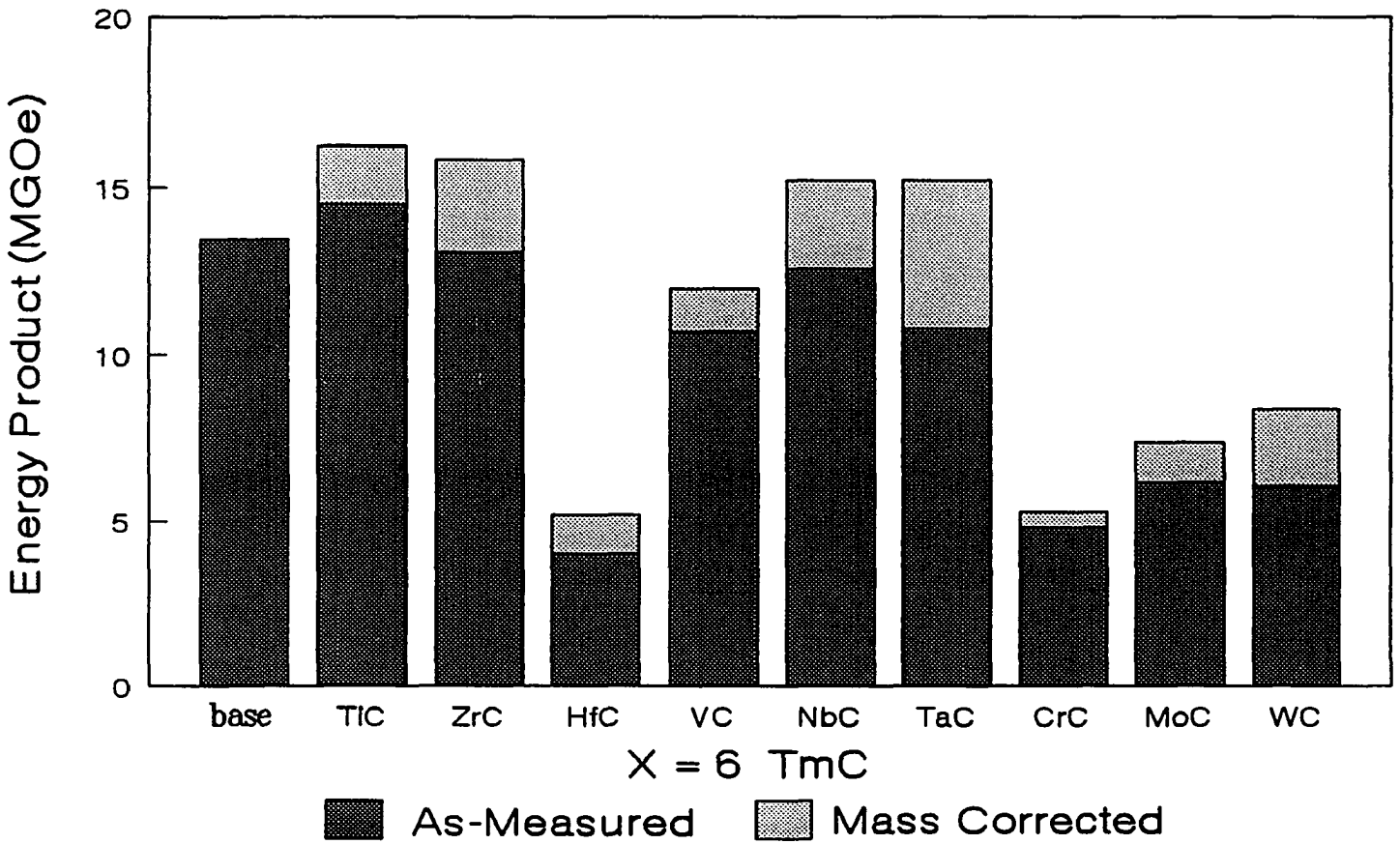

Figure 14 BHmax versus X=6 TMC alloys for melt-spun samples heat treated at 750°C for one hour.

which was verified by subsequent annealing. The group VA alloys, showed energy products comparable to the base alloy. In the group VIA alloys, low as-crystallized energy products were obtained which is consistent with the lack of carbide formation and with the DTA scans which indicated changes in phase formation. From the XRD scans (Table 8), free iron is found to be present in most of the alloys. On the hysteresis demagnetization loops, this magnetically soft iron gives an S-shaped loop which reduced the levels of measured energy product. This degrading effect of free iron formation would probably not occur in commercial alloys that are rare earth rich.

The as-measured and mass corrected saturation magnetization (M_S) values for the 750°C 1 hour heat treatment are shown in Figure 15. Care must be taken in interpreting the Ms data. The values measured are not representative of the true saturation magnetization since the maximum field used was 5.5 Tesla. In addition, many of the samples contain α-Fe which has a high saturation magnetization of 21,580 Gauss.[90] On Figure 15, a straight line is drawn at the base alloy's measured Ms value. It can be seen that the simple mass correction accounts for much of the changes in the M_S values. However, much lower saturation magnetization values are obtained for the VC, CrC and WC alloys. This is consistent with the equilibrium solubility data of Table 9. In the WC cast alloy, the measured equilibrium solubility after the 1000°C heat treatment isn't extraordinarily high at 0.90 wt%. However, it appears that much more W remains dissolved in the 2-14-1 phase of the melt-spun ribbon. Since the heat treatment was only at 750°C, there might not have been enough activation energy to allow diffusion of the large W ion. From the solubility data, it would be expected that the MoC alloy would have a low saturation magnetization as well. However, XRD scans and the measured M_S value indicated that the as-crystallized MoC alloy contains a significant amount of free iron.

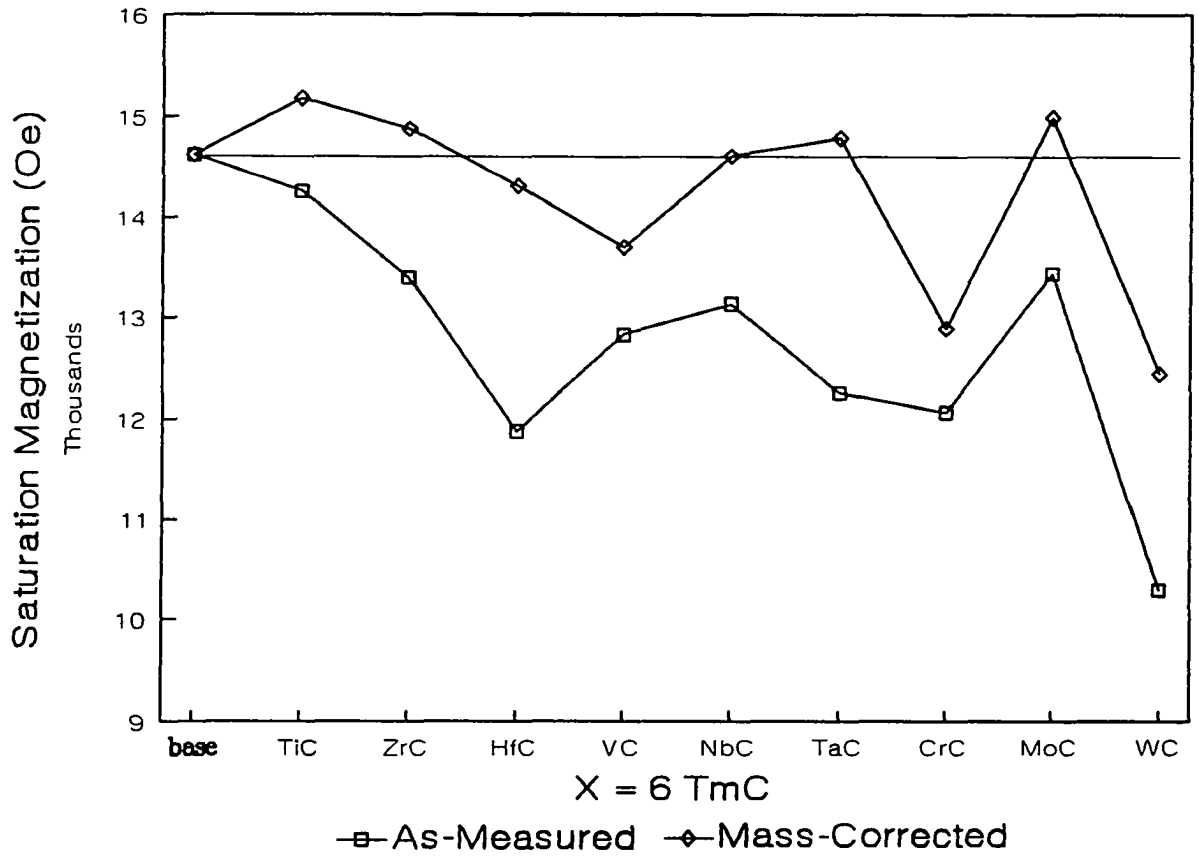

Figure 15 Saturation magnetization versus TMC for melt-spun samples heat treated at 750°C for one hour.

Magnetic Property Diminution

As mentioned earlier to adequately prevent grain growth an effective dispersion of precipitates must be formed. Grain growth can be indirectly measured by observing the diminution of hard magnetic properties during an isothermal anneal. A one day anneal was chosen so the grain growth could occur at a controlled rate and if a pinned configuration occurred, the differences in grain size would show differences in energy product. The energy product of the base alloy versus annealing temperature for a constant one day annealing time can be seen in Figure 16. The measured values of energy product remained constant within experimental error up to 800°C which is presumably the temperature where grain growth begins. The values of energy product drops off rapidly from 800°C to 900°C and then level off at 950°C. This leveling off of energy product was not expected. It is possible that small amounts of second phases have pinned the grains and prevented subsequent grain growth. Since this alloy is at the stoichiometric composition, a more plausible explanation may be that grain growth has continued to occur. Since the optimum grain sizes (20 to 100nm)[81] are found to be significantly below the single domain grain size (200 nm)[82], additional grain growth might be accommodated if defects are concurrently being annealed out. These defects could be chemical such as soft magnetic phases or physical such surface irregularities or oddly shaped grains. Normally larger grains contain more defects and these defects are the sites for the nucleation of reverse domains and the reduction of energy product. In the next section, TEM work gives a mechanism for this leveling off of energy product and the maintaining of coercivity.

It is important to note that the grain growth kinetics for the base alloy is significantly lower than is generally found in commercial magnetic alloys. Mishra et al[72] report significant levels of grain growth in hot pressed or die upset melt-spun

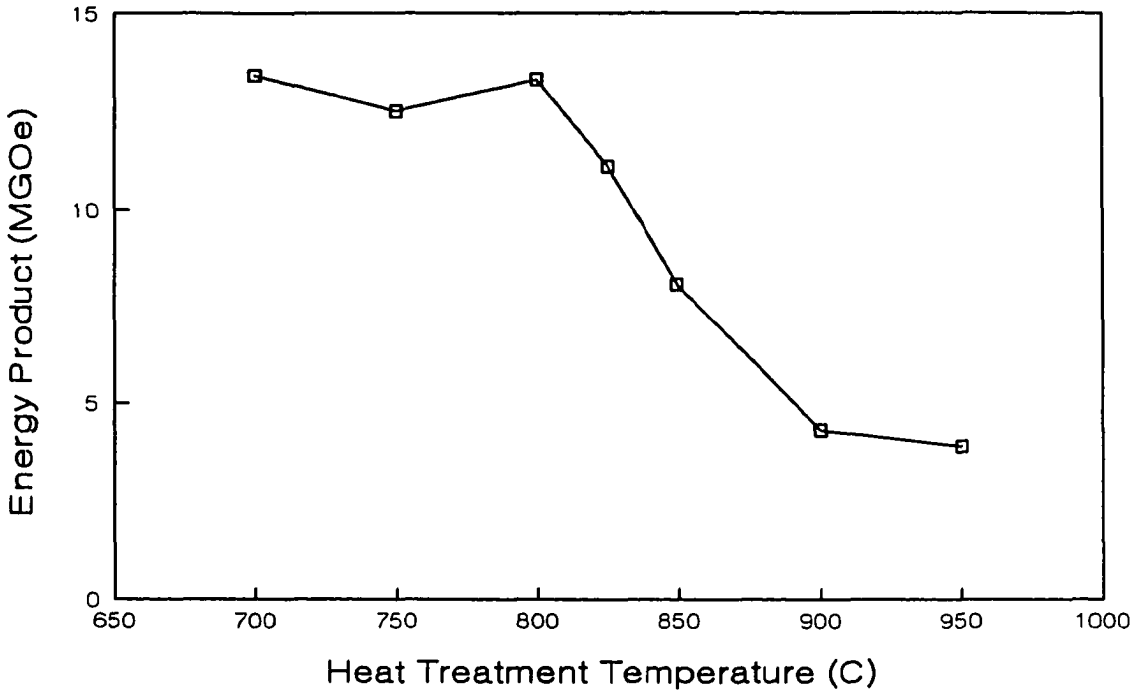

Figure 16 Energy product versus heat treatment temperature at a constant one day annealing time for the base alloy.

ribbon samples at 800°C for times as short as 5 minutes at the composition of $Nd_{0.135}Fe_{0.805}B_{0.06}$. This much higher rate of grain growth is probably due to the fact that Mishra's alloy as well as most commercial alloys are rare earth and boron rich and the eutectic liquid is what causes excessive grain growth. The low grain growth rate and relatively high as-crystallized energy products would seem to indicate that commercial magnets based on stoichiometric compositions might be economically viable. The main problem would be obtaining 100% density without a liquid phase sintering aid but this might be offset by the possibility of higher temperature processing from the carbide stabilized microstructure.

In Figure 17, the energy products for the melt-spun TMC alloys heat treated at 950° for one day are shown. The measured magnetic properties are shown in Table 11. The exact reasons for the diminution of magnetic properties is not entirely clear. Grain growth above the ideal or single domain grain size seems to be only one factor among several possible causes depending on the alloy system. Other possibilities for the reduction in energy product include the formation of soft magnetic phases or the reduction of the total amount of hard magnetic 2-14-1 phase. It should be noted that at the high temperature of 950°C, in some of the TMC systems, the carbides may be coarsening which reduces their grain refining ability. Yet, these same TMC systems may be potent grain refining additions in typical commercial alloys where grain growth occurs at lower temperatures.

The group IVA alloys have measured values of energy product which are as good or better than the base alloy. In the TiC alloy, the energy product is more than double the base alloy. In addition, all the group IVA alloys have significantly higher levels of coercivity. Since the alloys seem to satisfy the alloying criteria, the reason for the enhancement of magnetic properties should be related to the restriction of grain growth.

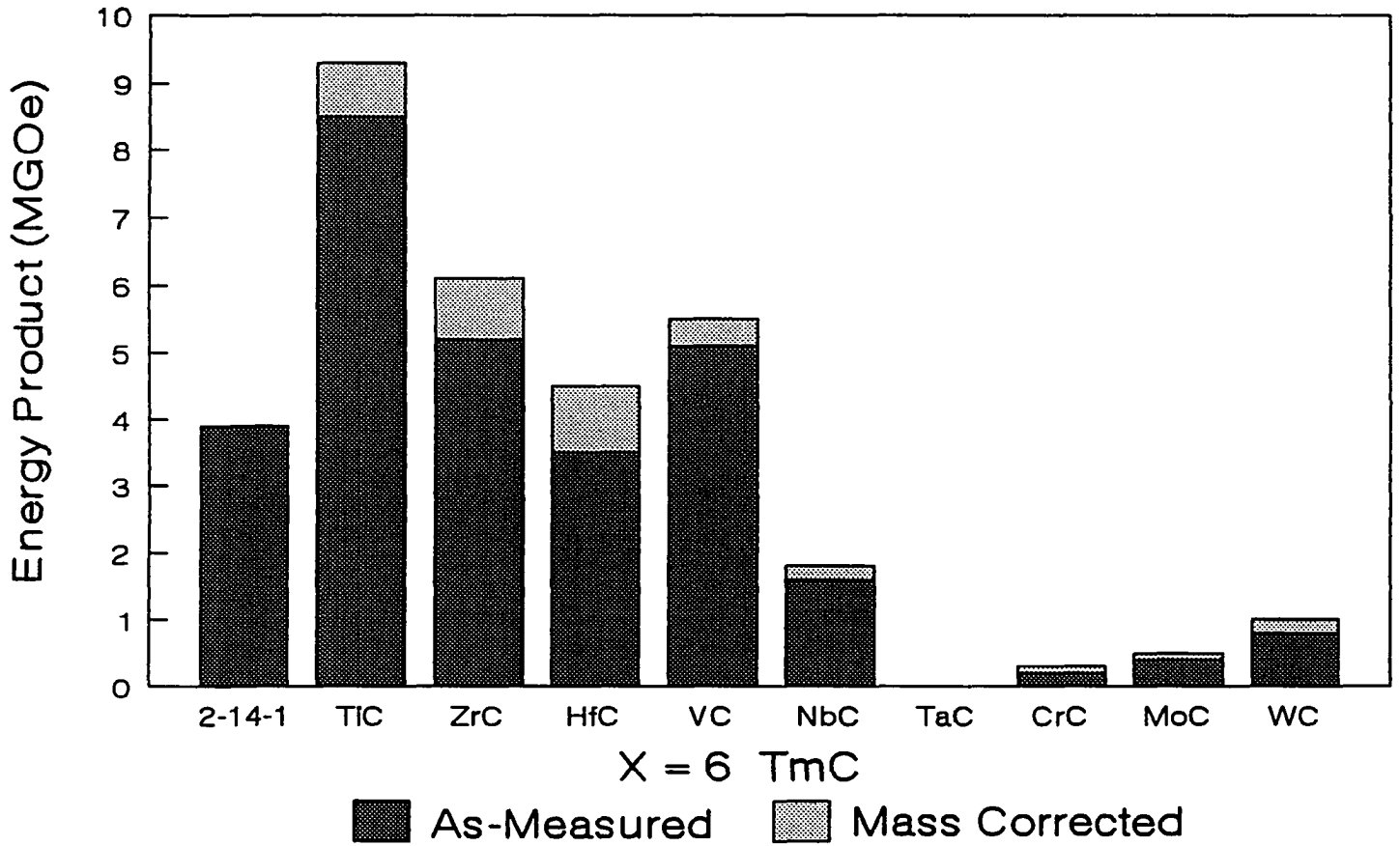

Figure 17 BHmax versus X=6 TMC alloys for melt-spun samples heat treated at 950°C for one day.

Table 11 Magnetic Properties (950°C for 1 Day)

Alloy (X= 6)	Msat (gauss)	Mrem (gauss)	Coerc. (Oe)	BHmax (MGOe)
base	14,670	7300	1210	3.9
TiC	13,740	7830	2450	8.5
ZrC	13,210	6710	4170	5.2
HfC	12,960	6160	3350	3.5
VC	12,440	6860	3470	5.1
NbC	13,640	5060	1590	1.6
TaC	12,710	2950	170	0.0
CrC	12,200	2960	820	0.2
MoC	13,680	4050	790	0.4
WC	11,280	6860	2190	0.8

The group VA alloys only partially satisfy the proposed alloying criteria. Only VC has a higher level of energy product. This may be due to it's high liquid solubility and the formation of many secondary carbide precipitates. In the TaC alloy, very low values of coercivity are obtained leading to an energy product out of the MGOe range. This is surprising considering the alloying behavior and strength of TaC formation. However, from the study of the homogenized ingots, it appears that the liquid solubility of TaC is very low since only a few secondary carbides were found. Since only a few secondary TaC precipitates are formed, grain growth would not be restricted. However, there is no reason to believe that the rate of grain growth of the 2-14-1 phase should be higher in the TaC alloy when compared to the base alloy.

In the group VIA alloys, low levels of energy product are obtained. This is expected from the alloying behavior and the lack of carbide formation. In the WC alloy, significant levels of coercivity are measured. This indicates that other secondary phase besides carbides could also be restricting grain growth.

Transmission Electron Microscopy

TiC fulfills the alloying criteria 1-4 and due to it's low atomic weight is the best choice for an alloying addition. The TiC alloy along with the base alloy was chosen for further study with the TEM. The base alloy heat treated at 750°C for one hour can be seen in Figures 18 and 19. The grain boundaries are found to be exceptionally clean with essentially no second phases. These clean grain boundaries are much different than reported for commercial alloys which always have a rare earth rich crystalline or amorphous grain boundary phase.[91-93] From Table 10, it can be seen that significant levels of coercivity are developed with the stoichiometric compositions. Note the grain boundaries shape and structure which indicates that the grain distribution after the 750°C heat treatment is nonequilibrium.

In Figure 20, the X=6 TiC alloy is shown after the 750°C for one hour heat treatment. A fine distribution of TiC precipitates from 5 to 20 nm in size can be seen at the boundaries and the triple junctions of the 2-14-1 grains. EDS and PEELS identified the precipitates as consisting of only titanium and carbon although some iron intensity was measured, probably from the background. In the middle of the 2-14-1 grains and in areas next to the titanium carbide precipitates, the amount of dissolved titanium was measured. Titanium was not found anywhere in the grains or grain boundaries and was found only in the precipitates. This validates the study of the homogenized ingots and further verifies that titanium has negligible equilibrium solubility in the 2-14-1 phase.

The grain size distribution for the base and the X=6 TiC alloy is found in Figure 21. In addition, the mean grain size, grain size range, and standard deviation are indicated on the figure. TiC is found to have a finer and more uniform grain structure. This is consistent with the higher crystallization temperature for the 2-14-1

Figure 18 TEM micrograph of $Nd_2Fe_{14}B$ melt-spun at 45 m/s and then annealed at 750°C for one hour. Note the nonequilibrium grain structure and the spotty ringed SAD.

Figure 19 TEM micrograph of $Nd_2Fe_{14}B$ melt-spun at 45 m/s and then annealed at 750°C for one hour. Note the nonequilibrium grain structure and the clean grain boundaries.

Figure 20 TEM micrograph of an X=6 TiC alloy melt-spun at 45 m/s and then annealed at 750°C for one hour. Note the distribution of 5-20 nm TiC precipitates (arrows) and the fine spotted SAD.

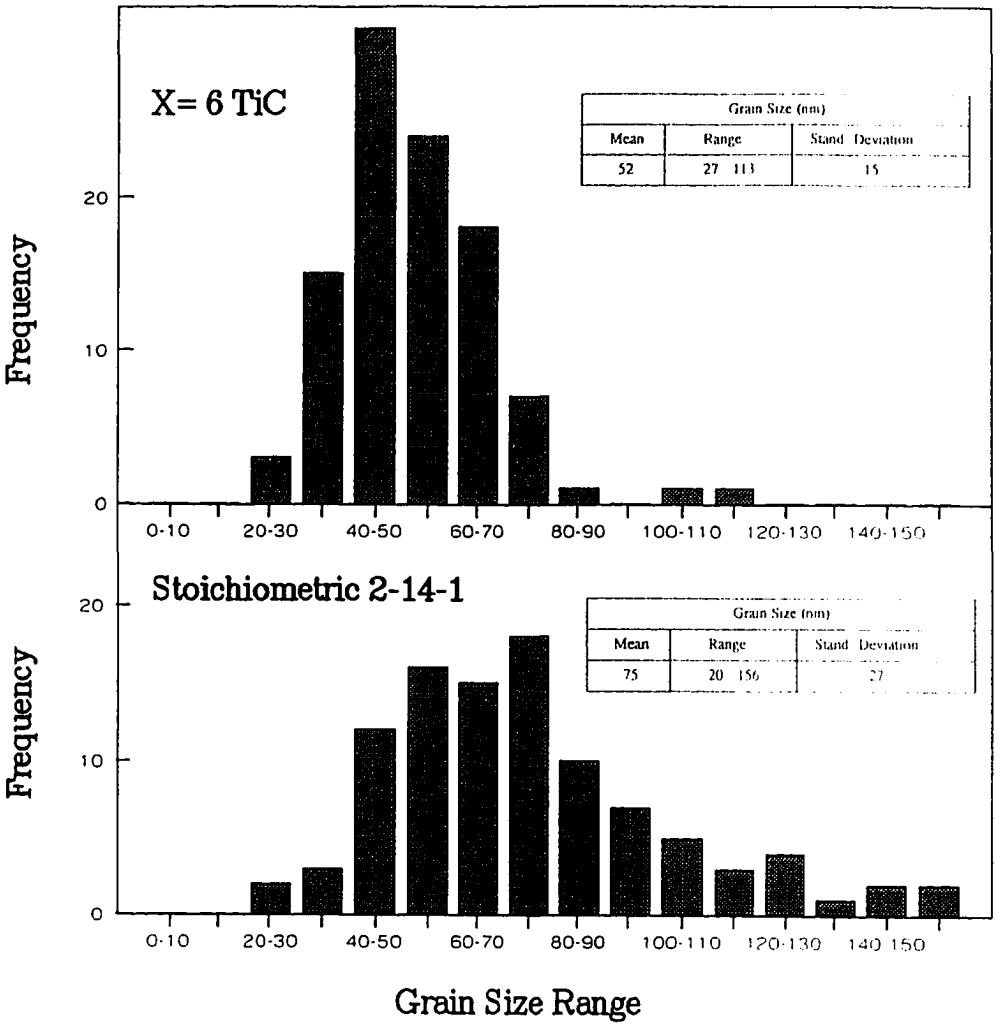

Figure 21 The grain size distribution for the base alloy and the X=6 TiC alloy heat treated at 750°C for one hour.

phase from TiC in solution which gives an enhanced nucleation rate.

TEM was done on the TiC and base alloys after the 950°C for 1 day anneal. In Figure 22 and 23, TEM micrographs are shown for the base alloy after the 950°C for one day heat treatment. Notice, first the much larger grain size (Figure 22). The larger average grain size is formed through normal grain growth. The grains are found to have an equilibrium shape and structure (120° triple boundaries) (see Figure 23).

The microstructure of the X=6 TiC alloy after the 950°C heat treatment is shown in Figure 24. Notice the distribution of the carbides which are 60 to 80 nm in size. The titanium carbides have more than tripled in size during the 950°C heat treatment. The grain distributions and sizes for the X=6 TiC and base alloys are shown in Figure 25 for the 950°C anneal. In the TiC alloy, a much lower rate of grain growth and a much smaller average grain size (117 nm less) is obtained after the 950°C anneal. Since the TiC precipitates coarsened during the heat treatment, their ability to inhibit grain growth was reduced. In commercial compositions, where grain growth occurs at a much lower temperature, an even better restriction of the grain growth should occur.

From the TiC grain size distribution, it is found that a number of grains have grown much larger than the average grain size. This abnormal grain growth is probably occurring when a grain is not properly pinned. Also, in the base alloy, a number of grains have grown very large (> 600nm). These large grains have grown abnormally probably due to a favorable orientation relationship. From these grain distributions, the leveling off of the energy product of the base alloy at 950°C found in Figure 16 can be explained. If only normal grain growth was occurring, the average grain size would progressively increase until all the grains are above the single domain grain size. The coercivity would steadily fall to very low values once the grains became multidomain. Since abnormal grain growth is also occurring, large fast growing grains result in the formation of many small partially

Figure 22 TEM micrograph of $Nd_2Fe_{14}B$ melt-spun at 45 m/s and then annealed at 950°C for 24 hours. Note the grain size distribution and the clean grain boundaries.

Figure 23 TEM micrograph of $Nd_2Fe_{14}B$ melt-spun at 45 m/s and then annealed at 950°C for 24 hours. Note the equilibrium grain structure and the clean grain boundaries.

Figure 24 TEM micrograph of an X=6 TiC alloy melt-spun at 45 m/s and then annealed at 950°C for 24 hours. Note the distribution of 60-80 nm cubic TiC precipitates (arrows) and the spotted SAD.

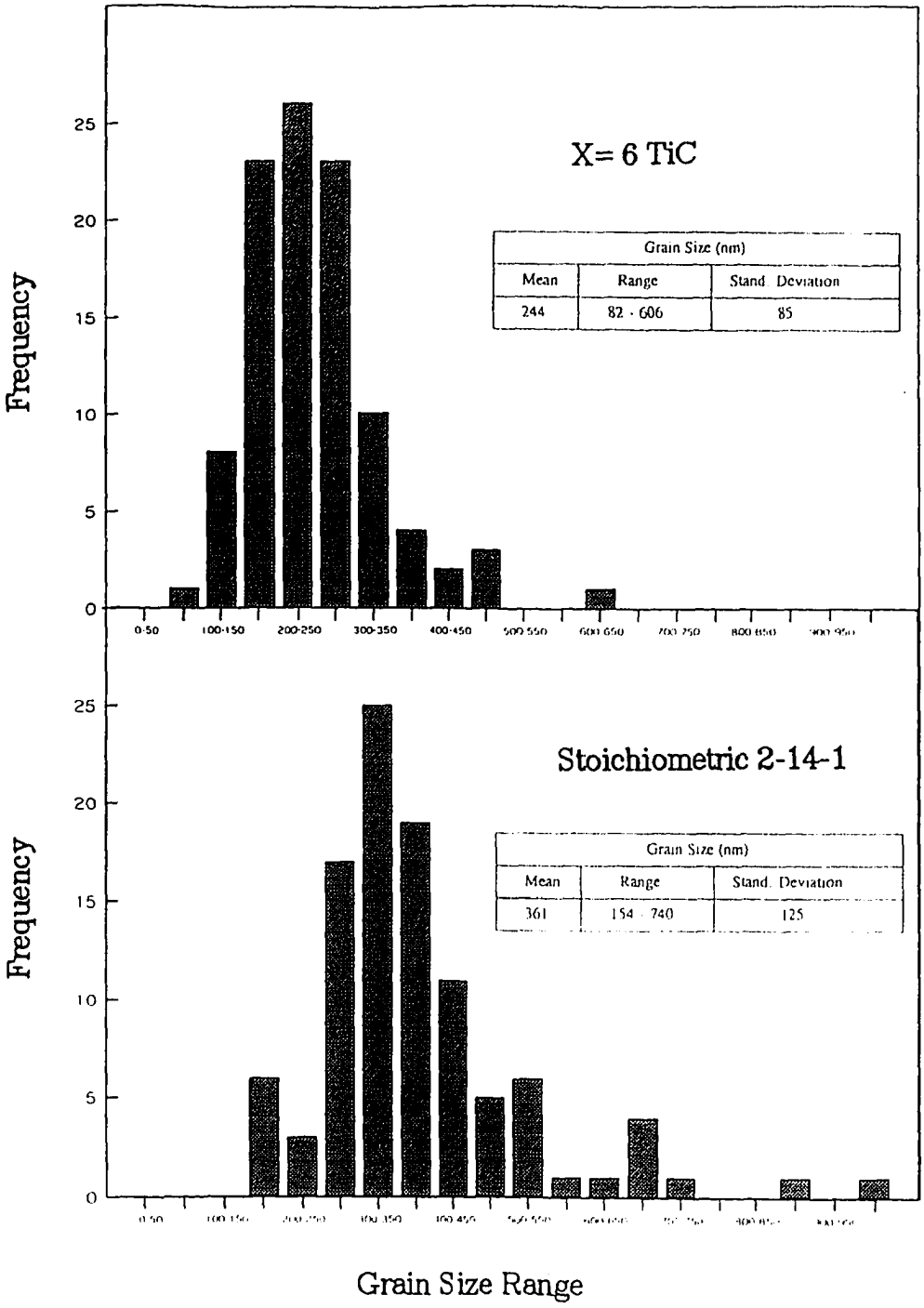

Figure 25 The grain size distribution for the base alloy and the X=6 TiC alloy heat treated at 950°C for 24 hours.

consumed grains. These small grains are slightly below the single domain grain size and therefore have significant coercivity. Since the growth of the abnormal grains is initially fast and then slows, the energy product levels off due to the small partially consumed grains and the effective pinning of the large grain boundaries.

SUMMARY

TMC formation was found for the Group IVA, and VA alloys. No binary transition metal boride phases or $Nd_2Fe_{14}C$ phases were found in any alloy. Criteria were developed to rate the alloying behavior of the transition metal carbide additions. The summary of the fulfillment of the alloying criteria for each alloy is shown in Table 12. The Group IVA alloys satisfy virtually every criteria and are considered excellent alloying additions. TiC seems to be the best choice due to it's low atomic weight and grain refining ability. The Group VA alloys, only partially fulfilled the proposed alloying criteria. VC seems to be the best choice due it's high liquid solubility. These additions have potential as alloying additions but their ability is only moderate. Their use might be limited to optimization of an alloy composition since the additions might involve a tradeoff of properties. The Group VIA alloys do not form carbides and due to their high solubilities in the 2-14-1 phase and the formation of other phases, they have little useful ability as alloying additions. TEM work showed that secondary TiC precipitates formed at the grain boundaries of heat treated melt-spun ribbons. Grain size measurements show that a much lower rate of grain growth is occurring in the TiC stabilized microstructure when compared to the base alloy without carbides. In addition, the TEM work verified many of the alloying criteria of TiC additions besides carbide formation such as criteria on solubility and stability. This validates the analysis in this paper and the proposed alloying criteria for the other transition metal carbide systems, although additional TEM work is warranted.

Table 12 Criteria For Alloying Ability*

Alloy (X=6)	Crit.#1 (Carbide Formation)	Crit.#2 (Liquid Solubility)	Crit.#3 (Solid Solubility)	Crit.#4 (Hi Temp. Stability)
X=6 TiC	Y	Y	Y	Y
X=6 ZrC	Y	Y	P	Y
X=6 HfC	Y	Y	Y	Y
X=6 VC	P	Y	N	Y
X=6 NbC	P	Y	P	P
X=6 TaC	Y	N	Y	N
X=6 CrC	N	Y	N	N
X=6 MoC	N	Y	N	N
X=6 WC	N	Y	N	N

*Criteria Fulfillment: Y = Yes N = No P = Partial

PART II AN SEM STUDY OF PRECIPITATION PHENOMENON IN STOICHIOMETRIC $Nd_2Fe_{14}B$ ALLOYS MODIFIED WITH TITANIUM AND TITANIUM WITH CARBON

INTRODUCTION

In PART I, TMC formation in the $Nd_2Fe_{14}B$ system was studied for the group IVA, VA, and VIA TM and carbon additions. Using alloying criteria, TiC was chosen as the best system for further study. In PART II, the Nd-Fe-B-Ti and Nd-Fe-B-Ti-C systems are studied. The precipitate phases will be shown and identified in order to understand the multicomponent phase equilibrium. Titanium additions are studied in order to compare and contrast its effects with the Ti and C additions.

The study of precipitation in the $Nd_2Fe_{14}B$ system is important for both rapid solidification processing and in the powder route for making permanent magnets. It is found that the coercivity is intimately tied to the grain size of the hard magnetic phase in materials made from both methods of permanent magnet production.[94-96] In order to achieve a uniform fine grain size which is stable during thermal processing, a uniform dispersion of a stable second phase may be used. To be able to form the most effective dispersion of grain refining precipitates, the precipitation process must be understood. This understanding includes more than just the location of precipitation. Precipitates form at surfaces in the microstructure including phase boundaries, grain boundaries, dislocations, etc. because surfaces provide sites for heterogeneous nucleation. In order to form secondary phases, the precipitating elements must come out of liquid or solid solution. Therefore the solubilities of the alloying elements must be known in order for precipitation to be understood. This includes an understanding of the liquid and solid solubility as well as the equilibrium and nonequilibrium solubility. The solubility of an element in a phase will also depend upon the other elements dissolved in the phase which

leads to a specific phase equilibrium. The maximum precipitate pinning force at the grain boundaries increases as the volume fraction of the precipitates increases and as the size decreases.[78] In order for the precipitates to effectively prevent grain growth, they must be stable at high temperatures. Both dissolution and coarsening (Ostwald Ripening) will diminish the effective pinning force.

EXPERIMENTAL APPROACH

The compositions of the alloys studied in this section are found in Table 13. Compositions are given in the form $(Nd_{2/17}Fe_{14/17}B_{1/17})_{100-X}$ + $Addition_X$. The study of as-cast and homogenized ingots in the Nd-Fe-B-Ti and Nd-Fe-B-Ti-C systems will be used to gain an understanding of the solubilities of the additive elements and the stabilities of the precipitating phases. The results from this section will be useful in the powder route to making permanent magnets and can be related to the precipitation processes occurring at a much finer scale in rapidly solidified samples.

Table 13 Composition of Alloys Studied

Alloy	Composition	Ti Add X=	C Add X=
X=2 Ti	$(Nd_{2/17}Fe_{14/17}B_{1/17})_{100-x} + Ti_x$	2	
X=6 Ti	$(Nd_{2/17}Fe_{14/17}B_{1/17})_{100-x} + Ti_x$	6	
X=2 TiC	$(Nd_{2/17}Fe_{14/17}B_{1/17})_{100-2x} + Ti_xC_x$	2	2
X=6 TiC	$(Nd_{2/17}Fe_{14/17}B_{1/17})_{100-2x} + Ti_xC_x$	6	6

RESULTS AND DISCUSSION

Titanium Addition

When titanium is added to the 2-14-1 system it might be expected that it will combine with boron to form titanium borides due to their extremely high free energies of formation. In the X=2 Ti as-solidified alloy, the solidification sequence was found to be unchanged with properitectic iron, 2-14-1, and rare-earth rich eutectic phases formed. In the as-cast microstructure a few titanium rich acicular precipitates (marked with arrows) from 0.5 to 1.0 μm in length were formed at the grain boundaries of the matrix phase in typically a continuous manner (Figure 26). Not many precipitates are formed during cooling after solidification because only a very short time is spent at the peak precipitation temperature. The peak precipitation temperature occurs where the diffusion rate and driving force is maximized. There is simply not enough time during the peak temperature range for the precipitation process to occur to any significant extent due to the fast cooling rate occurring on a water cooled copper hearth. In the as-cast microstructure titanium is found dissolved in the α-Fe and the 2-14-1 phases. In the properitectic iron phase 1.32 wt% Ti was found and in the 2-14-1 phase 1.07 wt% Ti was found. These results show that titanium has significant nonequilibrium solubility in both the iron and 2-14-1 phases.

After the homogenization heat treatment, many additional fine precipitates on the order of 0.5 to 1 μm long were found in the microstructure (Figure 27). These secondary precipitates are very similar in size and appearance to the ones formed initially during cooling after solidification. These precipitates formed along the grain boundaries of the 2-14-1 phase in a bunched up fashion typically as colonies. Three such colonies are marked in Figure 26 with arrows. Due to the precipitates small size, an accurate EDS scan could not be performed for semiquantitative analysis but the precipitates were

Figure 26 SEM micrograph of an as-cast X=2 Ti alloy. Arrows show the location of the TiB_2 precipitates.

Figure 27 SEM micrograph of an X=2 Ti alloy homogenized at 1000°C for one week. The arrows indicate colonies of TiB_2 formation.

titanium rich. No titanium boride phases were found in the X-ray diffraction scan due to the low atomic weight of the borides and the many peaks in the 2-14-1 diffraction pattern. It is expected that the precipitates formed during cooling and after homogenization are TiB_2 as found in the 2-14-1 system elsewhere.[84,85] In the 2-14-1 phase, it was found from semiquantitative EDS analysis that 0.47 wt% Ti remained which is representative of an equilibrium solubility in an alloy containing Nd, Fe, and B.

In the X=6 Ti alloy, the solidification sequence of the as-cast microstructure had been altered (Figure 28). Primary titanium rich rod-shaped precipitates (labeled 1) approximately 3 to 12 μm long and 1 to 3 μm in diameter formed in the liquid phase. In addition, there were a few titanium rich acicular shaped secondary precipitates (labeled 2) ranging in size from 0.5 to 1 μm long that formed after solidification during cooling. From EDS directly on the primary rod-shaped precipitates, it was found that they consist of 56.1 wt% Ti. This is a little lower than the expected value of 68.8 wt% Ti in the TiB_2 phase. Due to the spot size of the electron beam some intensity was measured from the surrounding 2-14-1 phase which may have caused some error in this measurement. From X-ray diffraction scans the titanium rich precipitates in the X=6 Ti alloy were verified to be the TiB_2 phase (Figure 29). Along with the TiB_2 phase, α-iron, Nd_2Fe_{17}, and $Nd_2Fe_{14}B$ phases were found. In this alloy, the weight percent titanium dissolved in the as-cast phases was not determined due to the difficulty in distinguishing between the 2-17 and 2-14-1 phases.

After the homogenization heat treatment, additional titanium rich precipitates on the order of 0.5 to 1 μm long were found in the microstructure. In Figure 30, the primary and secondary titanium borides can be seen in the homogenized microstructure of the X=6 Ti alloy and are labeled 1 and 2 respectively. The X-ray diffraction scan indicates only the presence of TiB_2 and Nd_2Fe_{17} phases. From stoichiometric considerations, there

Figure 28 SEM micrograph of an as-cast X=6 Ti alloy. Primary and secondary TiB_2 precipitates are labeled 1 and 2 respectively.

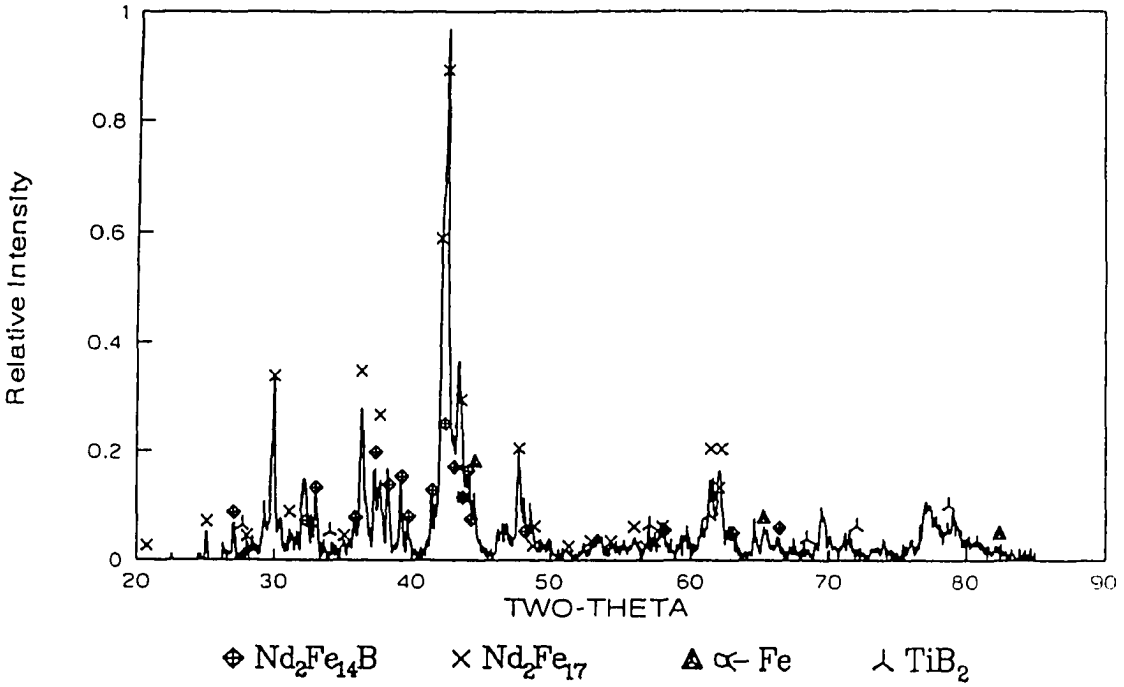

Figure 29 XRD of the as-cast X=6 Ti alloy.

Figure 30 SEM micrograph of an X=6 Ti alloy homogenized at 1000°C for one week. The primary and secondary TiB_2 precipitates are labeled 1 and 2 respectively.

is more than enough titanium present in the alloy to react with all of the boron to form the TiB_2 phase with 2.8 wt% Ti left over. Apparently this reaction occurred to completion which caused the remaining neodymium and iron to form the 2-17 phase. A significant amount of titanium was found to remain soluble in the 2-17 phase. From EDS, 2.2 wt% Ti remained dissolved in the 2-17 phase after homogenization.

Careful study of the primary and secondary titanium borides in the as-cast and homogenized alloys indicated the stability of the precipitates. The size and appearance of the borides present in the as-cast microstructure remained unchanged after homogenization. This shows that the titanium borides will not dissolve at high temperatures and resist coarsening at least to 1000°C. The high temperature stability of the titanium borides gives them the potential of being effective grain pinners. Their effectiveness in practice will depend on forming an appropriate dispersion which may be difficult due to the tendencies of the borides to form in clumped up colonies.

Titanium and Carbon Addition

When titanium and carbon are added to the 2-14-1 system, many precipitating phases are possible. From the JANAF Thermochemical tables[97], the standard free energies of formation for the TiB_2 and the TiC phases are -192.185 kJ/mol and -180.438 kJ/mol respectively. These binary phase free energies indicates that titanium boride would be the most stable second phase. However, the balance of free energies leading to equilibrium in a multicomponent system does not necessarily agree with binary phase equilibrium. In the quintery Fe-Nd-Ti-B-C system, TiC is found to be the most stable secondary phase. Apparently in the boron case, there is a free energy balance between using the boron to form a titanium boride or using the boron to form the 2-14-1 phase.

The low stability of the $Nd_2Fe_{14}C$ phase alters the phase equilibrium and makes it more favorable in energy for the titanium carbide to form.

In the as-cast X=2 TiC alloy, the normal ternary solidification sequence is found to remain unaltered (Figure 31). In the microstructure, there is found to be acicular shaped titanium rich precipitates (marked with arrows) present on the order of a 0.5 to 1.0 μm long. In the matrix 2-14-1 phase, there is found to be 1.30 wt% Ti dissolved and 1.71 wt% Ti dissolved in the properitectic iron phase. Due to the small size of the precipitates, semiquantitative analysis could not be performed on them.

After the homogenization heat treatment, many additional fine titanium rich precipitates were formed (Figure 32). The carbides were distributed in discrete 0.5 to 1 μm long particles along the matrix grain boundaries (marked with arrows) and also along the prior iron boundaries which had since homogenized (labeled 1). The carbides which formed during cooling after solidification and the ones formed during homogenization are both similar in size and appearance. This might be expected since in both cases the precipitates formed from supersaturated solid solution. The X-ray diffraction scan only indicated the presence of the 2-14-1 phase. Due to the low atomic weights and the small volume fraction of precipitates present, the titanium carbides did not show up in the X-ray diffraction scan. After the homogenization heat treatment, only 0.06 wt% titanium remained in the 2-14-1 phase. The equilibrium solubility may be even less than the measurements indicated due to the many fine precipitates found throughout the microstructure and the interaction volume of the beam. Nevertheless, this indicates that the equilibrium solubility of titanium with carbon in the 2-14-1 phase is extremely small.

In the X=6 TiC alloy, the solidification sequence was found to be altered. Primary titanium rich precipitates from 10 to 20 μm long (labeled 1) formed along with the acicular shaped 0.5 to 1.0 μm long (labeled 2) secondary precipitates as shown in Figure 33.

Figure 31 SEM micrograph of an as-cast X=2 TiC alloy. The arrows show the location of TiC secondary precipitates.

Figure 32 SEM micrograph of an X=2 TiC alloy homogenized at 1000°C for one week. The arrows mark the location of the TiC precipitates. TiC precipitates that formed on the dendritic iron boundaries which have since homogenized are labeled 1.

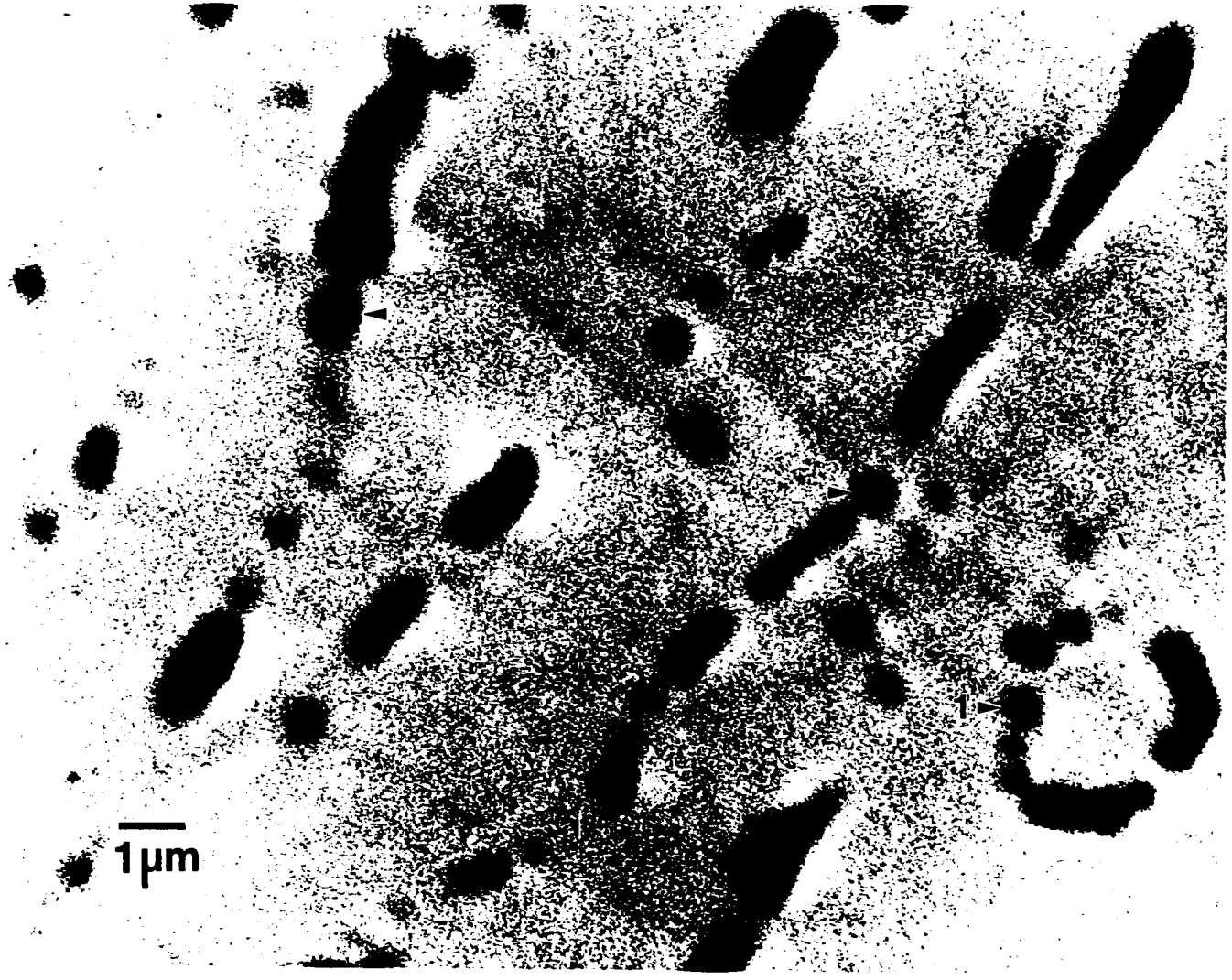
1μm

Figure 33 SEM micrograph of an as-cast X=6 TiC alloy. The primary and secondary TiC precipitates are labeled 1 and 2 respectively.

The primary precipitates appear to have first formed from the liquid in a cubic form and then partially reacted during solidification. Some of the primary carbides remained essentially cubic in form while others experienced a much greater degree of dissolution. The envisioned solidification scenario is as follows; first at high temperature in the liquid primary TiC cubic precipitates formed reaching an equilibrium of titanium and carbon in the liquid phase. Then during solidification, properitectic iron dendrites formed which contained some titanium. To maintain the depleted liquid equilibrium some parts of the primary titanium carbide precipitates redissolved. From EDS, the primary carbides are found to be 80.65 wt% Ti which is very close to the expected value of 79.95 wt% Ti in the TiC phase. X-ray diffraction scans verify the formation of the TiC phase. In the as-cast microstructure, 1.24 wt% Ti was found in the 2-14-1 phase and 1.76 wt % Ti was found in the iron phase. These results agree well with the X=2 TiC alloy and show titanium has at least a 1.3 wt% nonequilibrium solubility in the 2-14-1 phase. It should be noted the value of the solubility observed in a phase upon solidification will depend on the cooling rate where the maximum possible nonequilibrium solubility is equal to the liquid phase solubility.

The homogenized X=6 TiC alloy's microstructure can be seen in Figure 34. In addition to the primary (labeled 1) and solidification precipitated TiC precipitates, many fine precipitates (labeled 2) from 0.5 to 1.5 μm long were formed as discrete noncontinuous particles along the grain boundaries. A titanium carbide precipitate which formed at the triple junction between grains is labeled 3 in Figure 34. The X-ray diffraction scan of the homogenized X=6 TiC alloy indicates the presence of only two phases; 2-14-1 and TiC (Figure 35). After the homogenization heat treatment, only 0.02 weight percent of titanium could be found in the 2-14-1 phase. This result agrees well with the value found in the X=2 TiC alloy and shows the equilibrium

Figure 34 SEM micrograph of an X=6 TiC alloy homogenized at 1000°C for one week. The primary and secondary TiC precipitates are labeled 1 and 2 respectively. A TiC precipitate that formed at the triple junction of the grains is labeled 3.

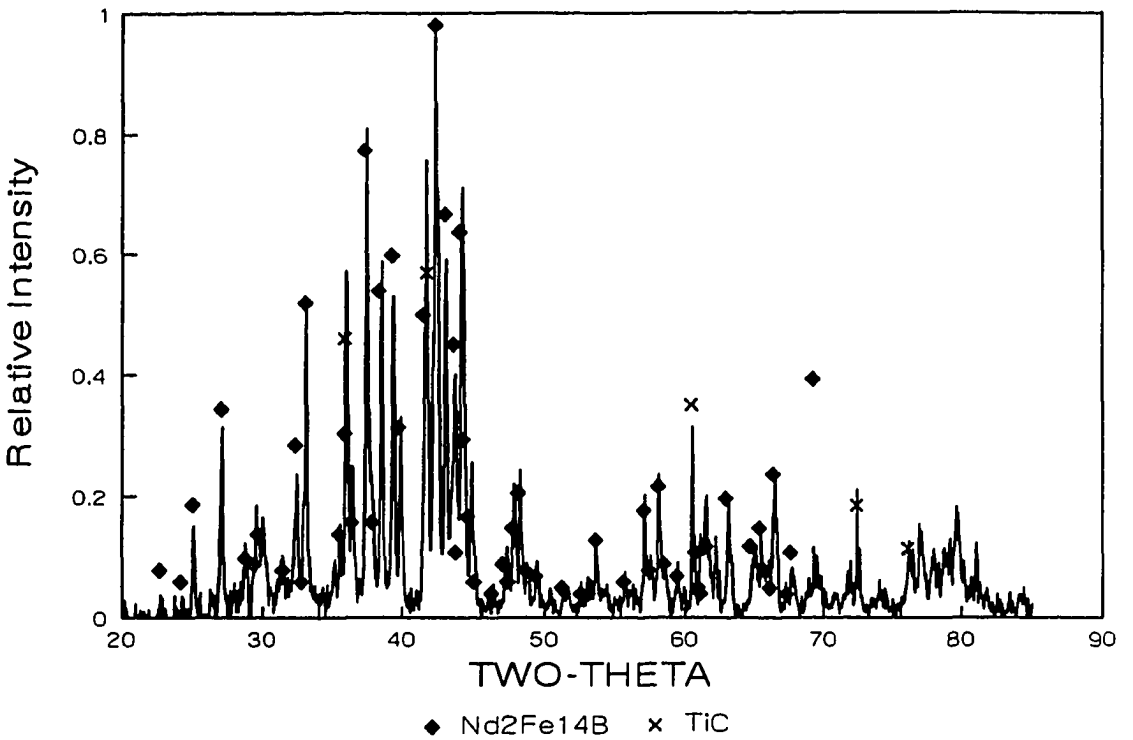

Figure 35 XRD of X=6 TiC alloy which has been homogenized at 1000°C for one week.

solubility of titanium in the 2-14-1 phase with Nd, Fe, B, and C present is extremely small.

By comparing the appearance and size of the titanium carbides in the as-cast and homogenized alloys, no differences could be found. This indicates that the titanium carbide precipitates are stable at high temperatures to at least 1000°C. Once formed they do not dissolve and they resist coarsening to high temperatures. In addition, the titanium carbides tend to form at the grain boundaries as discrete particles. Therefore, the titanium carbide precipitates are excellent candidates for the formation of a effective dispersion leading to the prevention of grain growth.

SUMMARY

The phase stabilities of the precipitating phases in the Nd-Fe-B-Ti and Nd-Fe-B-Ti-C systems was studied. When titanium is added above the solubility limit of the 2-14-1 phase, titanium borides will form. When titanium with carbon are added to the 2-14-1 system, titanium carbides will form. Once the solubility limit of the liquid melt was exceeded, primary titanium boride or primary titanium carbide phases were formed. In the X=6 Ti alloy, primary rod shaped titanium borides were formed approximately 3 to 12 μm in length and 1 to 3 μm in diameter. In the X=6 TiC alloy, the primary precipitates formed with a cubic shape with an edge length between 10 to 20 μm. The liquid solubility limits were not determined but in the X=2 Ti and X=2 TiC alloys the precipitates were entirely soluble. Primary precipitates were found in the X=6 Ti and X=6 TiC alloys which showed that the compositions exceeded the liquid solubility limit.

Besides precipitation from the liquid, carbides and borides were formed during cooling after solidification. This type of precipitation occurred for each alloy although the precipitation reaction was far from complete due to inadequate time at the peak precipitation temperature. A significant amount of Ti remained dissolved in the α-Fe and 2-14-1 phases in the as-cast ingots of every alloy.

After the homogenization heat treatment, additional precipitation was observed in each alloy, signifying that the dissolved precipitating elements existed in supersaturated solid solution. These secondary precipitates were much smaller than the primary precipitates and were acicular shaped typically from 0.5 to 1 μm long. In the Ti alloys, the secondary precipitates formed typically in a bunched up fashion as colonies. In the Ti with C alloys, the secondary precipitates formed along the grain boundaries as discrete particles.

The equilibrium solubilities were measured after the homogenization heat treatment. In the X=2 Ti alloy, Ti was found to have an equilibrium solubility of 0.47 wt% Ti. In the X=6 Ti homogenized alloy, titanium had grabbed all the boron to form titanium borides leaving only the 2-17 phase. The solubility of Ti in the 2-17 phase was high (2.2 wt%). In the Ti with C alloys, the equilibrium solubility was found to be 0.02 to 0.06 wt% Ti for the X=2 and X=6 TiC alloys respectively. The equilibrium solubility as measured is probably less due to problems with the interaction volume of the beam and the many fine secondary precipitates. Additional work on the equilibrium solubility of titanium with carbon shows that it is much less and is below the detectable limit of EDS (See PART I and PART III).

Comparing the as-cast and homogenized microstructures, no changes in size or appearance were found in the primary or secondary precipitates of the titanium or titanium with carbon alloys. Dissolution and coarsening (Ostwald Ripening) was not observed at least to 1000°C which shows that the precipitates are stable at high temperatures.

While any second phases at grain boundaries can provide pinning, TiC precipitates seem to be a much better choice compared to their boride counterparts. First, the titanium carbides seem to form as discrete particles while the titanium borides seem to form in a continuous and bunched up fashion. In addition, since Ti and C are added together and have extremely low solid solubility, their addition does not alter the base alloy composition. Thus, they can be alloyed in existing alloys without reducing the specific properties of the base alloy. When titanium is added it will ultimately form borides, which changes the base alloy composition. The composition of existing alloys must be altered in order to get boride precipitation while maintaining the same amount of grain boundary and hard magnetic phases. In addition, the intrinsic properties of the base alloy will be reduced

from Ti addition since it has a much higher equilibrium solubility than a Ti with C addition.

PART III SOLUBILITY OF TITANIUM WITH CARBON IN THE $Nd_2Fe_{14}B$ SYSTEM

INTRODUCTION

In PART II, it was found that in the Nd-Fe-B-Ti system the Nd_2Fe_{17} and TiB_2 phases were the most stable and in the Nd-Fe-B-Ti-C system the $Nd_2Fe_{14}B$ and TiC phases were the most stable. Thus, titanium additions alone react with boron and reduce the hard magnetic properties by reducing the amount of 2-14-1 phase that forms. Titanium with carbon additions form TiC which is not detrimental to 2-14-1 phase formation or the resulting magnetic properties. In Part III, the solubilities of titanium with carbon additions are studied in more detail.

Enhanced high temperature stability of the microstructure of the 2-14-1 type magnets results from the grain boundary pinning effects of precipitates. To effectively prevent grain growth, a fine dispersion of precipitates must be formed since the maximum pinning force for grain boundaries from precipitates increases as the volume fraction of precipitates increases and as the size of the precipitates decreases.[78] A fine dispersion of precipitates can only be formed if the precipitating elements form from supersaturated solid solution. Thus, the solubilities of the precipitating elements in the liquid and solid phases must be known. In this section, the equilibrium and nonequilibrium solubilities of Ti with C in the liquid and solid phases will be examined in detail in order to better understand the precipitation process.

EXPERIMENTAL APPROACH

Compositions are given in the form $(Nd_{2/17}Fe_{14/17}B_{1/17})_{100-2X} + Ti_XC_X$ (Table 14). In this section, cast ingot and melt-spun samples were examined. The scale of the microstructure is much finer and is much more difficult to study in melt-spun samples compared to the as-cast samples. However, the alloy chemistry depends on the balance of free energies and should be similar in both types of samples. The solubilities in the ingot material could be determined in a direct fashion through scanning electron microscopy (SEM) and the solubilities of the melt-spun material could be related in an indirect fashion through studying changes in properties. TEM studies of melt-spun material provide additional information about the equilibrium solid solubility. Also, since the cooling rate varies greatly ($\approx 10^3$°C/s) between the two types of samples, any cooling rate dependance of solid solubility can be deduced.

Table 14 Composition of Alloys Studied

Alloy	Composition	Ti Add X=	C Add X=
Base	$Nd_{2/17}Fe_{14/17}B_{1/17}$	0	0
X=0.5 TiC	$(Nd_{2/17}Fe_{14/17}B_{1/17})_{100-2x} + Ti_xC_x$	0.5	0.5
X=0.75 TiC	$(Nd_{2/17}Fe_{14/17}B_{1/17})_{100-2x} + Ti_xC_x$	0.75	0.75
X=1 TiC	$(Nd_{2/17}Fe_{14/17}B_{1/17})_{100-2x} + Ti_xC_x$	1	1
X=2 TiC	$(Nd_{2/17}Fe_{14/17}B_{1/17})_{100-2x} + Ti_xC_x$	2	2
X=3 TiC	$(Nd_{2/17}Fe_{14/17}B_{1/17})_{100-2x} + Ti_xC_x$	3	3
X=4 TiC	$(Nd_{2/17}Fe_{14/17}B_{1/17})_{100-2x} + Ti_xC_x$	4	4
X=5 TiC	$(Nd_{2/17}Fe_{14/17}B_{1/17})_{100-2x} + Ti_xC_x$	5	5
X=6 TiC	$(Nd_{2/17}Fe_{14/17}B_{1/17})_{100-2x} + Ti_xC_x$	6	6
X=7 TiC	$(Nd_{2/17}Fe_{14/17}B_{1/17})_{100-2x} + Ti_xC_x$	7	7

RESULTS AND DISCUSSION

Liquid Solubility

In order to form an effective dispersion of precipitates to prevent grain growth, the precipitates should form out of supersaturated solid solution. In this way, a large number of fine dispersoids will form directly at the grain boundaries. To obtain an effective dispersion, the elements that form the precipitates must first have significant solubility in the liquid phase. The elements soluble in the liquid may then be soluble in the solid phase(s) that form upon solidification. Once the solubility limit of the liquid has been exceeded, primary precipitates will form in the liquid. The existence of carbides in high temperature ferrous based liquid is known in steel processing.[98,99] The primary precipitates are relatively large and are less effective at preventing grain growth although they may have other significant effects.[100]

As-Solidified Ingots

Initially as-solidified arc melted ingots were examined by SEM for TiC additions with X = 2,4,6 to stoichiometric 2-14-1. In all cases the ingots consisted of 2-14-1 phase, properitectic Fe, and an unresolved rare earth rich eutectic phase probably consisting of α-Nd and $Nd_1Fe_4B_4$ phases. In the as-solidified arc-melted X=2 TiC ingot, no primary TiC precipitates were found. EDS analysis of the as-solidified phases indicated that Ti was homogeneously distributed in the 2-14-1 and Fe phases on the scale of the analysis at levels of 1.30 wt% and 1.71 wt% respectively for the X=2 addition. In the X=4 and X=6 TiC as-solidified alloys, primary TiC precipitates were present throughout the microstructure. In the as-cast X=4 TiC alloy the primary carbides have a cubic shape and are indicated by the arrows (Figure 36). The equilibrium cubic shape of the carbides indicates that they

Figure 36 SEM micrograph of an as-cast X=4 TiC alloy. The primary TiC precipitates are marked with arrows.

formed first from the liquid. From EDS, the cubic precipitates were found to consist of only Ti and C. The X-ray diffraction scan of the X=4 TiC alloy verified that the cubic phase was TiC (Figure 37). Thus, for the rather undefined levels of superheat obtained during arc melting, the solubility of Ti with C in the liquid is found to be between 4 and 8 at% Ti+C. Due to the multiple meltings of the sample, it is expected that equilibrium was approximated in the melt and the level of liquid solubility measured approximates the equilibrium solubility limit.

Melt-Spun Ribbon

In order to further verify that the blocky TiC precipitates did not form during solidification, melt-spun ribbons were studied. By melt-spinning at high wheel speeds (45 m/s), high cooling rates on the order of 10^6 °C/s are obtained which causes the formation of a primarily amorphous or glassy structure.[63] This high cooling rate will not allow time for solid state reactions requiring diffusion such as TiC precipitation. An X-ray diffraction scan of a X=6 TiC alloy melt-spun at 40 m/s shows the presence of TiC in an amorphous matrix (Figure 38). In the X-ray scans, TiC was observed in the amorphous alloys beginning with the X=4 TiC alloy. X-ray scans do not accurately indicate the limit of liquid solubility due to the poor detectability of the low molecular weight TiC precipitates. Auger analysis was done on an optimally quenched melt-spun X=6 TiC alloy. In the melt-spun alloy, primary TiC precipitates similar to those observed in as cast ingots were found (Figure 39). The existence of secondary carbides could not be verified due to the resolution limit of the auger microscope but additional titanium and carbon were found distributed homogenously through out the matrix of the melt-spun ribbon.

While it is difficult to accurately measure the amount of Ti and C in solution in the amorphous phase, measuring the changes in the properties of this phase can give a good

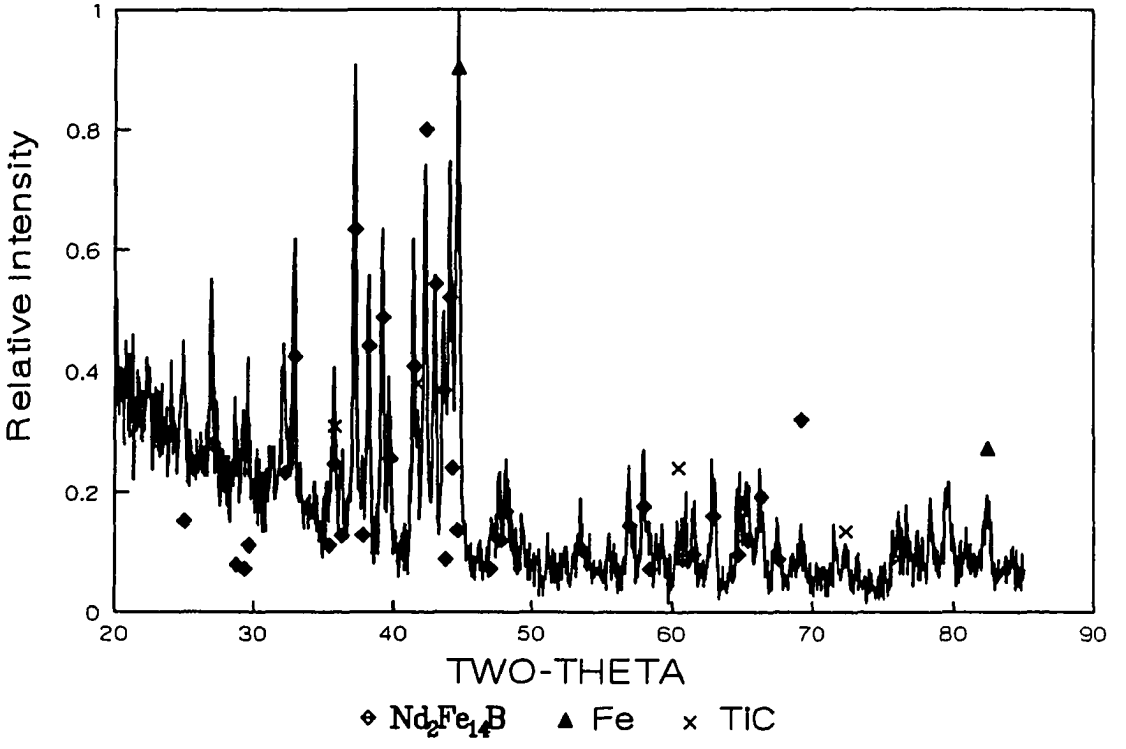

Figure 37 XRD of the as-cast X=4 TiC alloy.

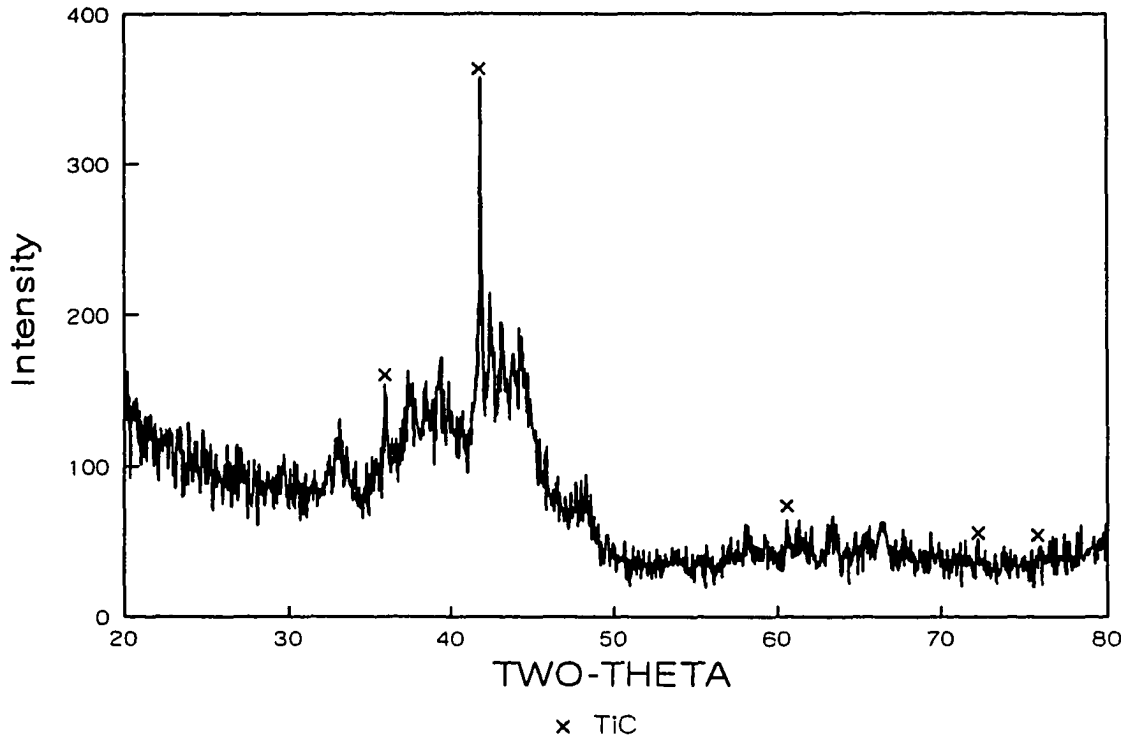

Figure 38 XRD of an X=6 TiC alloy which has been melt-spun at 25 m/s.

Figure 39 Auger micrograph of an X=6 TiC alloy melt-spun at 10 m/s. The primary TiC precipitates can be seen.

indication of the solubility limit. In Figure 40, the crystallization temperature of the 2-14-1 phase is plotted versus atomic percent Ti with C addition. It can be seen that between the X=2 and X=3 TiC alloys, the crystallization temperature reaches a plateau and further additions of Ti and C do not increase the crystallization temperature. This plateau region supports the hypothesis that the solubility limit of Ti with C in the glass has been reached. Taken as a whole, the evidence strongly supports a maximum solubility of Ti with C in the liquid phase of between X=2 to 3 TiC (4 to 6 at% Ti+C).

Solid Phase Solubility

While between 4 and 6 at% Ti+C can be maintained in the liquid phase, the level of solubility in the 2-14-1 phase must be independently determined. It is important to know both the nonequilibrium and equilibrium solubilities of Ti and C in the 2-14-1 phase. At least nonequilibrium solubility is necessary because to obtain an effective dispersion of precipitates, it is inherent that the precipitates form from supersaturated solid solution. This results in a fine and widely distributed array. The equilibrium solubility is important because any titanium or carbon left dissolved in the 2-14-1 phase will cause changes in the intrinsic magnetic properties.

2-14-1 Phase Nonequilibrium Solubility

Experiments were undertaken in both the arc-melted ingots and the melt-spun ribbons to find the maximum solubility of Ti with C in the 2-14-1 phase. In the arc-melted ingots, the level of Ti in the 2-14-1 phase was measured using EDS semiquantitative analysis. The amounts of Ti found in the 2-14-1 and α-Fe phases for the as-solidified arc-melted X=2, 4, and 6 TiC alloys can be seen in Table 14. These results show that Ti has at least a 1.3 wt% solubility in the 2-14-1 phase. This does not indicate

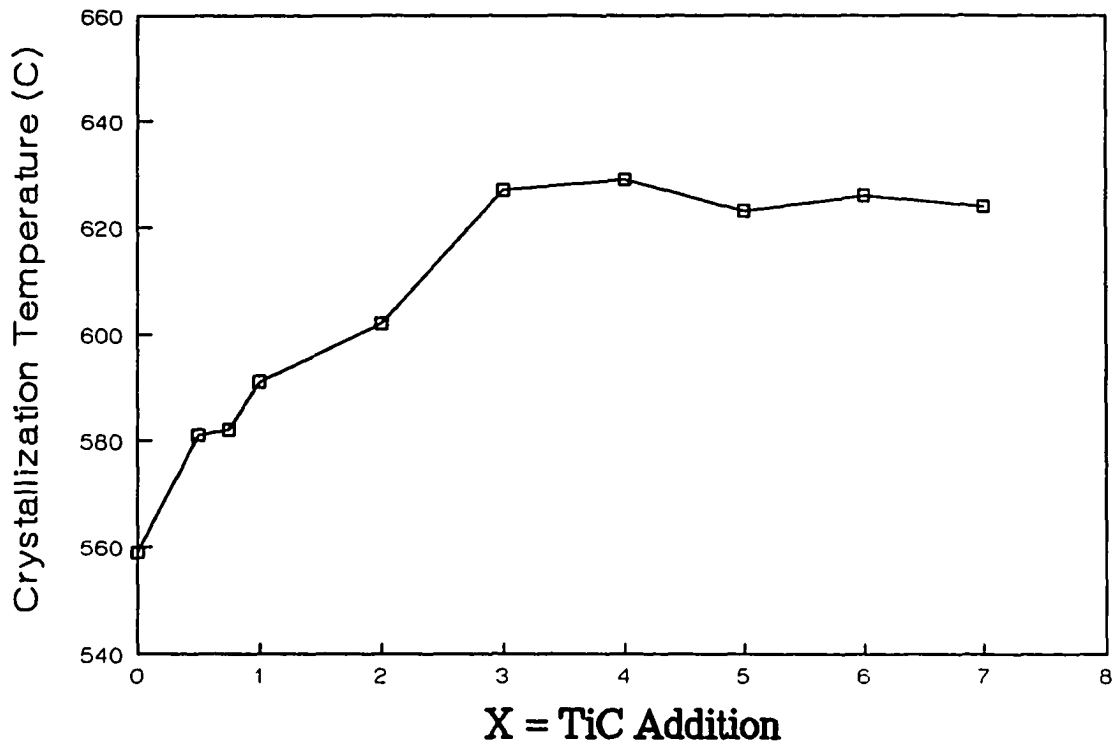

Figure 40 Variation in crystallization temperature of the 2-14-1 phase with TiC addition.

the maximum solubility in this phase due to competition with the properitectic iron phase which exists in the as-cast ingots. From Table 14, at least 1.7 wt% Ti is dissolved in the iron phase. In addition, during cooling and after solidification some titanium carbide precipitates are formed. This indicates the titanium must exist in supersaturated solid solution. Through the study of the arc-melted ingots, titanium is found to have a significant solubility in the 2-14-1 phase.

Table 14 Semiquantitative Analysis of Wt% Ti

Addition	X =	α-Fe	2-14-1
TiC	2	1.71	1.30
TiC	4	1.15	0.64
TiC	6	1.76	1.24

Through melt-spinning at high wheel speeds, the peritectic and eutectic reactions can be avoided upon solidification and a glassy or fine grained 2-14-1 phase material can be formed directly. Due to the extremely fine scale of the microstructure, changes in the physical properties as a function of alloy additions are used to detect elements in solution. Since it is known that C addition to the 2-14-1 phase lowers the Curie temperature[101], an amorphous phase was produced which after crystallization formed only the 2-14-1 phase and the Curie temperature was determined. In Figure 41, the Curie temperature versus TiC addition can be seen for samples heat treated at 650°C for one hour. From the figure it can be seen that the Curie temperature levels off between the X=2 and X=3 TiC alloys. This indicates that the solubility of Ti with C is between 4 and 6 at% Ti+C. This

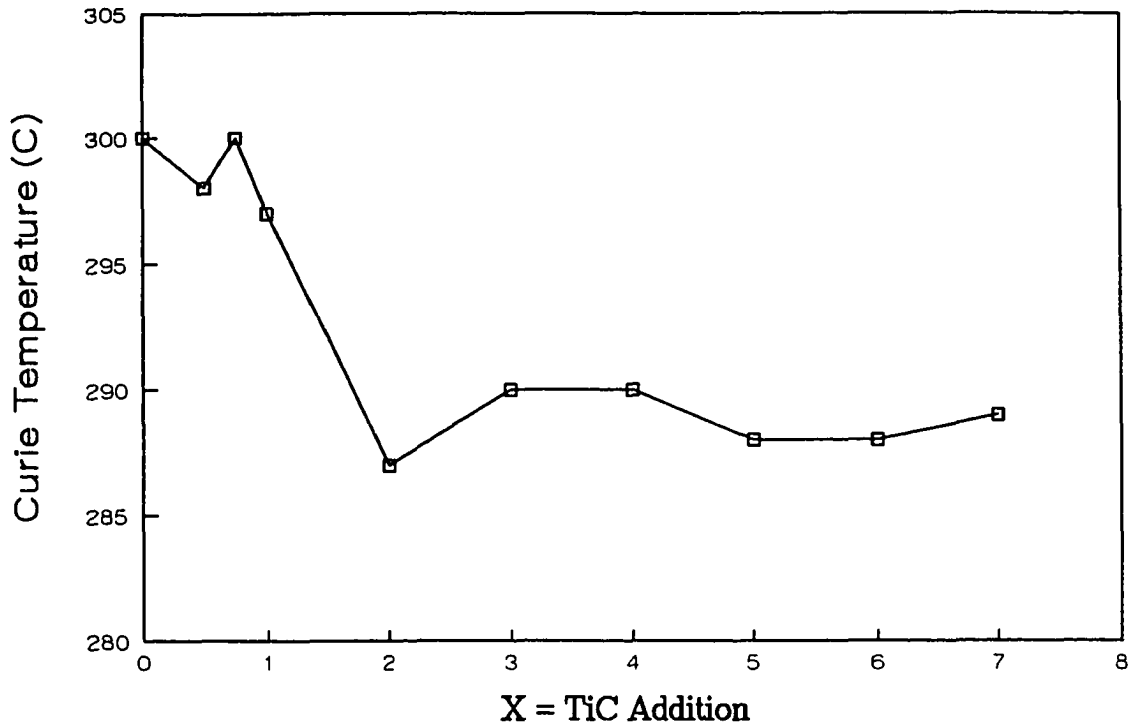

Figure 41 Variation in Curie temperature with TiC addition for melt-spun samples heat treated at 650°C for one hour.

is concurrent with the liquid solubility and shows the Ti with C present in the liquid remains present in the 2-14-1 phase under rapidly solidified conditions. As shown from the ingot data however, lower cooling rates allow time for some TiC precipitation during solidification. This is an indication that the solubilities as measured are nonequilibrium and that the titanium with carbon exists in supersaturated solid solution.

2-14-1 Phase Equilibrium Solubility

Samples of arc-melted ingots were homogenized at 1000°C for one week. During the homogenization heat treatment, many fine TiC acicular shaped precipitates from 0.5 to 1.0 μm long were formed in the microstructures of the X=2, 4 and 6 TiC alloys. The primary (labeled 1) and secondary (labeled 2) precipitates can be seen in the X=4 TiC homogenized alloy in Figure 42. This composite microstructure is found to consist of only two phases. XRD scans verify that the phases observed are 2-14-1 and TiC. In Figure 43, it can be seen that many of these precipitates formed on the properitectic iron dendrites which then subsequently reacted with the rare earth eutectic to form additional 2-14-1 phase. Note that in the melt-spun ribbon, there is no free iron present and the TiC precipitates will use the grain boundaries as sites for heterogeneous nucleation.

EDS was performed on the matrix 2-14-1 phase after the homogenization heat treatment and the solubility of titanium was found (Table 15). Thus, the equilibrium solubilities are found to be less than or equal to 0.06 wt % Ti in either the X=2, 4, or 6 TiC homogenized alloys. The equilibrium solubility may be less due to the formation of the many precipitates in the microstructure. Due to the spot size and interaction volume of the electron beam, it is very difficult to find an area without carbide influence. Nevertheless, the loss of Ti and C from the 2-14-1 phase indicates that the equilibrium solubility of Ti with C in the 2-14-1 phase is very low.

Figure 42 SEM micrograph of a X=4 TiC alloy homogenized at 1000°C for one week. The primary and secondary TiC precipitates are labeled 1 and 2 respectively.

Figure 43 SEM micrograph of the X=4 TiC homogenized alloy. The secondary carbides trace out the prior iron dendritic boundaries which have since homogenized.

Table 15 Semiquantitative Analysis of wt% Ti dissolved in the 2-14-1 phase

Alloy	(wt%) 2-14-1
X=2 TiC	0.06
X=4 TiC	0.00
X=6 TiC	0.02

To determine the equilibrium solubility in melt-spun samples, amorphous ribbons were heat treated at 800°C for 8 hours. Again the Curie temperature was used as a probe of the material. In Figure 44, the Curie temperature is graphed versus TiC addition. It can be seen that within experimental error a uniform Curie temperature is found independent of composition. Also, the average Curie temperature of 312°C is found which is representative of the unalloyed stoichiometric $Nd_2Fe_{14}B$ phase.[102] These data indicate that after the 800°C heat treatment most or all of the Ti and C precipitated out of supersaturated solid solution.

The solubility of TiC in melt-spun ribbons was further investigated with the TEM. An X=6 TiC alloy melt-spun at 45 m/s was heat treated at 750°C for 1 and 24 hours (see Figures 20 and 45 respectively). The 750°C heat treatment was chosen to find the beginning stages of precipitation since the Curie temperature data indicated that precipitation hadn't started at 650°C but was complete at 800°C. Secondary TiC precipitation has occurred at 750°C (Figure 44). After the 1 hour heat treatment, the precipitates are found to be not completely formed and possibly semicrystalline in nature. After the 24 hour heat treatment the carbides have a much sharper and a more cubic appearance (Figure 45). Using EDS and PEELS, no dissolved Ti was found next to

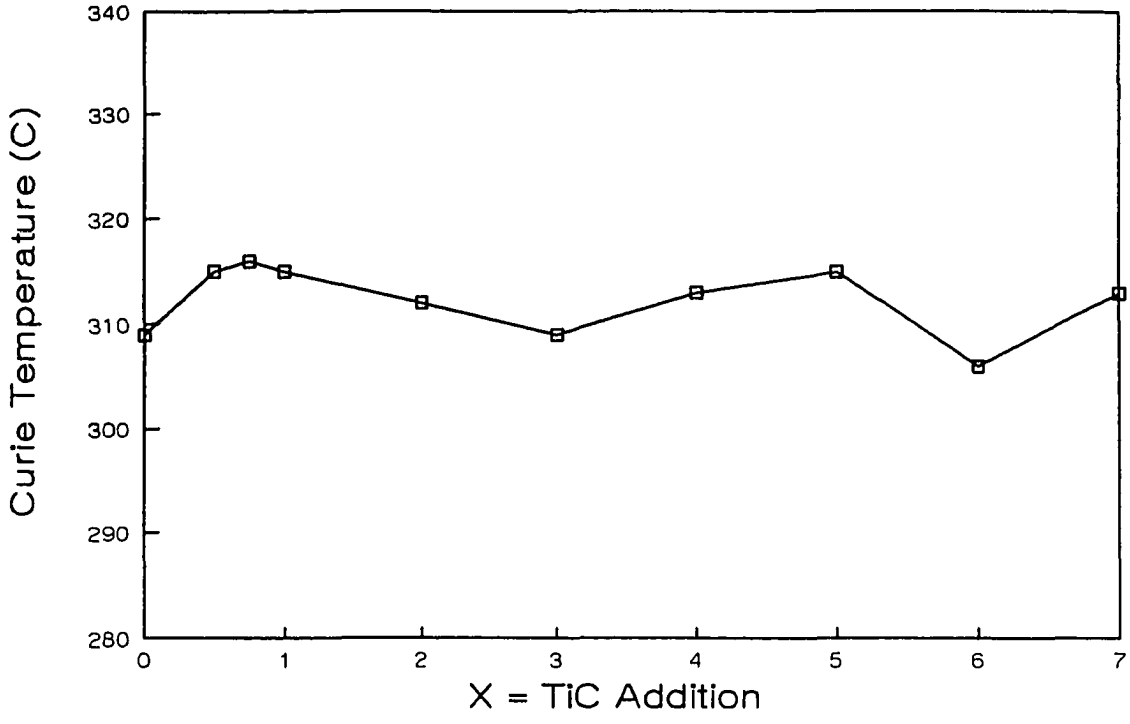

Figure 44 Variation in Curie temperature with TiC addition for samples heat treated at 800°C for 8 hours.

Figure 45 TEM micrograph of an X=6 TiC alloy melt-spun at 45 m/s and then annealed at 750°C for 24 hours. Note the distribution of 10-20 nm cubic TiC precipitates (arrows) and the fine spotted SAD.

the precipitates or anywhere else in the 2-14-1 grains after the 1 hour anneal. This further confirms the extremely low value of equilibrium solubility of Ti and C in the $Nd_2Fe_{14}B$ phase.

It should be noted that these results are in contrast to those of Ti alone. Due to TiC's extremely high free energy of formation (-22.0 Kcal/g-at)[97], C essentially pulls the Ti out of solid solution and causes the formation of the TiC. If Ti is added alone to stoichiometric 2-14-1, Ti borides will form. In this case however there is a competition between using the boron to form the Ti boride and using the boron to form the 2-14-1 phase. This results in an equilibrium where some of the Ti remains dissolved in solid solution. In stoichiometric 2-14-1 alloys containing only Ti below the solubility limit, Ti is found to have an equilibrium solubility of 0.47 wt% in the 2-14-1 phase (see PART II).

SUMMARY

The liquid and nonequilibrium and equilibrium solid solubilities was found for Ti and C in the Nd-Fe-B-Ti-C system. The solubility limit of Ti with C in the liquid phase was found to be between X=2 to 3 TiC (4 to 6 at% Ti+C). In alloys containing additional amounts of Ti and C, primary TiC precipitates are found to form in the liquid. The solubility of Ti and C in the 2-14-1 phase was found to equal the liquid solubility. The measured value of nonequilibrium solubility was found to be cooling rate dependant. It also depends on the competition between solubilities of other phases. In the arc-melted ingots, the observed solubility is less than the maximum which is consistent with the multiphase microstructure and the lower cooling rate. From studies of melt-spun ribbons and arc-melted ingots, the equilibrium solubility of Ti with C in the 2-14-1 phase is found to be very low (< = 0.06 wt% Ti).

Titanium carbide represents an exemplary addition to the 2-14-1 system due to its liquid and solid solubility. It has a significant liquid solubility which can be maintained during solidification in the solid phases such as in the glass or the 2-14-1 phase. This liquid and solid solubility is important because when the titanium and carbon are dissolved, they change the intrinsic properties of the phase. The intrinsic changes in the properties of the liquid and solid phases will be studied in the subsequent PARTS IV, V and VI. Since TiC is found to have essentially no equilibrium solubility in the 2-14-1 phase, it can be precipitated out of supersaturated solid solution which allows the extrinsic properties of the 2-14-1 phase to be altered and improved while the excellent intrinsic properties of the 2-14-1 phase are maintained.

PART IV ALTERING THE COOLING RATE DEPENDANCE OF PHASE FORMATION DURING RAPID SOLIDIFICATION IN THE $Nd_2Fe_{14}B$ SYSTEM

INTRODUCTION

In PART III, the liquid and solid solubilities of Ti with C in the Nd-Fe-B-Ti-C system was studied. TiC was found to have a significant liquid solubility (between X= 2 to 3), a significant nonequilibrium solid solubility (X= 2 to 3 in melt-spun samples), and essentially no equilibrium solid solubility. Thus, TiC addition is found to be a superb addition allowing the formation of a composite 2-14-1 and TiC microstructure. In Part IV, the intrinsic changes that are occuring when Ti and C are dissolved in the liquid or solid solutions are being studied

The use of phase diagrams is very widespread in the permanent magnet industry as well as in material science as a whole. Phase diagrams have limitations however because they only indicate the equilibrium phases. Under nonequilibrium conditions, kinetic as well as thermodynamic factors determine what phases and the microstructures that will form. In processes such as solidification, equilibrium conditions are never achieved. Therefore the effects of time and cooling rate are very important. By varying the cooling rate, amorphous and metastable phases can often be formed which are not predicted by phase diagrams. Phase transformations such as those occurring upon solidification are best described through the use of continuous cooling transformation (CCT) diagrams. A continuous cooling transformation (CCT) diagram represents phase formation during the solidification process under continuous cooling conditions for a wide range of cooling rates from rapid solidification to equilibrium cooling. CCT diagrams incorporate kinetic as well as thermodynamic effects on the phase transformation process. These type of diagrams facilitate the study of the phase transformation kinetics through looking at the effects of time by varying the cooling rate. In the steel industry, continuous cooling transformation (CCT) diagrams are used widely in processing and can describe the phase transformations

occurring during cooling after austenization leading to specific microstructures such as martensite, pearlite and bainite.[103-105] The use of CCT diagrams to describe the solidification process in permanent magnet alloys could be very useful as well. Since the transformations in steels are solid state, the time frame is considerable slower than when dealing with solidification. For steels the CCT diagram provides a quantitative road map for the development of the desired microstructure. In the present case the CCT diagram is a conceptual aid which may help in understanding the solidification process.

In melt-spinning, the cooling rate can be controlled by changing the wheel tangential velocity. The highest wheel speeds correspond to cooling rates in excess of 10^6 K/s.[106] At slower wheel speeds and to a first approximation, the mean cooling rate in the vicinity of the solidification point is found to decrease linearly with wheel speed.[107] Due to the extremely high cooling rates, the development of quantitative CCT diagrams would be difficult for rapid solidification processing (RSP). However qualitative representations of the rapid solidification process in the $Nd_2Fe_{14}B$ system are possible and are conceptually useful. A model CCT diagram has been developed for a stoichiometric $Nd_2Fe_{14}B$ alloy based on experiments for this dissertation and from general knowledge of the permanent magnet literature.

Unlike phase diagrams, whose regions show the stability of phases at certain temperatures and compositions, CCT diagrams indicate regions of temperature and time where phase transformations occur. A given CCT diagram can represent only one composition and should be used only for minor alloy modifications. In the absence of metastable phases, a model CCT diagram can be developed from considerations of the equilibrium phase diagram. The development of the CCT diagram (Figure 46) from the ternary isopleth at the tie line between Fe and $Nd_2Fe_{14}B$ representing these equilibrium phase reactions (Figure 47)[108] starts with the identification of the phases which one would

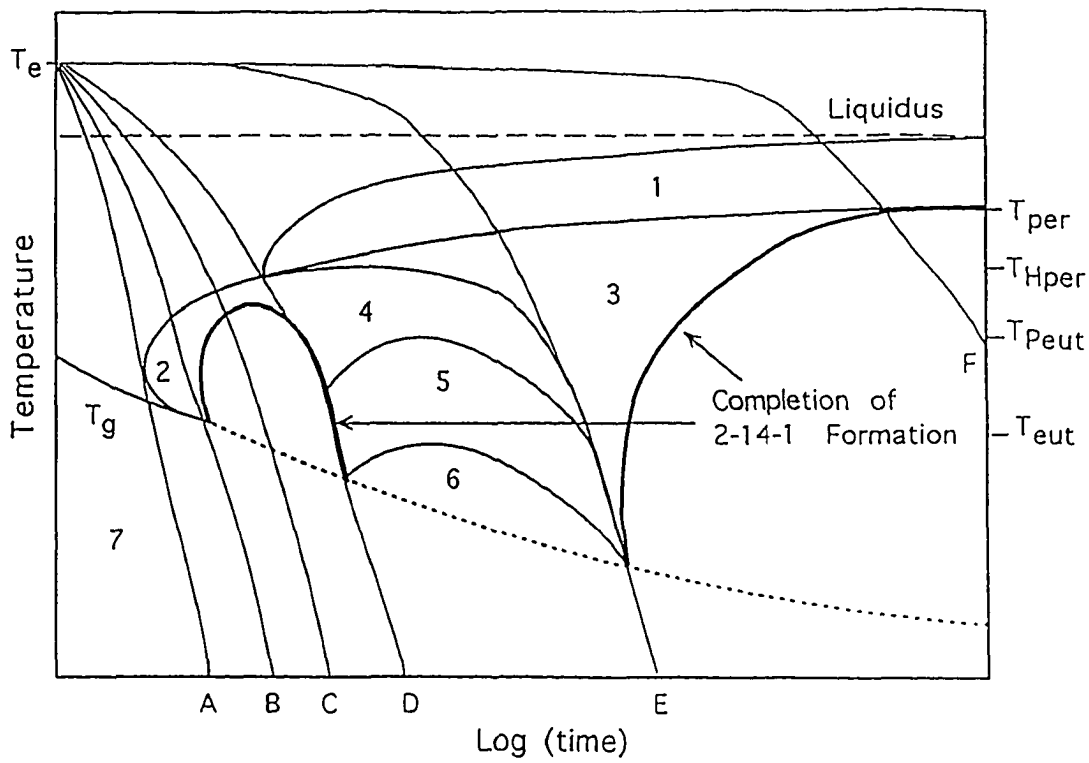

Figure 46 Model CCT diagram for stoichiometric $Nd_2Fe_{14}B$. The reaction regions are labeled 1-7 and are identified in Table 16. Five cooling curves labeled A-E are shown. Temperatures corresponding to the phase diagram of Figure 47 are labeled on the Y-axis.

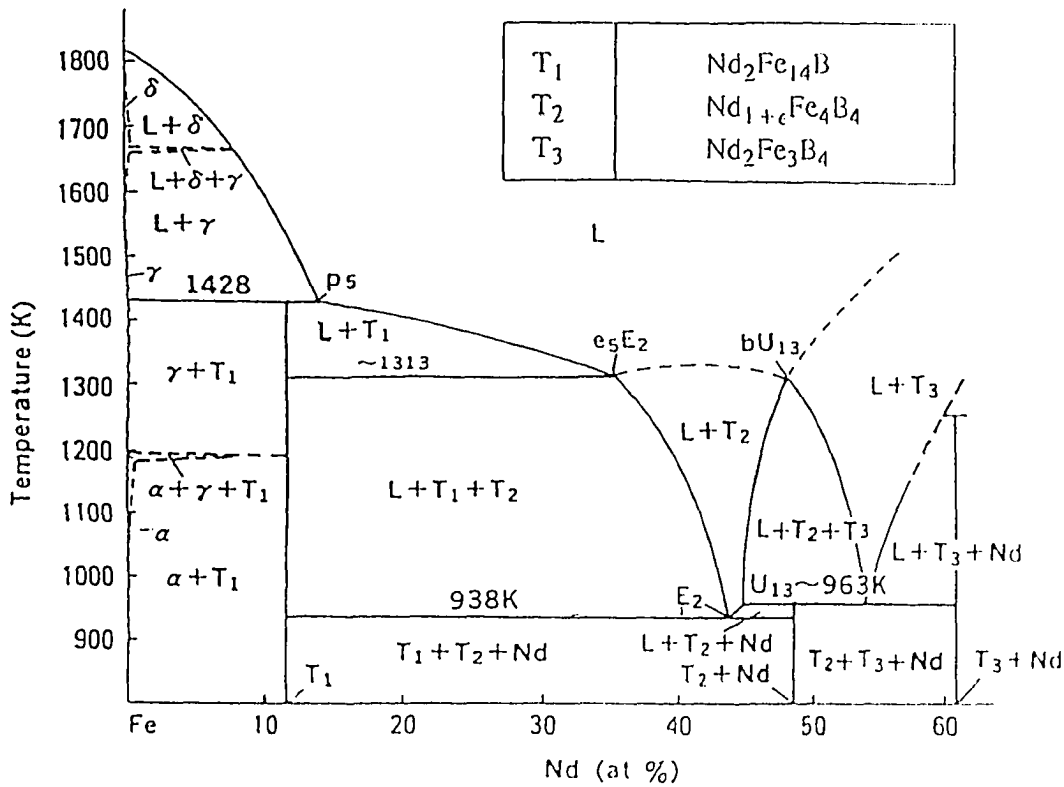

Figure 47 A vertical section of the Nd-Fe-B phase diagram along the tie-line between Fe and T_1.[108]

expect for the given composition under non-equilibrium conditions and the reactions by which they form. On the CCT of Figure 46, 7 regions are indicated which are representative of different phase reactions. The reaction regions present on the CCT diagram are identified in Table 16. Reaction regions 1 through 6 are consistent with the observed ternary phase equilibrium reactions. Reaction 7 is the liquid to glass transition and is not represented on the ternary isopleth but is well known.

Table 16 Reaction Regions of CCT Diagram

Region	Reaction*	Type	Description
1	$L > Fe + L_1$	Peritectic	Properitectic Iron Reaction
2	$L > T_1$	Transition	Direct Crystallization
3	$L + Fe > T_1$	Peritectic	Peritectic Reaction
4	$L > T_1 + L_1$	Peritectic	Hyperperitectic Reaction
5	$L > T_1 + T_2 + L_1$	Eutectic	Proeutectic Reaction
6	$L > T_1 + T_2 + Nd$	Eutectic	Ternary Eutectic Reaction
7	L > Glass	Transition	Liquid to Glass Transition

* The phase reaction labels are consistent with the ternary isopleth of Figure 2

On the CCT diagram only the beginning of the phase reactions are drawn except the 100% reaction lines are drawn for the 2-14-1 phase formation. Six representative cooling curves (A-F) are drawn on the CCT diagram, starting from the melt spinning ejection temperature (T_e). Since the free surfaces, wheel surfaces and the center of the ribbons cool with different cooling rates, a single cooling curve is not entirely representative. However, the changes in cooling rate dependance studied in this paper are much larger than the surface effects so the representative cooling curves (A-F) can be simply viewed as lines having width. The X-axis is a log scale so a wide range of cooling rates can be

shown representative of RSP, ingot cooling, and equilibrium cooling. Since the cooling rate range from rapid solidification to equilibrium cooling is at least 12 orders of magnitude, the CCT diagram has been foreshortened to show all of the essential features.

The left hand side of the CCT diagram can be drawn from the observation that at sufficiently high cooling rates it is possible to form a glass. This is represented in cooling curve A, where a 100% amorphous structure is formed as the alloy is cooled below the glass transition temperature before crystalline phases can nucleate. The right hand side of the diagram is determined by equilibrium cooling. Cooling curve F represents near equilibrium cooling. At the liquidus, Fe begins to precipitate. As the temperature decreases, the composition of the liquid moves along the liquidus toward point p_5 on the equilibrium isopleth and the amount of solid Fe increase in accordance with the lever law. When the peritectic temperature is reached the Fe and the liquid react to form the 2-14-1 phase.

In the powder route to making 2-14-1 type magnets, solidification rates during casting occur between cooling curves D and E. In this region, the solidification sequence begins with the properitectic reaction and free iron formation. Then the peritectic reaction occurs. The peritectic reaction requires bulk diffusion and is very sluggish. The ingot cooling rates are fast enough in this region to allow only limited diffusion which causes bulk segregation in both the liquid and solid phases. The solidification sequence after the peritectic reaction occurs through the hyperperitectic, proeutectic and ternary eutectic reaction regions as seen by following the liquidus curve in the isopleth.[108,109]

When the cooling rate is sufficient to undercool below the peritectic temperature, direct solidification of the 2-14-1 phase occurs. Cooling curve B gives a fully crystallized 2-14-1 single phase microstructure. Material cooled with cooling rates intermediate between A and B is partially crystalline and represents an overquenched condition. The

optimum cooling rate would occur slightly faster than cooling curve B. This will give the ideal microstructure consisting of an almost completely crystallized nanosized grain structure with a small amount of amorphous grain boundary phase. Optimum grain sizes are generally found to be between 20 to 100 nm[110] which is below the single domain particle size.[82] The grain boundary amorphous phase is important to magnetically decouple adjacent grains.[113] In cooling curve C, a completely crystalline 2-14-1 structure is formed but the alloy is in the underquenched condition. During cooling and after crystallization is complete, the grains have time to grow above the optimum grain size. This grain growth after crystallization occurs as the ribbon is cooling in the air and can be called self annealing.

Altering the cooling rate dependance of phase formation has been done to a limited extent in permanent magnet processing. Most commercial alloys contain excess Nd. This is to form a rare earth rich grain boundary phase and also as a liquid phase sintering aid but it also moves the composition nearer to the ternary eutectic composition.[72,112,113] Through utilization of the model CCT diagram, the effect of excess Nd can be visualized. Excess Nd inhibits or if enough is added, prevents the formation of properitectic iron. On the CCT diagram, the properitectic iron region (Region 1) is reduced and moved to the right to longer times with Nd addition. Also, as the composition moves closer to the eutectic reaction, the liquidus is reduced. This allows for less undercooling to avoid the peritectic and eutectic reactions and enhanced glass forming ability results. On the CCT, this pushes the start of the liquid to crystalline 2-14-1 phase formation region (Region 2) to the right to longer times.

EXPERIMENTAL APPROACH

Six modified alloys along with a stoichiometric base alloy, used as a reference, were studied (see Table 17). While commercial alloys vary considerably from stoichiometry, it was chosen as the starting point for simplicity. The compositions were chosen so that the effects of Ti and C alone could be evaluated and then compared to the effects of adding Ti with C to the base alloy. Careful control over all the melt-spinning parameters along with changes in wheel speed led to concise and reproducible cooling rates. Each alloy was melt-spun at wheel tangential velocities of 5, 10, 15, 20, 25, and 30 m/s. After magnetic measurements were obtained for each run, additional wheel speed runs were done for each particular alloy to find the optimum wheel speed. The term optimum wheel speed will be used to describe the wheel speed which gives the highest value of energy product for a given composition of melt-spun material. By observing the phases formed and the resulting magnetic properties at each wheel speed, the development of the microstructure can be traced. From this, the regions of wheel speed for each alloy which determine the level of properitectic iron formation, nucleation and grain growth, and glass formation are found.

Table 17 Composition of Alloys Studied

Alloy	Composition	Ti Add X=	C Add X=
2-14-1	$Nd_{2/17}Fe_{14/17}B_{1/17}$		
X=2 Ti	$(Nd_{2/17}Fe_{14/17}B_{1/17})_{100-x} + Ti_x$	2	
X=6 Ti	$(Nd_{2/17}Fe_{14/17}B_{1/17})_{100-x} + Ti_x$	6	
X=2 C	$(Nd_{2/17}Fe_{14/17}B_{1/17})_{100-x} + C_x$		2
X=6 C	$(Nd_{2/17}Fe_{14/17}B_{1/17})_{100-x} + C_x$		6
X=2 TiC	$(Nd_{2/17}Fe_{14/17}B_{1/17})_{100-2x} + Ti_xC_x$	2	2
X=6 TiC	$(Nd_{2/17}Fe_{14/17}B_{1/17})_{100-2x} + Ti_xC_x$	6	6

RESULTS

Magnetic Measurements

Optimum Wheel Speed

In Figures 48, 49, and 50, energy product versus wheel speed graphs are presented for X=0 (base), 2, and 6 alloys of Ti, C and TiC respectively. All the magnetic properties as a function of composition and wheel speed are listed in Table 18. The alloying additions are found to cause large changes in the optimum wheel speeds. Thus the ideal cooling rate necessary to obtain the optimum properties is altered. The optimum is found to be 21.25 m/s in base. Ti addition to the 2-14-1 phase causes a large shift in the optimum wheel speed to lower velocities. In the X=2 and X=6 Ti alloys, the optimum wheel speed is shifted down to 15 and 10 m/s respectively. C addition is found to also cause a shift in the optimum wheel speed. In the X=2 and X=6 C alloys, the optimum is shifted down to 20 and 12.5 m/s respectively. In the Ti with C alloys the change in optimum wheel speed follows closely the amount of Ti addition. In the X=2 and X=6 TiC alloys, the optimum is 16.25 and 10 m/s respectively.

Optimum Magnetic Properties

Significant differences between alloying additions appear in the peak values of the energy product. In Figure 51, the optimum energy product versus alloying addition is graphed. The optimum energy product in the base alloy is 8.8 MGOe. In the X=2 alloys, the energy product is increased over the base alloy. In the X=6 alloys, the energy product is reduced with Ti or C additions. In the X=6 TiC alloy, which represents a 12 at% addition, the energy product is enhanced over the base alloy.

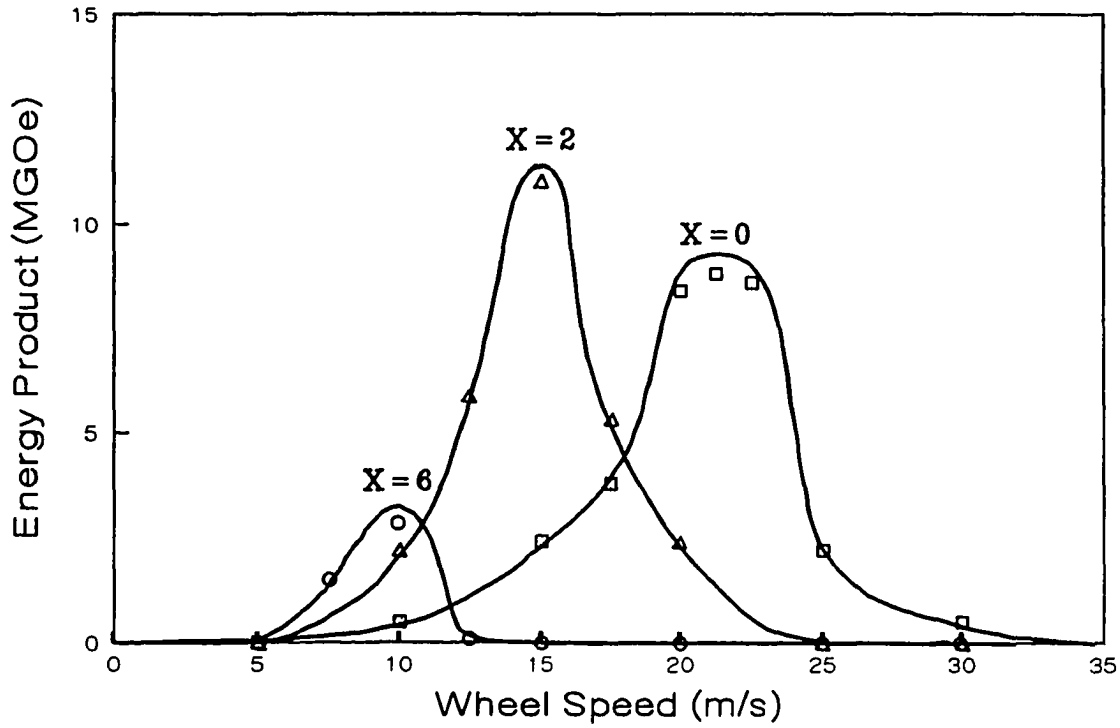

Figure 48 Energy product versus wheel speed for the base alloy and for Ti modification.

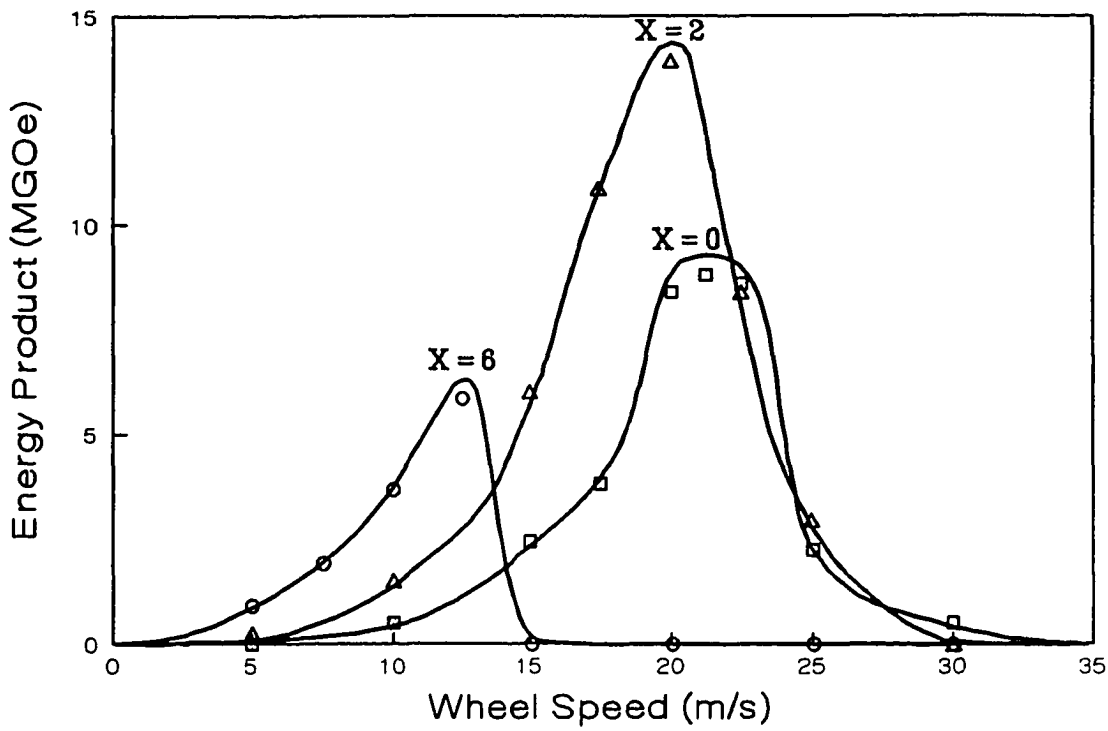

Figure 49 Energy product versus wheel speed for the base alloy and for C modification.

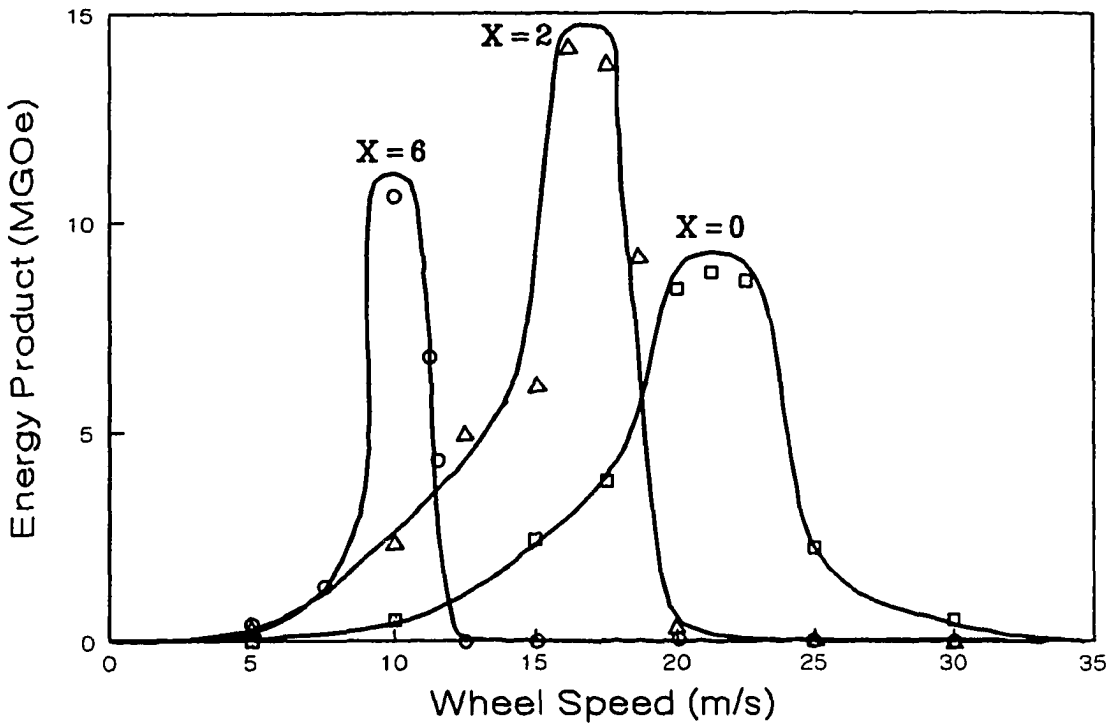

Figure 50 Energy product versus wheel speed for the base alloy and for TiC modification.

Table 18 Magnetic Properties

WH.SP. (m/s)	Msat (G)	Remanence (G)	Coercivity (Oe)	BHmax (MGOe)
		X=0 (base)		
5	14,760	1190	140	0.0
10	14,280	3520	710	0.5
15	15,150	6570	2530	2.4
17.5	15,330	7260	3920	3.8
20	14,270	8280	6930	8.4
21.25	15,270	8670	5420	8.8
22.5	15,010	8590	7500	8.6
25	15,360	7190	4600	2.2
30	13,830	4470	810	0.5
		TiC Addition X = 2		
5	14,160	2400	420	0.2
10	14,330	6410	3010	2.2
12.5	14,900	7540	4770	4.7
15	14,140	8200	7890	5.8
16.25	14,660	9110	8720	13.5
17.5	14,460	9060	10,240	13.1
18.75	14,620	8430	8960	8.8
20	13,510	4880	540	0.3
25	13,450	3440	180	0.0
30	14,110	3080	170	0.0
		TiC Addition X = 6		
5	14,190	3410	680	0.4
7.5	14,110	5370	1390	1.3
10	14,390	8500	8490	10.6
11.25	13,790	7680	6290	6.8
11.5	13,960	7210	4770	4.3
12.5	12,480	3370	220	0.0
15	12,090	2200	110	0.0
20	12,810	3470	400	0.1
25	12,330	890	40	0.0
30	12,900	1340	60	0.0

Table 18 Continued

WH.SP. (m/s)	Msat (G)	Remanence (G)	Coercivity (Oe)	BHmax (MGOe)
Titanium Addition X = 2				
5	13,970	1840	270	0.0
10	14,080	5760	2540	2.2
12.5	14,170	7430	5540	5.8
15	14,260	8440	8380	11.0
17.5	14,020	8130	7950	5.3
20	13,780	7190	6350	2.4
25	12,180	110	10	0.0
30	13,220	2020	70	0.0
Titanium Addition X = 6				
5	11,370	1260	100	0.0
7.5	12,450	5090	2730	1.5
10	12,040	7080	5250	2.9
12.5	11,190	3360	340	0.1
15	11,060	1550	80	0.0
20	10,660	0	0	0.0
25	10,120	0	0	0.0
30	10,530	0	0	0.0
Carbon Addition X = 2				
5	13,730	2360	360	0.2
10	14,320	5710	1800	1.5
15	14,120	7610	4820	6.0
17.5	14,700	8750	6040	10.8
20	14,620	9080	8270	13.9
22.5	14,340	8220	6830	8.4
25	14,130	6870	7310	2.9
30	13,570	3410	140	0.0
Carbon Addition X = 6				
5	15,050	5080	770	0.9
7.5	15,000	6390	1280	1.9
10	14,580	7350	2440	3.7
12.5	14,590	8320	4220	5.9
15	13,740	3460	250	0.0
20	13,780	740	20	0.0
25	12,970	0	0	0.0
30	13,140	0	0	0.0

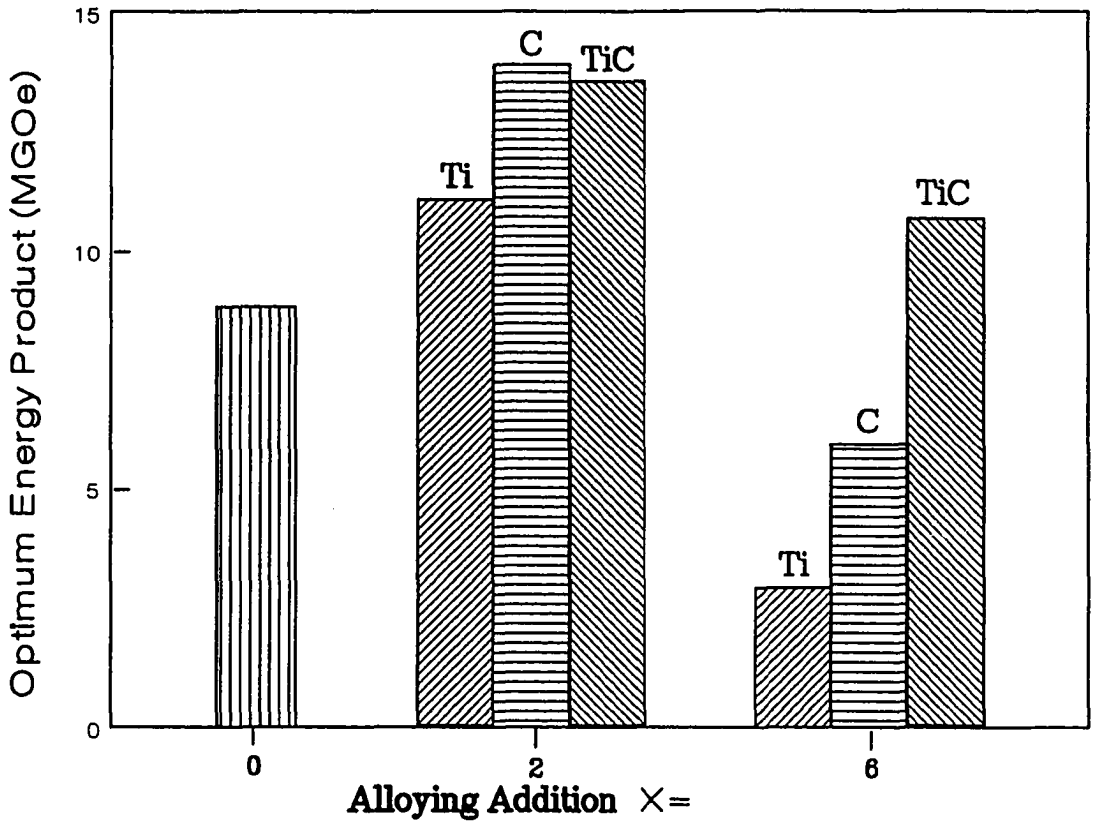

Figure 51 Optimum energy product versus the alloying addition.

X-Ray Diffraction

Alloying additions can cause significant changes in the phases formed at a particular cooling rate. The optimum magnetic properties are not only dependant on the grain size of the hard magnetic phase but depend on the formation of other phases as well. For each melt-spun sample, X-ray diffraction scans were obtained. The phases found in the optimally quenched samples will be explicated. The base, X=2 Ti, and X=2 TiC alloys are found to be single phase 2-14-1. In the X=2 C alloy, properitectic iron is present. In the X=6 C alloy, the properitectic iron peak is greatly enhanced indicating a larger amount of free iron is formed. In the X=6 Ti alloy, 2-14-1 and Nd_2Fe_{17} phases are found. In the X=6 TiC alloy, 2-14-1 and TiC phases are found.

DISCUSSION

Regional Wheel Speeds

For each composition, regions were defined on the BHmax versus Wheel Speed plots in order to analyze the data. These regions correspond to the general concepts of overquenching and underquenching but an attempt has been made to quantify the definitions in order to show the changes in cooling rate dependance of phase formation brought about from the alloy modifications. Region 1 shows the presence of free iron which is formed through the properitectic reaction. The limit of region 1 indicates the minimum cooling rate necessary to avoid peritectic microsegregation. Even though other soft magnetic phases can form at slow cooling rates, in this paper, the chief interest is the formation of properitectic iron since that is what forms at the stoichiometric 2-14-1 composition. Region 3 is defined as a region which is cooled fast enough to form an amorphous or not fully crystallized structure. X-ray diffraction was used to verify the glass structure. Since determining the degree of crystallinity through X-ray scans is imprecise, the lower limit of region 3 was defined as the wheel speed giving a coercivity equal to 1000 Oersteds. This value was chosen from a study of the exothermic crystallization energies versus wheel speed for melt-spun stoichiometric 2-14-1 alloys (see PART V). The 1000 Oe value of coercivity corresponds to an approximate 35% glass / 65% crystalline microstructure. The region between region 1 and region 3 will be then designated region 2. In this region, grain nucleation and growth of the hard magnetic phase and grain growth during the self-annealing stage are important. The nucleation rate of the 2-14-1 grains is significant because more nuclei means less growth until impingement occurs between neighboring grains. The driving force for this type of grain growth is the exothermic crystallization energy released from the metastable glass to

crystalline transition. After complete crystallization, the grains can grow during the self-annealling stage. The driving force for this type of grain growth is the reduction in surface energy through the reduction in grain boundary surface area per unit volume. The regions found for each alloy along with the optimum wheel speeds are shown in Figure 52.

Base Alloy

The limit of region 1 is at 17.5 m/s. This extended region is due to the large properitectic region (75°C) which is difficult to cool through without avoiding the precipitation of α-iron. On the CCT diagram (Figure 46), the cooling rate achieved in the 17.5 m/s sample would be equivalent to a cooling rate just slower than cooling curve D. The formation of large inclusions of free iron is the reason for the drastic diminution of coercivity seen at this wheel speed (17.5 m/s). Region 3 of glass formation starts at approximately 29.8 m/s (extrapolated to 1000 Oersteds). On the CCT diagram, this cooling rate would be equivalent to a cooling curve just to the left of cooling curve B. Region 2 thus lies from 17.5 to 29.8 m/s and corresponds to cooling rates between cooling curves B and D on the model CCT diagram. This represents a large region where grain nucleation and growth of the hard magnetic phase along with grain growth during self annealing are the events determining the value of energy product during cooling.

Titanium Addition

Ti is found to have a large effect on the glass to crystalline transition region. As Ti is added to the 2-14-1 phase, the crystallization temperature is raised (see PART VI). This essentially stabilizes the glass formation region. On the CCT, this will increase the glass to crystalline transition temperature and will move the bottom of the CCT diagram to higher temperatures. Also, Ti addition has a large effect on the start of

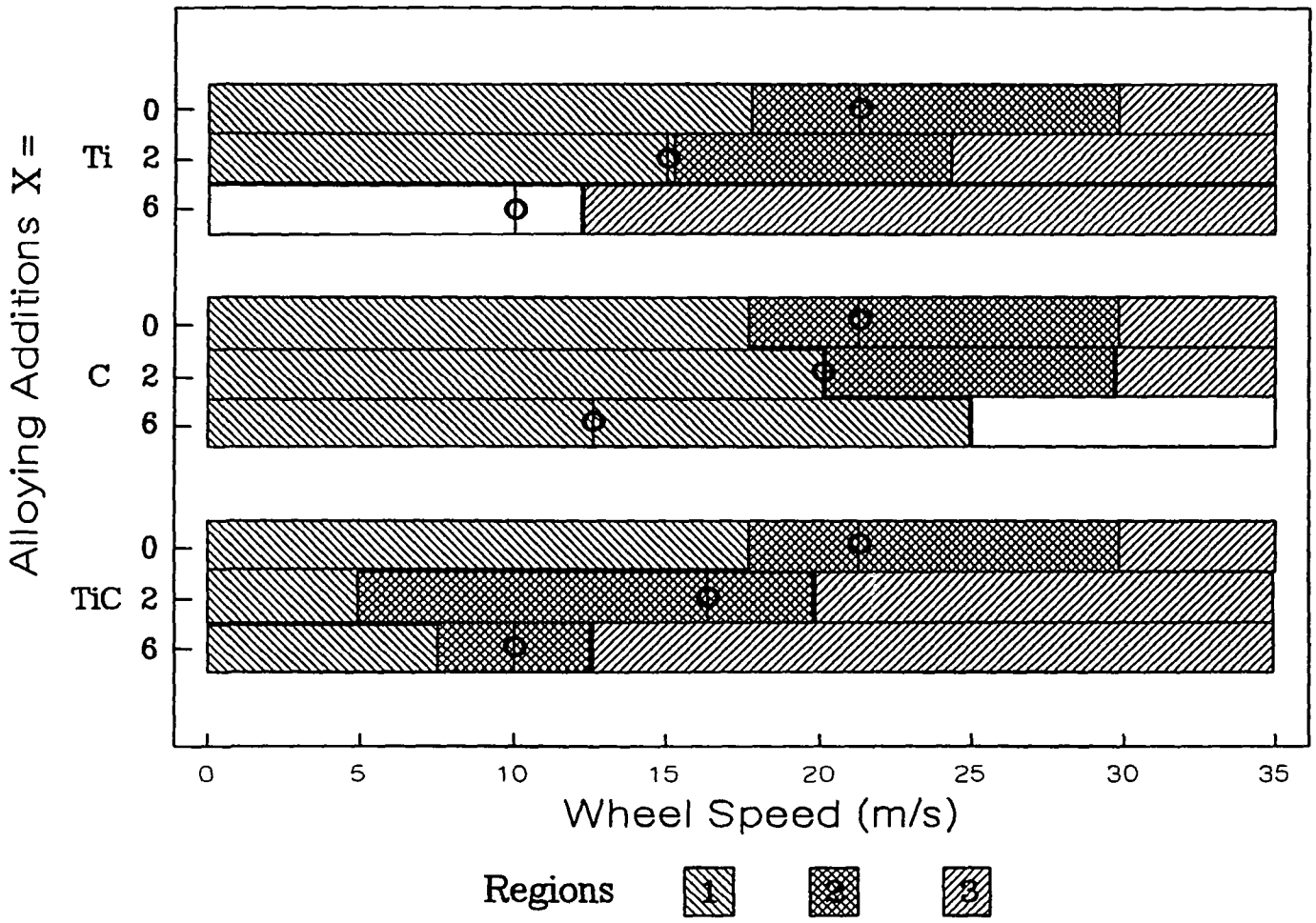

Figure 52 Regional wheel speeds for the Ti, C, and TiC alloys. Regions 1, 2, and 3 are indicated. The unhatched areas are undefined. The optimum wheel speeds are shown with the symbol Φ.

the liquid to crystalline 2-14-1 transition region. In the X=2 Ti and X=6 Ti alloys, region 3 is moved down from 29.8 m/s in the base alloy to 24.2 and 14.5 m/s respectively. This essentially moves the nose or the start of the liquid to crystalline transition region to the right to longer times. This is indicative of the enhanced glass forming ability.

In the X=2 Ti alloy, region 1 is moved down slightly to 15 m/s. In the X=6 Ti alloy, there is no region 1 because there is found to be no free iron precipitation. In the X=6 Ti alloy, the liquid solubility is exceeded and primary TiB_2 precipitates form in the liquid (see PART II). This causes a depletion of the boron content which causes 2-14-1 and 2-17 phases to crystallize. Since the solidification sequence has been changed in the X=6 Ti alloy, the model CCT diagram is no longer valid. The X-ray diffraction scan of the X=6 Ti optimally quenched alloy can be seen in Figure 53. The low values of energy product are due to the formation of the soft magnetic phase; Nd_2Fe_{17}. Region 2 is less important here because the 2-17 phase is found to occur from low wheel speeds up to 12.2 m/s. The formation of the 2-17 phase rather than grain growth controls the level of hard magnetic properties.

Carbon Addition

C addition is found to have the opposite effect of Ti on the formation of properitectic iron. In the X=2 and X=6 C alloys, region 1 is extended up from 17.5 m/s in the base alloy to 20 m/s and 25 m/s respectively. On the CCT diagram, this can be easily visualized by essentially moving the start of the properitectic iron region (region 1) to the left to shorter times. The X-ray diffraction scan of Figure 54 shows the presence of crystalline iron in an otherwise amorphous sample in the X=6 C alloy melt-spun at 20 m/s. That crystalline iron can exist in an amorphous matrix can be easily explained through visualization of the CCT diagram with region 1 modified.

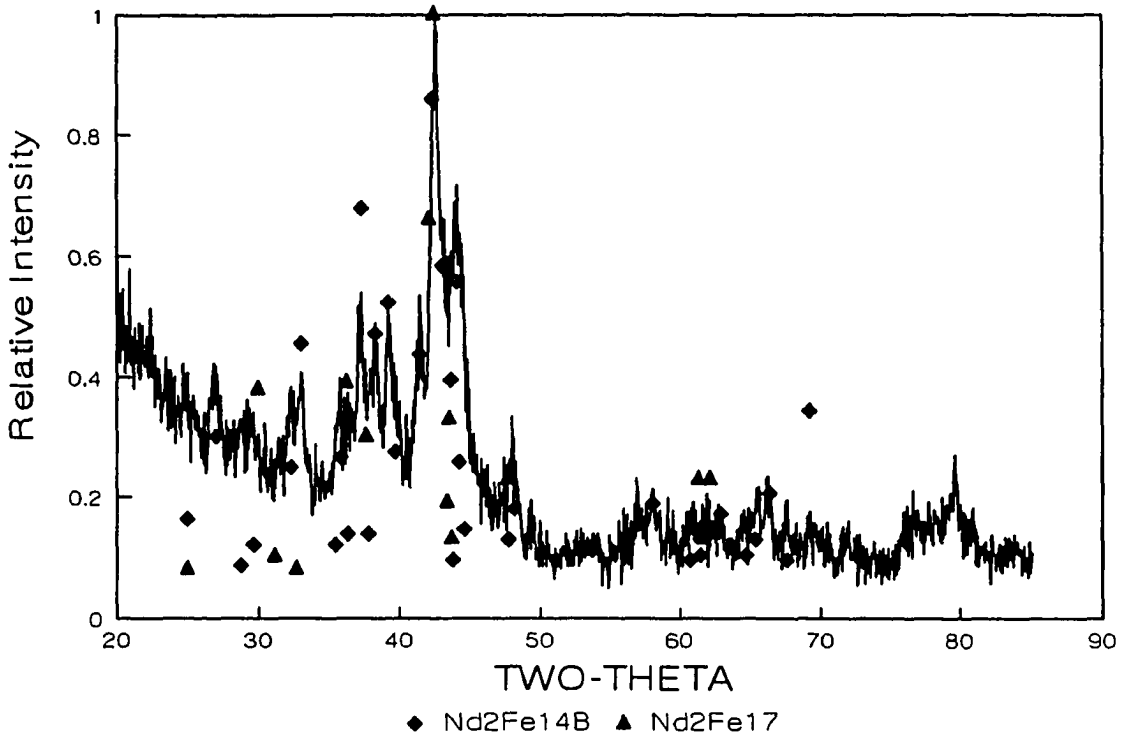

Figure 53 XRD of X=6 Ti alloy which has been melt-spun at 10 m/s.

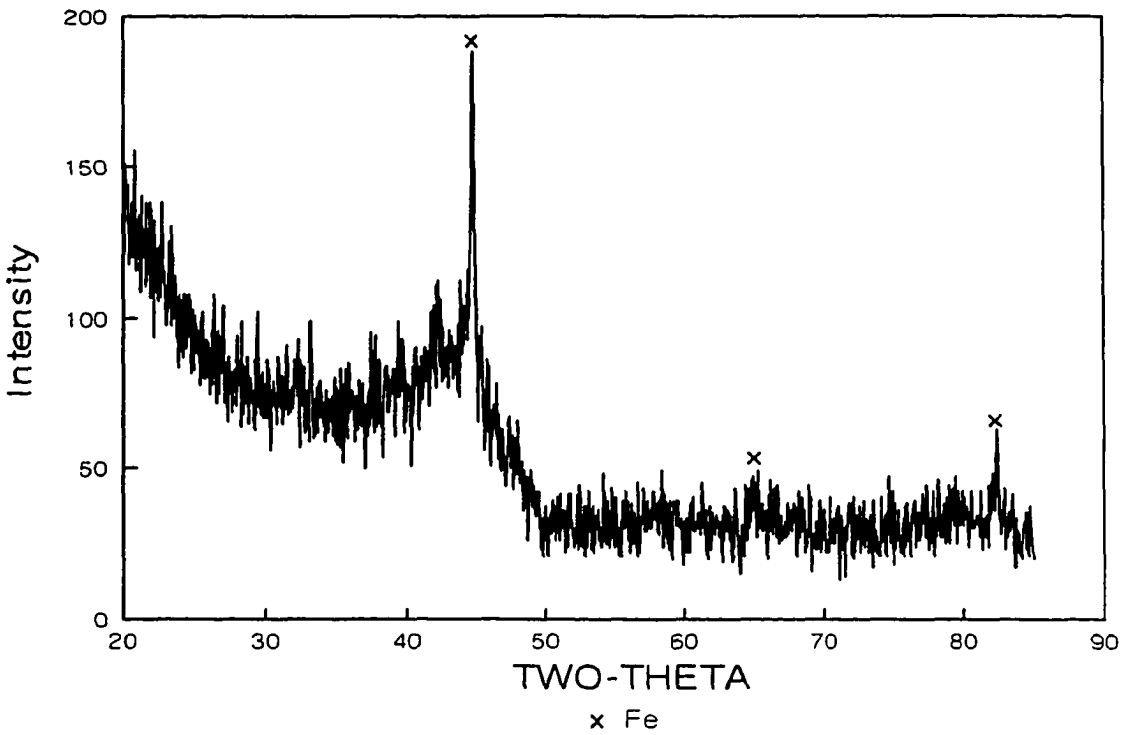

Figure 54 XRD of the X=6 C alloy which has been melt-spun at 20 m/s.

In the X=2 C alloy, region 3 begins at 29.4 m/s. This represents virtually no change in glass forming ability compared with the base alloy. Region 2 occurs over a medium range of cooling rates (20-29.4 m/s). In the X=6 C alloy, defining region 3 is somewhat arbitrary. Since free iron is found up to 25 m/s, separating the loss of coercivity due to magnetically soft glass or free iron is difficult. However, from the X-ray scans, increased glass forming ability is apparent. This enhanced glass forming ability in the X=6 C alloy can be explained. The model CCT diagram is not valid in this case due to the large compositional differences occurring upon solidification. Even at high solidification rates (wheel speeds), a significant amount of free iron is formed. After iron comes out of solution, the remaining liquid is rare earth rich. This moves the composition of the Nd-Fe-B-C system nearer to the ternary eutectic composition. Lowering the liquidus temperature reduces the undercooling necessary to avoid the solid state reactions and enhanced glass forming ability results. This beneficial effect is offset by the reduction in hard magnetic properties caused by iron formation. Also, this data indicates that free iron does not act as heterogeneous nucleation sites for the 2-14-1 phase since iron is found in coexistence with the amorphous matrix.

Titanium and Carbon Addition

When Ti and C are added to the 2-14-1 phase, properitectic iron formation is suppressed and region 1 is shifted down to very low wheel speeds. From DTA measurements, it is found that as Ti and C are added to the stoichiometric 2-14-1 composition, the liquidus is decreased (See PART III). This essentially suppresses the properitectic iron formation since less undercooling is needed to avoid the peritectic reaction. This change of cooling rate dependance can be visualized on the CCT diagram

because the properitectic iron region would be reduced and moved to the right to longer times.

In the TiC alloys enhanced glass forming ability is observed consistent with the Ti addition. In the X=2 TiC and X=6 TiC alloys, region 3 extends down from 29.8 m/s in the base alloy to 19.9 m/s and 12.3 m/s respectively. This again can be visualized on the model CCT diagram through moving the nose of the glass to crystalline transition region to the right to longer times. In the X=6 TiC alloy, the glass to crystalline transition is very rapid due to the increase in the crystallization temperature of the 2-14-1 phase caused principally from the Ti dissolution. The increased crystallization temperature causes an enhancement in nucleation rate and allows for rapid crystallization once the activation energy barrier is exceeded. This is shown by the X-ray diffraction scans at 11.5 and 12.5 m/s (Figure 55).

In the X=2 TiC alloy, region 2 represents a very wide range of wheel speeds (5 to approximately 19.9 m/s). It was hoped by the addition of Ti and C in this alloy, the peaked relationship of BHmax versus wheel speed, common in region 2, would be flattened out due to the formation of TiC precipitates pinning grain boundaries and preventing grain growth. However, it has been shown in PART III that the 2-14-1 phase can dissolve between X=2 to 3 TiC (4 to 6 at% Ti+C) in supersaturated solid solution. Due to the rapid solidification conditions little or no TiC is expected to exist in this as-spun alloy. None is found in the X-ray diffraction scans. After an appropriate heat treatment, the dissolved Ti can be pulled out of solution as TiC precipitates. These precipitates can then be used to prevent any subsequent grain growth.

In the X=6 TiC alloy, region 2 represents a narrow region from 7.5 to 12.3 m/s. Even at high wheel speeds, TiC shows up in the X-ray diffraction scans. Since the solubility limit of Ti has been exceeded in the liquid phase, primary

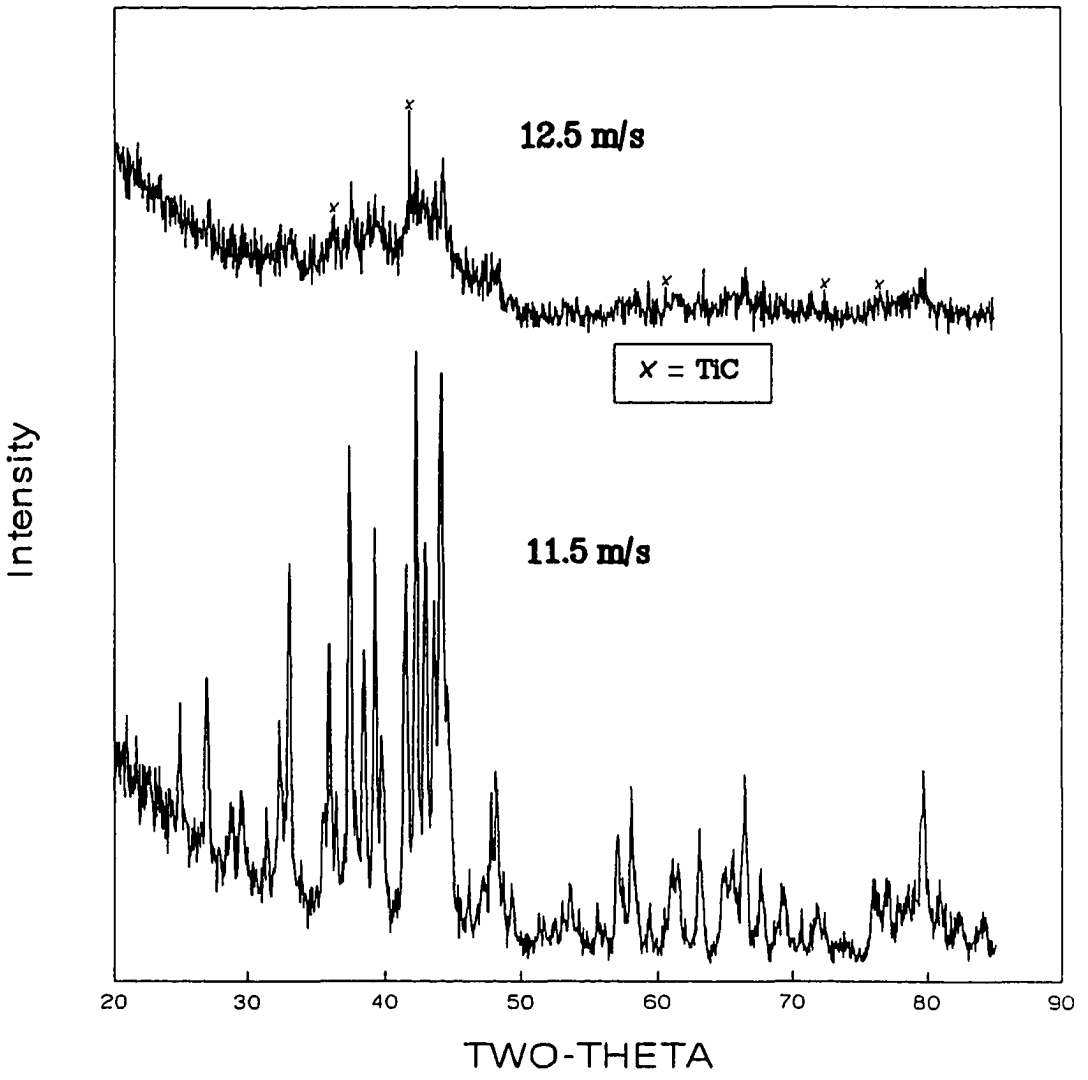

Figure 55 XRD scans of the X=6 TiC alloy which has been melt-spun at 11.5 and 12.5 m/s.

TiC precipitates formed in the melt before solidification began. Since, the primary carbides already exist at the melt-spinning temperature (1375°C), so there is no time dependence on the CCT diagram for their formation. Also, since the excess Ti and C form TiC and the solidification sequence is not changed, the model CCT diagram is still conceptually valid.

Importance of Microstructural Control

Controlling the start of the peritectic iron region could be very significant in alloy development. It has been shown that the start of properitectic iron formation can be varied through alloy modification from melt-spinning tangential velocities of 5 to 25 m/s. In conventional 2-14-1 magnets, the formation of free iron would be suppressed because properitectic iron formation usually results in a diminished level of coercivity. In the newly developing high remanence isotropic magnets[19,20], the size and distribution of the iron that precipitates out at a particular cooling rate will directly determine the level of hard magnetic properties.

Controlling the start of the liquid to crystalline 2-14-1 region on the CCT diagram is also very significant. It has been shown that the glass forming ability can be increased from forming a substantially amorphous structure at 29.8 m/s down to 12.3 m/s. This represents a change of more than one order of magnitude in cooling rate. Glass forming ability is a very important property of any commercial alloys produced by RSP. In many processing schemes, the formation of an overquenched structure is the first step in production[83,84,86,114,115]. The formation of a glass precursor offers many advantages. Forming an amorphous or overquenched structure is easier and represents a wider processing zone than in trying to produce directly the optimum grain structure. In thermomechanical processing starting with overquenched material allows more time for

compaction to full density before the grains have grown above the optimum single domain grain size. The ability to alter an alloys glass forming ability is a significant new type of metallurgical control. Processes that have only a small variability in high cooling rates, such as gas atomization, may now be fully exploited through the development of new alloys with enhanced glass forming ability.

Controlling or reduction in the optimum cooling rate could also be important in permanent magnet processing. It has been shown that the optimum cooling rate can be varied from 21.25 m/s to 10 m/s. In the melt-spinning route, often the alloys are overquenched but are still processed near the optimum cooling rate. By reducing the optimum cooling rate, the quality of the melt-spun ribbon is enhanced. Ribbons formed at a lower quench rates are usually longer and more uniform and there is generally less shot formation. In addition, the control of the optimum cooling rate may allow new and different RSP techniques to be utilized since the alloy's optimum cooling rate could be tailored to the average cooling rate of a particular processing technique.

SUMMARY

For the analysis in this paper, a model CCT diagram has been developed for solidification of stoichiometric $Nd_2Fe_{14}B$ alloys. The CCT diagram shows the development of the microstructure during solidification through a wide range of cooling rates from rapid solidification to equilibrium cooling. The usefulness of using CCT diagrams to represent solidification during continuous cooling is shown through the compilation of regional data from the energy product versus wheel speed plots. The changes in cooling rate dependance of phase formation brought about from the alloying additions are easily visualized through the use of the CCT diagram.

Small additions (X=2) of Ti, C or TiC to the base alloy cause enhanced optimum energy products. Large additions (X=6) of Ti or C alone result in low values of optimum energy product due to the formation of additional soft magnetic phases. Ti addition above the liquid solubility limit forms primary TiB_2 precipitates which deplete the system of boron and causes the formation of the 2-17 phase. C forms neodymium carbide which depletes the system of neodymium and causes the formation of free iron. Even with large additions of TiC (X=6), high values of optimum energy product are obtained. The excess Ti and C above the liquid solubility limit form primary TiC precipitates. These primary TiC precipitates form in the liquid and don't influence the subsequent solidification sequence. They also are found to have no detrimental affect on the magnetic properties.

The cooling rate dependance of properitectic iron formation, glass forming ability and the optimum cooling rate can be altered by more than a factor of two in cooling rate through appropriate alloy modification. The results obtained from this study should be very useful in alloy development, alloy modification or any other situation where microstructural control is necessary.

PART V CHANGES IN GLASS FORMATION AND GLASS FORMING ABILITY OF $Nd_2Fe_{14}B$ BY THE ADDITION OF TIC

INTRODUCTION

In PART IV, intrinsic changes brought about from Ti and C additions to the 2-14-1 system were studied. When Ti and C are dissolved in the liquid and solid solutions, the intrinsic properties of these phases are changed. Significant intrinsic changes that were found included a large decrease in the properitectic iron formation range, a reduction in the optimum cooling rate, an increase in the optimum energy product, and an increase in the glass forming ability. In PART V, the effects of Ti and C on the glass formation and glass forming ability (GFA) will be studied in detail.

The GFA of any alloy produced by rapid solidification processing (RSP) is an important property. Although defining GFA is difficult, it is often related to a critical cooling rate which is the minimum cooling rate at which crystal formation can be still observed.[114] The formation of an amorphous or partly crystalline structure is the first step in many processing schemes.[83,84,86,115,116] Forming an overquenched structure gives a much larger processing zone than trying to produce the optimum microstructure directly upon solidification. In addition, RSP processes such as gas atomization that have lower maximum cooling rates than melt-spinning, can be more fully exploited through tailoring the alloys GFA to the available processing technique.

As a liquid is cooled, two events can occur. Either crystallization can begin at the melting temperature or the liquid will become supercooled. If crystallization is suppressed, further decreases in temperature cause an increase in the viscosity of the liquid which then may form a glass. The glass temperature is reached when the viscosity of the melt equals 10^{12} Nsm^{-2}.[117] A metallic glass can be described in simple terms as a supercooled liquid which has not had enough time for crystallization. Good glass forming ability requires poor crystallization of the supercooled melt. To obtain a glass, crystallization has to be subdued down to the glass temperature. Thus, the temperature difference between the

melting temperature (T_m) and the glass temperature (T_g) is important. It should be noted that the glass temperature is not fixed and is dependant on the cooling rate. As the cooling rate is increased, the glass transition temperature is raised.[118]

Studies have been done on enhancing the GFA of Fe-B and Fe-B-Tb alloys with La additions by Koon et al.[12,13,24,119,120] The authors explained the enhancement of GFA to the fact that La forms no intermetallic compounds with iron so that it has the effect of inhibiting intermetallic compound formation.[119] Another reason for the observed enhancement of glass forming ability from La additions has been proposed by Branagan and McCallum.[121] La substitution for Nd is found to destabilize the 2-14-1 phase resulting in a smaller crystallization enthalpy and a reduced driving force for crystallization. More undercooling is necessary to promote crystallization, thus, at a particular high cooling rate, more glass will be formed in the La containing alloy.

Other work on glass formation and enhancing glass forming ability in the Nd-Fe-B system has focused on changes in the ternary composition.[122-129] Generally, this work has showed that as the composition moves toward the ternary eutectic point, enhanced glass forming ability occurs. This is due to the reduction in melting point as the composition moves nearer the ternary eutectic temperature. Since T_m is lowered, the range (T_m-T_g) is reduced which requires less undercooling to prevent crystallization.

An alternative way to enhance GFA without changing the ternary composition would be quite attractive. An alloying addition is required that would allow enhanced GFA without sacrificing the properties of the base alloy. Alloys of transition metals and metalloids are best described by arrangements of stereochemically defined structural units than by the description of the liquid in terms of random packing of atoms. A prerequisite condition, although not sufficient, for glass formation is that the melt show a tendency towards compound formation. Then, in the liquid, there will be a non-random distribution

of the various atoms present which will lead to a chemical short range order.[116] The molecular like species are called associates.[116] The associates are often found to be simple structural units such as trigonal prisms and are fundamental to many transition metal-metalloid systems in both their crystalline and amorphous states.[130] The associates are generally assumed to be present above Tg and increase in number as the temperature is decreased. The existence of an association equilibrium in liquid alloys is a prerequisite for good GFA. In the $Nd_2Fe_{14}B$ (2-14-1) phase, boron atoms occupy trigonal prisms which pucker the hexagonal iron nets and stabilize the tetragonal crystal structure.[131]

The study of GFA is being done through TiC addition to stoichiometric 2-14-1. Since TiC has extremely low equilibrium solid solubility in the 2-14-1 phase, it can be added to a wide range of alloy compositions without affecting the base alloys metallurgical or magnetic properties (see PART III). When titanium and carbon are dissolved in the liquid or glass, the glass itself as well as the GFA are changed. The effects of TiC on the glass formation range, GFA, and the intrinsic properties of the glass will be discussed and from these results an explanation for the changes in GFA will be given.

EXPERIMENTAL APPROACH

To minimize sampling errors, for each DSC sample, the data is reported as an average of two independent measurements. At the highest wheel speed (45 m/s), some melt instability occurred due to system vibration. The DSC measurements (J/g) reported at 45 m/s are the highest value obtained at that wheel speed. Three alloys were studied with a composition; $(Nd_{2/17}Fe_{14/17}B_{1/17})_{100-2X} + Ti_XC_X$ with X=0, X=2, or X=6. The base alloy (X=0) was a stoichiometric $Nd_2Fe_{14}B$ was used for comparison. To study the amount of glass formed at a particular cooling rate, melt-spinning can be utilized. By varying the wheel tangential velocity, the cooling rate is changed. As a first approximation, the mean cooling rate near the vicinity of the solidification point is found to vary linearly with wheel tangential velocity.[135] Since the thermal conductivity will change insignificantly at the levels of TiC addition used in this study, the GFA of samples melt-spun under identical melt-spinning conditions can be compared directly at a constant cooling rate. In this section, the enhancement of GFA is being studied through TiC addition to stoichiometric (2-14-1). Since TiC has extremely low equilibrium solid solubility in the 2-14-1 phase, it can be added to a wide range of alloy compositions without reducing the resulting magnetic properties (see PART III). When it is dissolved in the liquid or glass, it can affect the GFA. The effects of TiC on the glass formation range, GFA, and the intrinsic properties of the glass will be discussed. In addition, an explanation for the enhancement in GFA will be given.

RESULTS

Glass Forming Ability

To study the amount of glass formed at a particular cooling rate, melt-spinning can be utilized. By varying the wheel tangential velocity, the cooling rate is changed. As a first approximation, the mean cooling rate near the vicinity of the solidification point is found to vary linearly with wheel tangential velocity.[133] Since the thermal conductivity will change insignificantly at the levels of TiC addition used in this study, the GFA of samples melt-spun under identical melt-spinning conditions can be compared directly.

Classification

The energy product versus wheel speed plots for the stoichiometric 2-14-1 (X=0), X=2 TiC, and X=6 TiC alloys can be seen in Figure 50. As shown in PART IV, TiC additions reduce the optimum wheel speed (cooling rate) and increase the optimum energy product. At high wheel speeds, glass formation occurs which is verified by XRD. XRD scans of the as-spun ribbons can be used to qualitatively estimate the amount of glass formation. In Figure 56, XRD are shown for the melt-spun X=0, 2, and 6 TiC alloys at a constant cooling rate corresponding to a wheel speed of 15 m/s. The diagrams show the changes in the structure of the as-spun ribbons from crystalline to partly crystalline to amorphous caused by TiC addition.

Another method of estimating the amount of glass formation is achieved by using the measured magnetic properties at the high wheel speeds. The glass is magnetically soft since it has no magnetocrystalline anisotropy. When it is present in a partially crystalline structure, it is the site for the nucleation of reverse domains which leads to low levels of

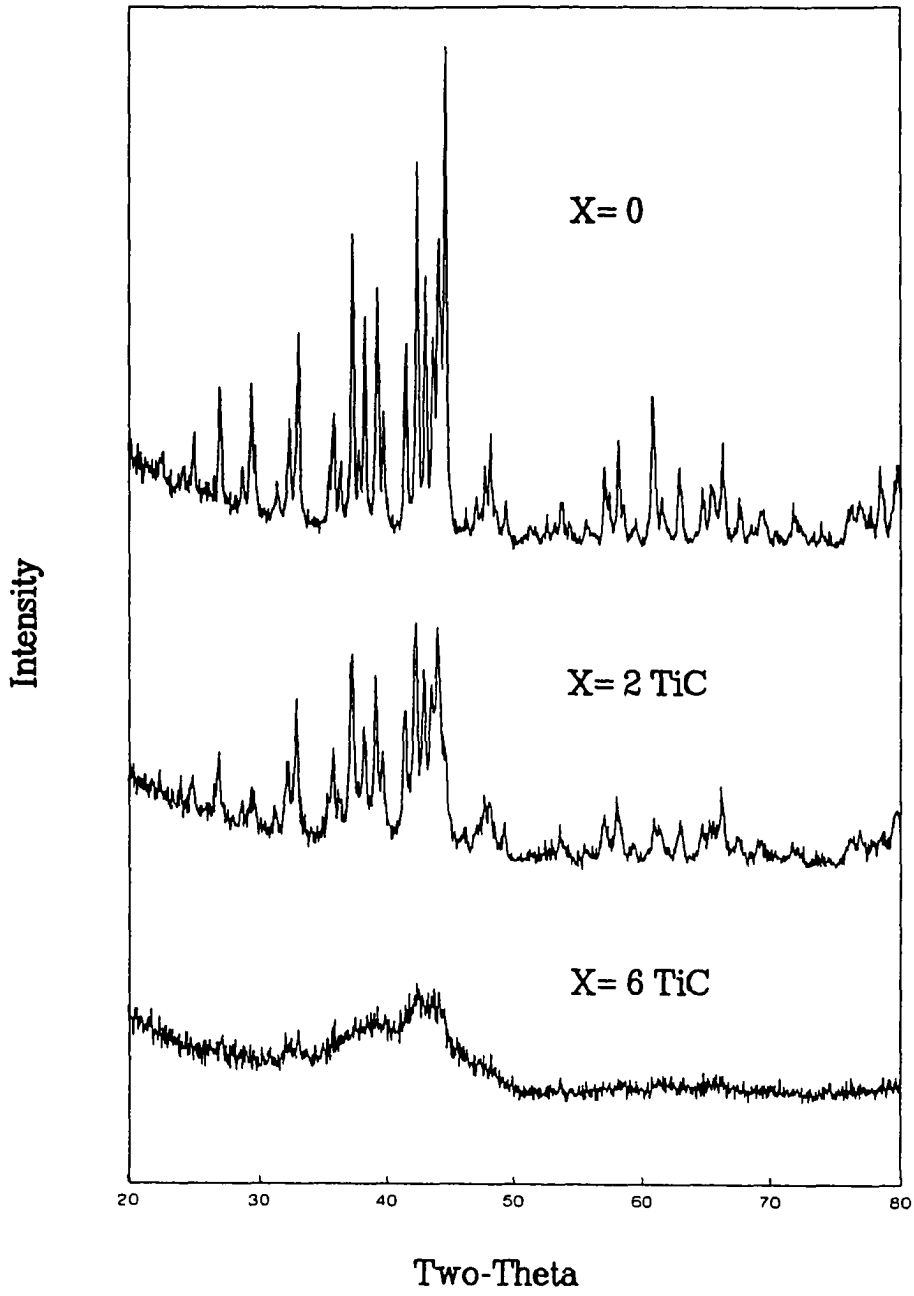

Figure 56 XRD scans of the X=0, 2 and 6 TiC alloys which have been melt-spun at 15 m/s.

coercivity. A significant glass range for each alloy can be defined as one giving a maximum level of coercivity at the high wheel speeds equal to 1000 Oe (see Part IV). The glass range for each alloy interpolated at a coercivity of 1000 Oe can be seen in Table 19.

Characterization

The amount of glass formation as a function of cooling rate can be measured in a direct fashion through measuring the exothermic energy released upon crystallization through DSC. In Figure 57, a plot of crystallization energy versus wheel speed is shown for the X=0, 2, and 6 TiC alloys. The amount of glass formed as well as the maximum exothermic energy released from the glass to crystalline transition is changed by the addition of TiC.

Table 19 Glass Range

Alloy	Glass Range (m/s)
X=0 TiC	29.8
X=2 TiC	19.9
X=6 TiC	12.3

Intrinsic Glass Properties

Since the enhancement in the GFA has been documented, the next step is to study changes in the intrinsic properties of the glass. Since the glass is a supercooled liquid, the intrinsic changes must be due to structural changes in the local short range order. Possible alterations in local order would include a change in the packing of the atoms through a

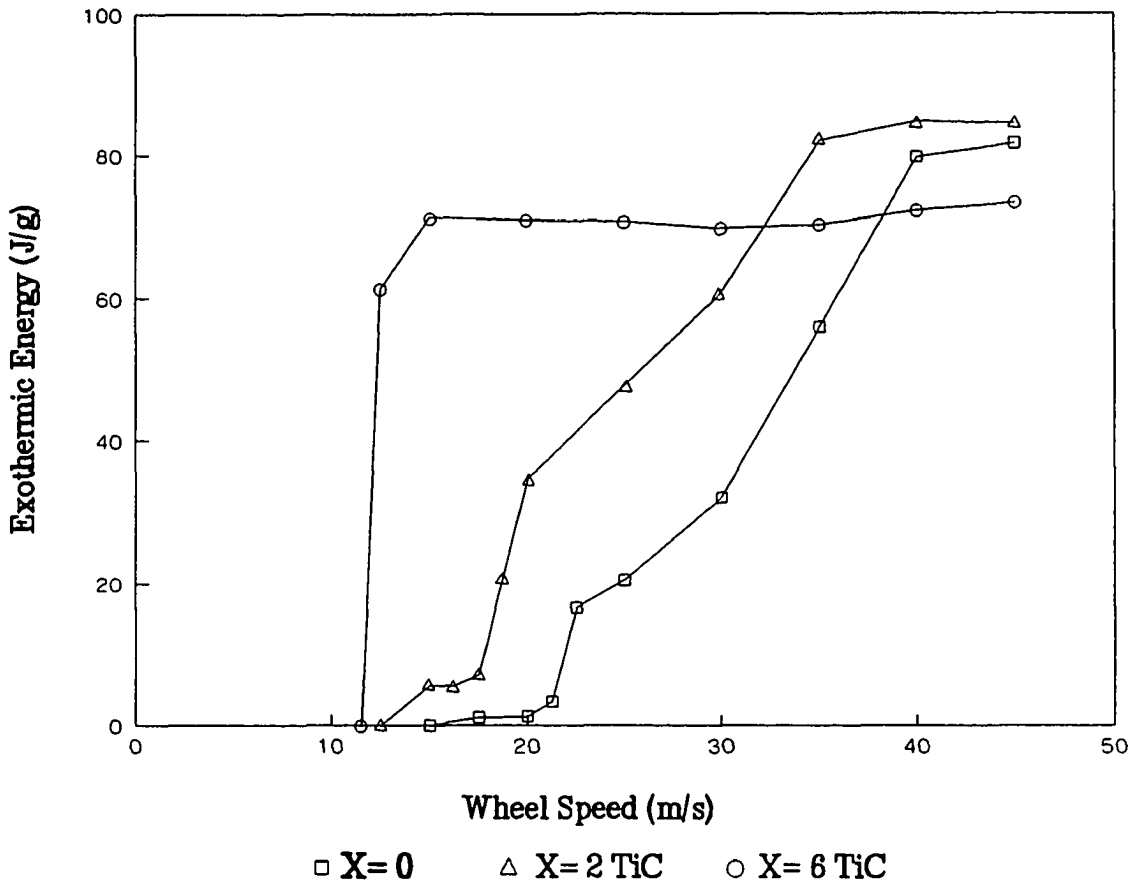

Figure 57 Exothermic Energy versus wheel speed for the X=0, X=2, and X=6 TiC alloys.

change in coordination number, a change in the packing efficiency or a change in the fundamental unit of packing (molecular associate). Through using experimental techniques such as Mössbauer, nuclear magnetic resonance (NMR), or extended X-ray absorption fine structure (EXAFS), the molecular associates could be studied in a direct fashion. In this paper, changes in the intrinsic properties of the glass will be used to infer information on local structural changes in the glass.

Stability

On the DSC plots, the T_g will appear as an endothermic change in slope of the baseline.[114] The glass transition temperatures were not found on the DSC plots of the melt-spun samples which indicates that crystallization occurred before T_g was reached, which is common in metallic glass systems.[118] The onsets of the DTA peaks can be seen in Table 20 for each alloy which has been melt-spun at 45 m/s. Figure 58 shows changes in intrinsic glass properties versus composition and it can be seen that the crystallization temperature is raised with TiC addition. Note that in using Figure 58, the liquid solubility limit is around $X \approx 3$ which limits the amount of TiC dissolution into the glass (see PART III). The X=6 TiC alloy is over the liquid solubility limit so the amount dissolved in the glass is far below the nominal composition.

Table 20 DTA Peaks

Alloy (°C) >>	Peak 1 (exo)	Peak 2 (endo)	Peak 3 (endo)
X=0 TiC	559	1099	1175
X=2 TiC	602	1156	1170
X=6 TiC	626		1162

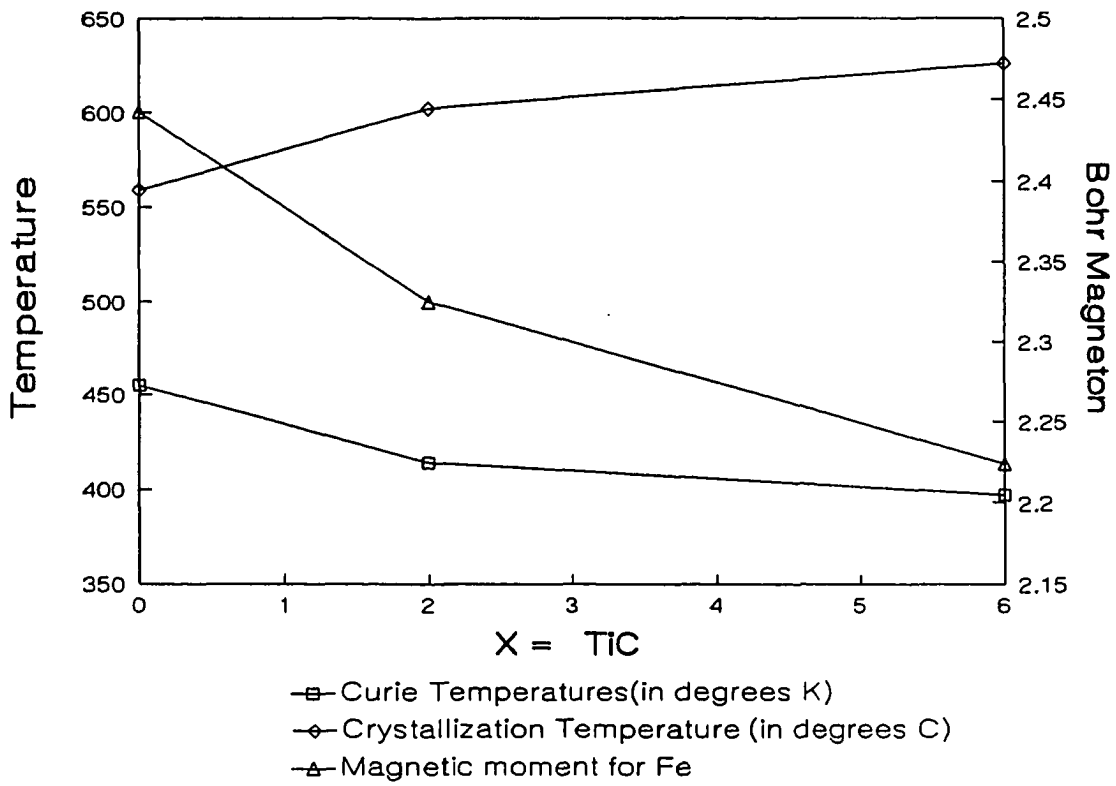

Figure 58 Intrinsic glass changes versus composition.

Transformation Rate

In Figure 59, DSC plots of the X=0, 2, and 6 TiC alloys melt-spun at 45 m/s are shown. The transformation rate can be defined as the ratio between the height of the crystallization peak divided by the complete area.[134,135] The transformation rates for each alloy are shown in Table 21.

Table 21 Transformation Rates

Alloy	Transformation Rate (s^{-1})
X=0 TiC	$4.87 * 10^{-3}$
X=2 TiC	$5.82 * 10^{-3}$
X=6 TiC	$11.33 * 10^{-3}$

Saturation Magnetization

In Figure 60, the saturation magnetization is plotted versus temperature for the X=0, 2, and 6 TiC alloys. The saturation magnetization is reduced with the addition of TiC to the stoichiometric alloy. This reduction of saturation magnetization from the stoichiometric alloy is approximately 2500 Gauss in the X=6 TiC alloy. This is a much greater reduction than the 1100 Gauss which would be expected from a simple mass dilution effect from the introduction of a nonmagnetic phase.

Curie Temperature

The changes in T_C versus composition are shown in Figure 58. As TiC is added, the T_C is decreased with a 58 K reduction in the X=6 TiC alloy.

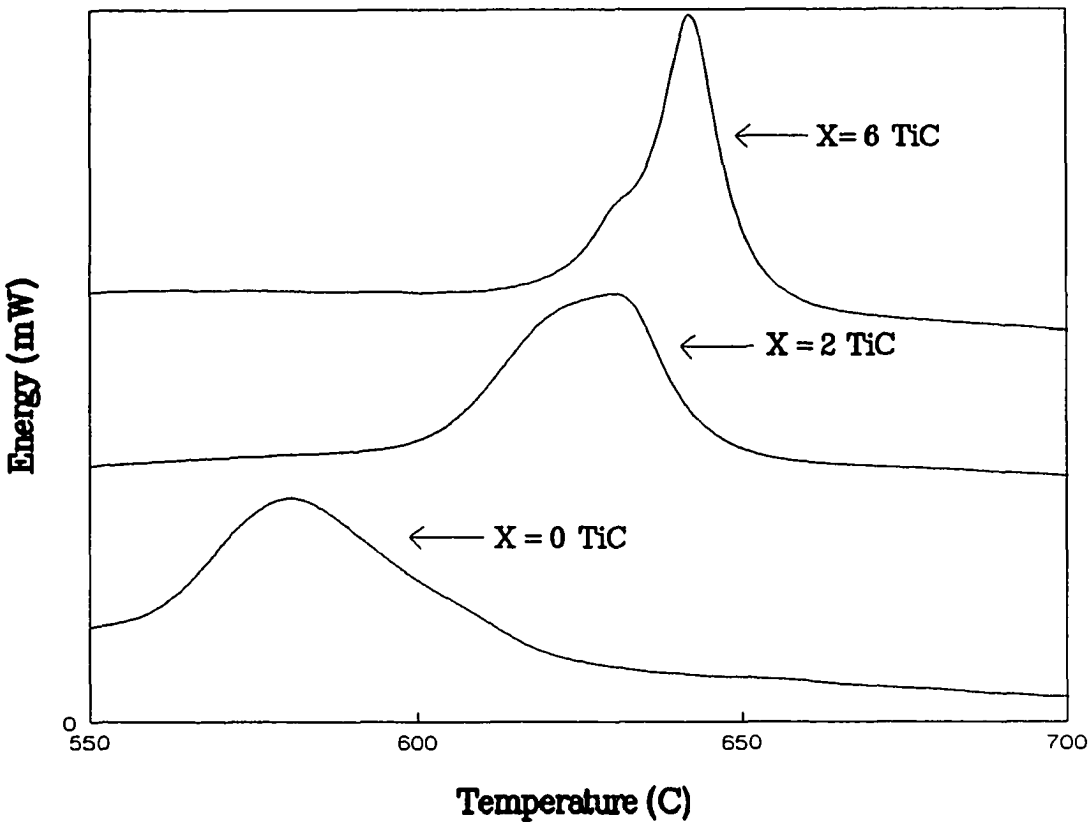

Figure 59 DSC plots of the X=0, X=2, and X=6 TiC alloys which have been melt-spun at 45 m/s.

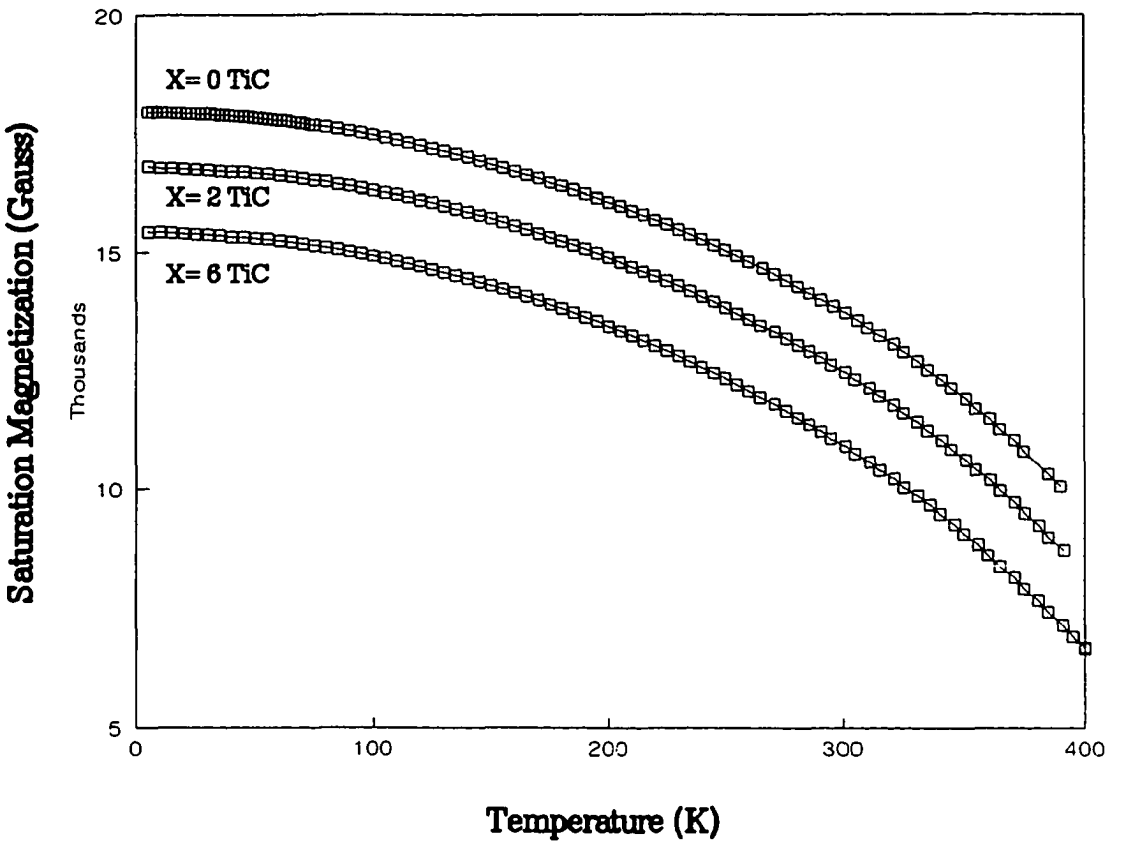

Figure 60 Glass saturation magnetization versus temperature for the X=0, X=2, and X=6 TiC alloys melt-spun at 45 m/s.

DISCUSSION

Glass Forming Ability

The XRD, magnetic, and DSC results from the RESULTS section all consistently show increases in GFA with TiC additions. The limit of the glass formation range represents wheel speeds (cooling rates) whose ribbons exhibit no crystallization energy (Figure 57). This limit is reduced from 15 m/s in the stoichiometric alloy down to 12.5 m/s and 11.5 m/s in the X=2 and X=6 TiC alloys respectively. Note that all values of wheel speed were not performed which could change the endpoints slightly but not this significant general trend.

Differences were found in the maximum value of the crystallization enthalpy. The maximum crystallization energy (at 45 m/s) of the X=0 and X=2 TiC alloys are similar with a slight increase in the X=2 TiC alloy. In the X=6 TiC alloy, the maximum exothermic energy is reduced. Part of this difference is that all of the mass of the alloy does not undergo crystallization since primary TiC precipitates already exist in the glass of the X=6 TiC alloy. The remaining reduction may be from primary TiC precipitates acting as heterogeneous nucleation sites. A thin shell of crystalline material may form around the primary precipitates during solidification which would further reduce the amount of material crystallizing in the DSC measurement. This small amount of crystallinity has not been verified however.

The samples melt-spun at 45 m/s are assumed to be entirely amorphous which was verified by TEM. In the X=6 TiC alloy melt-spun at 45 m/s, the absence of structure along with the selected area diffraction pattern which contained no spots and only a diffuse ring indicate a uniform glass is formed (Figure 61). From PEELS, Ti and C were found

Figure 61 TEM micrograph of an X=6 TiC alloy which has been melt-spun at 45 m/s. Note the absence of structure indicating a uniform glass and the diffuse rings in the SAD.

to be homogenously distributed throughout the glass. The primary carbides were too large for study with the size scale of the TEM but were verified in the Auger microscope (See PART III).

By comparing the total amount of energy given off during crystallization at a particular wheel speed and comparing that to the amount given off at the maximum wheel speed, the fraction of glass can be found.[134-136] The fraction of glass for each alloy is shown in Table 22. Large changes in the amount of glass in each sample with cooling rate can be found. A primarily glass structure (> 95%) exists down to 40 m/s, 35 m/s, and 15 m/s in the X=0, 2, and 6 TiC alloys respectively. This represents a large increase in GFA through TiC addition.

Table 22 Percent glass in each wheel speed run

Wheel Speed (m/s)	Percent Glass		
	X=0	X=2 TiC	X=6 TiC
45	100	100	100
40	97.7	100.2	98.6
35	68.5	97.1	95.9
30	39.2	71.8	95.1
25	25	56.5	96.4
22.5	20.3		
21.25	4.1		
20	1.5	41.0	96.7
18.75		18.8	
17.5	1.3	8.3	
16.25		6.4	
15	0	6.6	97.3
12.5		0	83.6
11.5			0

Intrinsic Glass Properties

TiC additions when dissolved in the glass, change the intrinsic properties of the glass as shown in the RESULTS Section. TiC additions cause increases in the crystallization temperature of the 2-14-1 phase. Higher crystallization temperatures means the crystallization process should proceed with an enhanced nucleation rate due to the Arrenhius temperature dependance. Since TiC additions increase the transformation rate this indicates an enhanced nucleation rate is occurring. This is an important effect since this will allow less time for grain growth before impingement between neighboring grains which should lead to finer as-crystallized grain sizes. Enhancement in as-crystallized energy products have been documented in alloys modified with TiC and are attributed to this effect (See PART VI).

The increase in crystallization temperature can be explained with the free volume model. In the free volume model, space is broken up between the molecules or associates and the unoccupied volume which is called the free volume.[114,118] The distribution of associates in the glass leads to holes whose volumes are close to that of the unit involved in the diffusion process. In the glass structure, the free volume is frozen in. Molecular or atomic transport leading to crystallization can't occur until the thermal energy exceeds the activation energy for diffusion. Decreases in diffusivity or an analogous increase in viscosity from a reduction in free volume will lead to increases in crystallization temperature.

Thus, increases in the crystallization temperature can be explained by local structural changes in the short range order that cause a reduction in free volume. Additional information validating this hypothesis would be useful. It is widely accepted that the intrinsic magnetic properties of a glass depend primarily on the interactions

between nearest neighbors. Corb[137,138] has developed a quantitative model giving the dependance of magnetic moment on coordination number in transition metal-metalloid crystalline and glassy alloys. In this ligand approach, the metalloid atoms reduce the magnetic moment of neighboring transition metals through bond formation which reduces the number of free d-electrons and the corresponding magnetic moment. This general result should hold for more complicated systems since the glass structure is based on localized short range interactions.

From the saturation magnetization values at 5K the magnetic moments can be calculated. The magnetic moments per magnetic atoms (Ti, Fe, and Nd) are shown in Table 23. Bao-gen et al.[139] and Zhang et al.[140] have shown that the magnetic moment of the neodymium atom in a Nd-Fe-B glass is independent of composition. Bao-gen and Zhang reported magnetic moments of 1.02 μ_b (Bohr Magneton) and 1.05 μ_b for neodymium respectively. Using the 1.02 μ_b value for Nd and assuming that Ti makes no moment contribution, the magnetic moment for the Fe atoms can be calculated. A decrease in the magnetic moments of the Fe atoms is found with increasing amounts of TiC addition (Table 23). This reduction in magnetic moment is consistent with a change

Table 23 Magnetic Moments

Alloy X= TiC	Fe+Nd+Ti (μ_b)	Nd (μ_b)	Fe (μ_b)
0	2.264	1.02	2.442
2	2.115	1.02	2.325
6	1.934	1.02	2.224

in the short range order leading to a higher coordination number. Incidently, the magnetic moment for iron in the X=6 TiC alloy (2.224 μ_B) approaches the value for body centered cubic iron (2.219 μ_B).[141] Body centered cubic iron has a packing factor of 0.68, a coordination number of 8, and a lattice parameter equal to 2.866 Å.

The decrease in the T_c with TiC addition was shown in Figure 58. In transition metal - rare earth based systems, the 3d-3d, 3d-4f, and 4f-4f exchange interactions all contribute to the measured value of T_c. However, the 3d-3d interactions are by far the strongest and have the biggest effect on the T_c. The Fe-Fe interactions are strongly dependant on distance with a change from a ferromagnetic to antiferromagnetic coupling as the interatomic distance decreases below 2.44 Å.[102] The measured reduction in T_cs are a strong indication that the Fe-Fe separation distance is decreasing. Increases in coordination number would also contribute to the same trend.

From the changes in the intrinsic properties of the glass, it is clear that TiC dissolution is altering the short range order of the glass. The intrinsic changes in the glass are consistent with a reduction in free volume. This reduction seems to be occurring from smaller interatomic distances and higher coordination numbers leading to a more efficient packing of the fundamental molecular associates. These structural changes increase the stability of the glass since the more stable the glass, the higher the T_g.[142] The T_g was not measured but the crystallization and glass transition temperature generally show the same trends.[143] Raising T_g means that less undercooling (Tm-Tg) is required to prevent nucleation. Thus, at a particular high wheel speed (cooling rate), a higher percentage of glass will be formed in TiC added alloys.

SUMMARY

XRD, magnetic, and DSC measurements of the as-quenched alloys indicated enhanced GFA with the addition of TiC. The limits of glass formation and the amounts of glass formed at a particular high cooling rate were increased with TiC addition. Enhanced GFA was concurrent with intrinsic changes in the glass. The crystallization temperature of the 2-14-1 phase was increased by TiC dissolution. The increased crystallization temperature led to an increased transformation rate because of the Arrehnius temperature dependance of nucleation. The increase in crystallization temperature, reduction of magnetic moment, and increase in T_c are consistent with a reduction in free volume. Changes in the structural short range order by titanium and carbon dissolution increase the stability of the glass. This means that less undercooling (Tm-Tg) is required to prevent nucleation and a glass will form. Thus, in TiC added alloys, the GFA is increased.

PART VI THE EFFECTS OF Ti, C, AND TiC ON THE CRYSTALLIZATION OF AMORPHOUS $Nd_2Fe_{14}B$

INTRODUCTION

In PART V, the GFA of Ti and C dissolution in the liquid melt and solid glass was studied. Large increases in GFA were found with increasing amounts of Ti and C dissolution. Intrinsic changes in the glass properties were related to changes in the local short range order of the glass. Structural changes resulted in a reduction in the free volume of the glass. This caused a reduction in the diffusivity, increased the viscosity, and resulted in an increase in crystallization temperature with Ti and C addition. In PART VI, the effects of Ti, C, and Ti with C on the as-crystallized magnetic properties will be studied. The results can be used toward the production of high energy product permanent magnets.

Many investigators have successfully produced high energy product $Nd_2Fe_{14}B$ (2-14-1) type magnets by either quenching at an optimal wheel speed or slightly overquenching and then annealing to achieve an optimum grain size.[72,84,144,145] The annealing may be part of thermomechanical processing such as hot-pressing or die-upsetting resulting in consolidation and in some instances grain alignment which improves the remanence and the corresponding energy product.[83,86,146] In general, attempts to produce high energy product material from an amorphous precursor have not been successful. High energy products have been obtained by this route only by flash anneals of individual ribbon pieces.[147] Hsu et al[148] showed that this lack of success may be attributed to the fact that at the crystallization temperature, nucleation is the determining factor in the grain size obtained and in stochiometric 2-14-1, the nucleation of the hard phase is not uniform.

EXPERIMENTAL APPROACH

Six alloys along with a stoichiometric base alloy were chosen for study (See Table 24). Compositions are given in the form $(Nd_{2/17}Fe_{14/17}B_{1/17})_{100-X}$ + $Addition_X$. The compositions were chosen so that the effects of Ti or C alone could be differentiated from the effects of Ti with C addition. The base alloy is used for direct comparison. Each alloy was melt-spun at high speeds (30 m/s) to form a substantially amorphous structure. The amorphous structure was verified by X-ray diffraction. In this section, it is demonstrated that by selecting appropriate alloying additions, the energy product after crystallization can be raised. The enhancement of energy product of samples crystallized from the glass can be achieved by enhancement of the nucleation rate or inoculation. Since the temperature dependance of nucleation rate follows an Arrehius relationship, alloying additions were chosen which raised the crystallization temperature.

Table 24 Composition of Alloys Studied

Alloy	Composition	Ti Add X=	C Add X=
base	$Nd_{2/17}Fe_{14/17}B_{1/17}$		
X=2 Ti	$(Nd_{2/17}Fe_{14/17}B_{1/17})_{100-x} + Ti_x$	2	
X=6 Ti	$(Nd_{2/17}Fe_{14/17}B_{1/17})_{100-x} + Ti_x$	6	
X=2 C	$(Nd_{2/17}Fe_{14/17}B_{1/17})_{100-x} + C_x$		2
X=6 C	$(Nd_{2/17}Fe_{14/17}B_{1/17})_{100-x} + C_x$		6
X=2 TiC	$(Nd_{2/17}Fe_{14/17}B_{1/17})_{100-2x} + Ti_xC_x$	2	2
X=6 TiC	$(Nd_{2/17}Fe_{14/17}B_{1/17})_{100-2x} + Ti_xC_x$	6	6

RESULTS AND DISCUSSION

Crystallization Temperature

In Figure 62, the onset of the crystallization temperatures for the 2-14-1 phase from DTA analysis for the X=2 and X=6 alloys of Ti, C and TiC are presented along with the curve for the base alloy. As shown, in the X=2 C alloy, the crystallization temperature of the 2-14-1 is raised only slightly while in the X=2 Ti alloy there is a large increase. The behavior in the X=2 TiC alloy is almost identical to that of the Ti alloy. While the crystallization temperature of the X=6 C alloy remains largely unchanged, in the X=6 Ti and the X=6 TiC alloys, the crystallization temperature continues to increase. In the X=6 Ti and the X=6 TiC alloys, the liquid solubilities have been exceeded and the amounts of Ti or Ti with C dissolved in the glass are considerably less than the nominal percentage (see PART II). The largest increase is found in the X=6 Ti alloy, which is probably due to its higher liquid solubility (see PART II).

As-Crystallized Magnetic Properties

The results of magnetic measurements on these samples are presented in Table 25. The as-spun ribbons of each alloy were crystallized by heat-treating at 650°C for one hour. This temperature was chosen because it is high enough to crystallize the 2-14-1 phase but low enough to prevent excessive grain growth. Grain growth after complete crystallization is driven by the reduction in surface energy from the reduction in grain boundary surface area per unit volume. This type of grain growth is found to occur generally at temperatures above 800°C (see PART I).

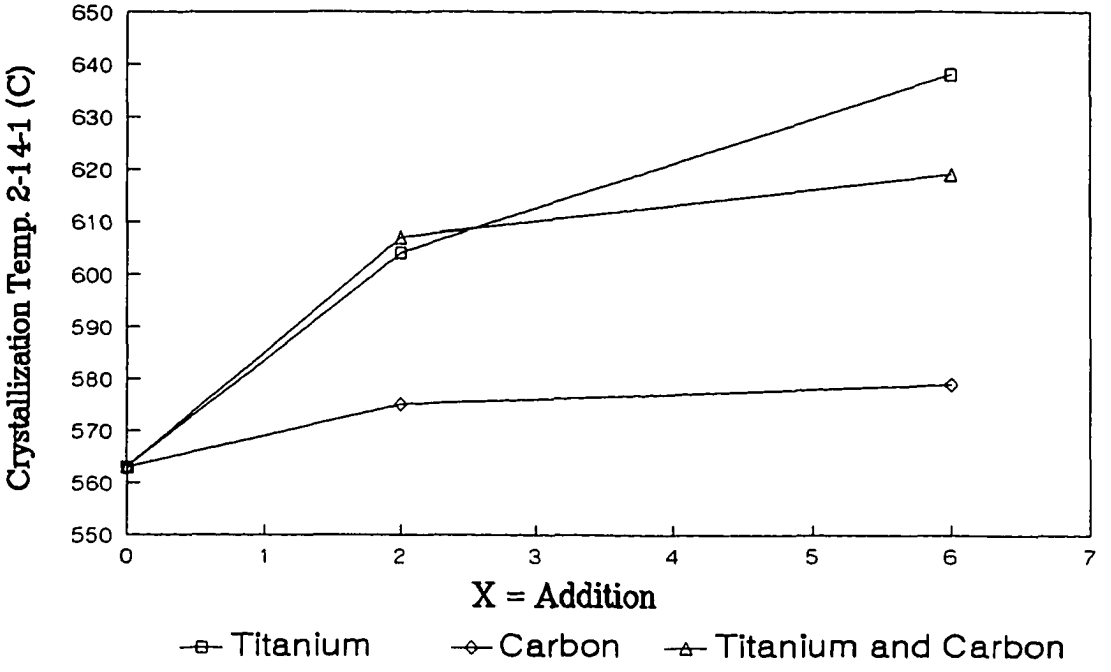

Figure 62 Variation of the crystallization temperature of the 2-14-1 phase with titanium, carbon, and titanium with carbon additions.

Table 25 Magnetic Properties

Addition X =	Msat (G)	Remanence (G)	Coercivity (Oe)	BHmax (MGOe)
0	15,310	8440	6420	7.1
2 C	14,680	9240	8770	16.4
6 C	14,890	8180	3020	6.9
2 Ti	14,850	9310	8740	17.4
6 Ti	12,790	7430	10,840	7.0
2 TiC	14,720	9290	9780	17.1
6 TiC	14,130	8540	8760	14.1

In Figure 63, a bar graph shows the as-crystallized energy products versus alloying addition. It is important to note that the crystallization temperature of the particular alloy is important and not necessarily the furnace temperature. The samples are placed in a hot furnace and almost certainly crystallization occurs as each sample is heated up to its particular crystallization temperature.

Base Alloy

The base alloy has a crystallized energy product of 7.1 MGOe. This low value of energy product is due primarily to a low value of as-crystallized coercivity. In the base alloy, the crystallization temperature is only 563°C. During crystallization, grains nucleate and then grow until impingement occurs between neighboring grains. By this process occurring at low temperature, some grains have grown more than others and the as-crystallized grain size is nonuniform. In addition, this effect can be compounded by problems with nucleation.

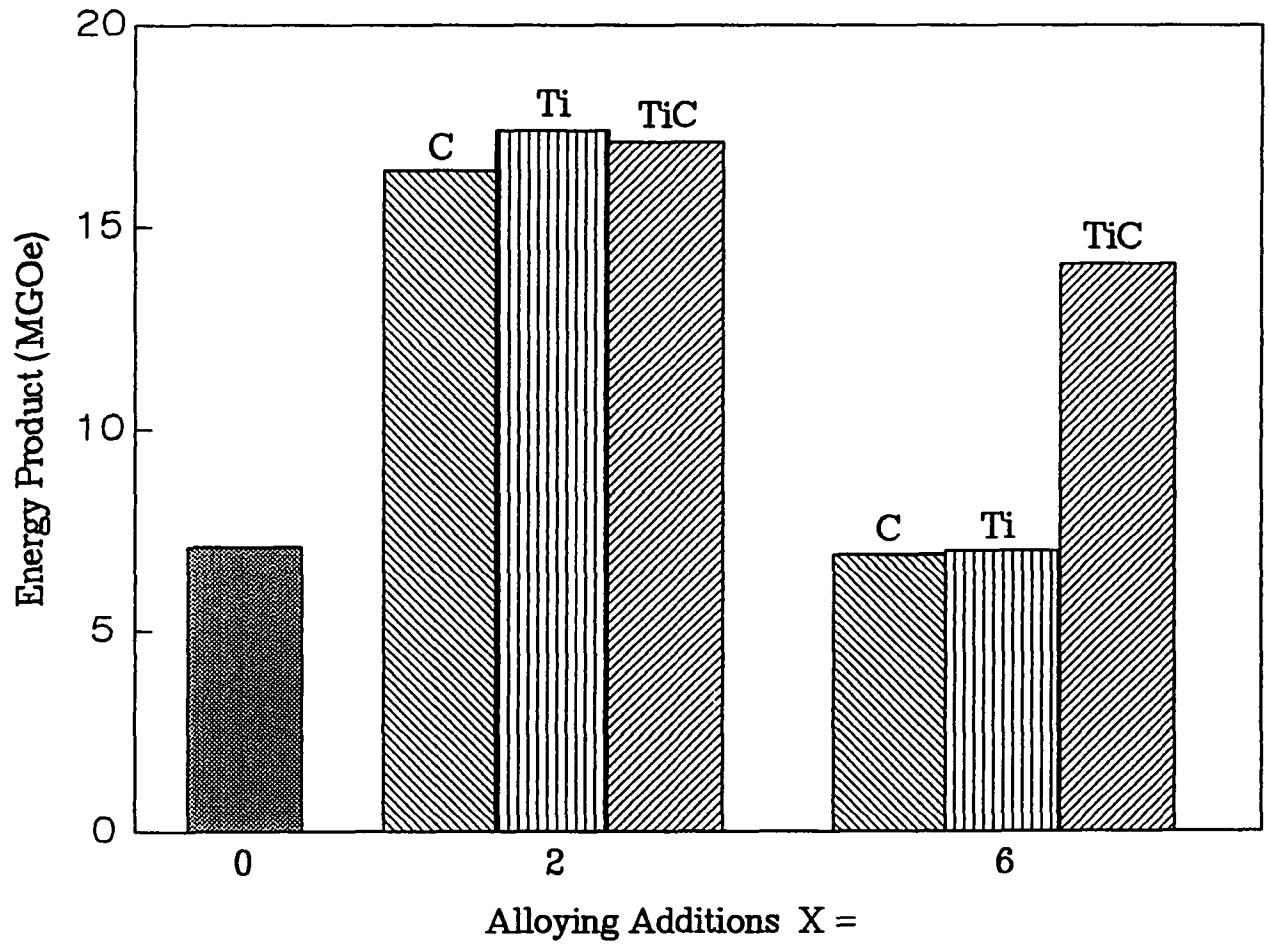

Figure 63 Energy product versus alloying additions for samples crystallized from the glass at 650°C for one hour.

Titanium Addition

In the X=2 Ti alloy, a maximum energy product of 17.4 MGOe is obtained. This much improved energy product is due to the enhancement of coercivity from the higher crystallization temperature resulting from Ti addition. In the X=6 Ti alloy, the crystallization energy product is low even though the crystallization temperature is quite high (75°C above the base alloy). From Table 25, it can be seen that the coercivity is high but the saturation and remanence are low. The high coercivity indicates that the grain size of the 2-14-1 phase is near optimum which is consistent with the high crystallization temperature. The low saturation magnetization value is due to the alloy chemistry of titanium addition. It appears that the solubility of Ti in the melt is limited by the solubility of TiB_2. When the solubility limit is exceeded, the precipitation of TiB_2 removes B from the melt. The formation of the 2-14-1 phase is then limited by the amount of available B and results in the formation of the Nd_2Fe_{17} (2-17) phase. This causes a corresponding reduction in saturation magnetization because the 2-17 phase has a lower value of magnetization since its Curie temperature is 330 K. While the detection of TiB_2 by X-ray diffraction is difficult, both 2-14-1 and 2-17 phases are found in the as-crystallized ribbon (Figure 64). The formation of titanium borides is consistent with the alloy chemistry of Nd-Fe-B-Ti ingots (see PART II).

Carbon Addition

While the X=2 C alloy exhibits only minor effects on the crystallization temperature, the maximum energy product is increased to 16.4 MGOe. An explanation for this increase is that a distribution of neodymium carbides formed which promoted nucleation. Neodymium carbides have been identified in Nd-Fe-B type magnets that contained carbon additions.[149] The carbides may be sufficiently

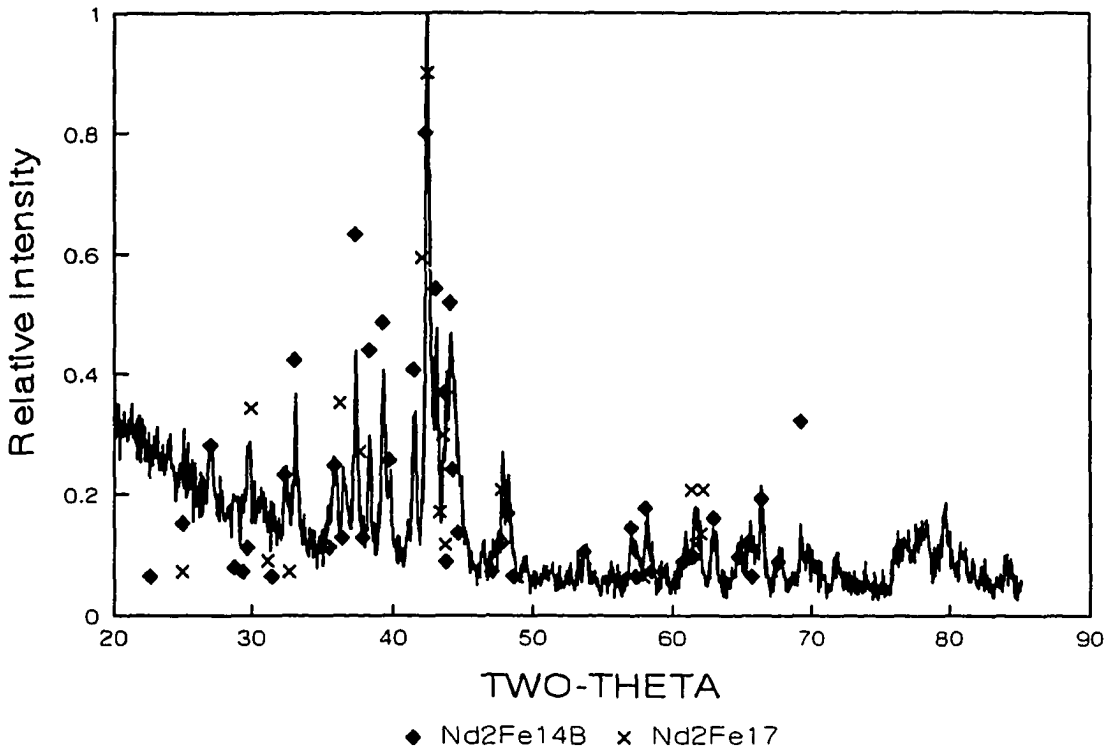

Figure 64 XRD of the X=6 Ti alloy which has been heat treated at 650°C for one hour.

well distributed to serve as sites for heterogeneous nucleation resulting in a near optimum microstructure on crystallization. Clearly TEM measurements are required to validate this hypothesis. For the X=6 C alloy there is a sharp decrease in energy product due to a low value of coercivity. X-ray diffraction scans show the presence of free iron in this alloy (Figure 65). This is consistent with PART IV and is caused by the high stability of the NdC_2 phase which forms removing Nd from the melt and results in the formation of α-Fe. The $Nd_1Fe_4B_4$ phase should also form but this is much more difficult to detect. Clearly, for the large C addition, the free iron is in sufficiently large particles to cause a reduction in coercivity due to the nucleation of reverse domains.

Titanium and Carbon Addition

As with all of the low level additions, the X=2 TiC alloy shows a large enhancement of the energy product ($\approx$10 MGOe) on crystallization relative to the base alloy. This is consistent with the high crystallization temperature of 607°C increasing the nucleation rate and giving a more uniform grain size. Unlike the other alloys, the X=6 TiC alloy also nucleates with a high energy product. Since TiC is the most chemically stable compound in the system, additions of TiC do not result in the formation of deleterious phases. Titanium and carbon in excess of the liquid solubility limit, forms titanium carbide precipitates in the liquid. The crystallization temperature of the X=6 TiC alloy is very close (12°C) to that of the X=2 TiC alloy which is consistent with the liquid solubility (see PART III). TEM measurements of the grain size for the X=6 TiC alloy crystallized from the glass verify the hypothesis. After a 750°C for one hour anneal, the X=6 TiC alloy had a finer and more uniform grain size when compared to the base alloy (See PART I). It is important to note that the energy product after crystallization of the X=6 TiC alloy is lower than in the X=2 TiC alloy. This decrease

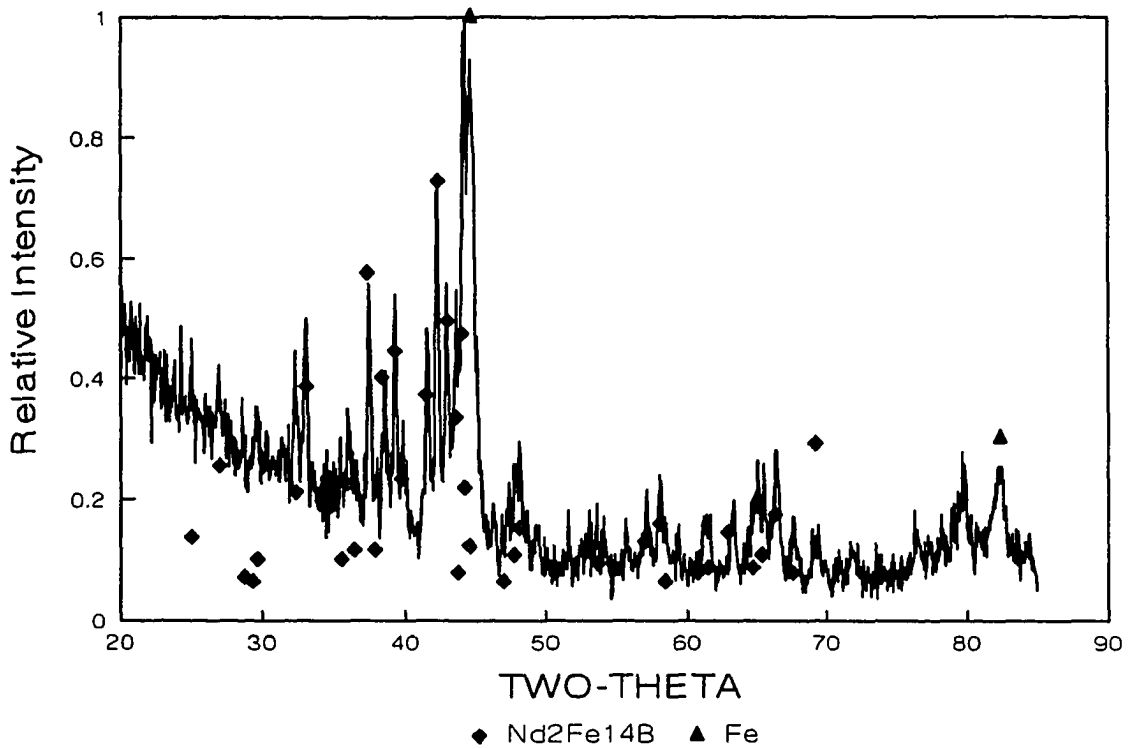

Figure 65 XRD of the X=6 C alloy which has been heat treated at 650°C for one hour.

is partly from the reduction in the amount of hard magnetic phase from the large (12 at% Ti+C) TiC addition. Since this only accounts for part of the reduction, the TiC primary precipitates may be acting as nucleation sites for reverse domains.

SUMMARY

The energy products of materials crystallized from a substantially amorphous precursor can be more than double that of the base alloy when appropriate alloying additions are used. This increase is attributed to a more uniform microstructure due to enhanced nucleation of the hard magnetic phase. Two factors may contribute to this nucleation. First additions of Ti and TiC raise the crystallization temperature of the glass. Since nucleation follows an Arhenius Law, nucleating at higher temperatures is advantageous in obtaining a uniformly fine grain sized microstructure. Second stable carbide and boride phases may serve as inoculation sites and promote uniform nucleation.

In this study, titanium was found to cause large increases in the crystallization temperature of the 2-14-1 phase. Small amounts of titanium or carbon both cause a large increase in the energy product on crystallization. However, if larger amounts of these elements are added by themselves, the energy product remains low due to the formation of soft magnetic phases. Excess Ti binds B an causes the formation of the 2-17 phase. Excess C forms neodymium carbide, reducing the amount of 2-14-1 phase and causing the precipitation of free iron. When titanium and carbon are added together, high crystallization energy products are obtained even when large amounts (12 at% Ti+C) are added. This is due to the formation of titanium carbide which is found to have no detrimental effect to either the nucleation of the 2-14-1 or the resulting magnetic properties. The addition of excess amounts of Ti and C is self regulating in the respect that the amount dissolved in the glass is dependant on the maximum liquid solubility.

GENERAL CONCLUSIONS

Compound additions of Group IVA, VA, and VIA transition metals with carbon were added to a base alloy which was stoichiometric $Nd_2Fe_{14}B$. Transition metal carbide formation was found for the group IVA (TiC, ZrC, and HfC) and group VA (VC, NbC, and TaC) transition metals alloys. Carbide formation did not occur in the group VIA alloys. Besides carbide formation, the alloying ability of each transition metal carbide system was graded using four criteria. The criteria dealt with carbide formation and phase stability, liquid and equilibrium solid solubility, and high temperature carbide stability. The Group IVA transition metal carbide alloys satisfied the proposed alloying criteria and were found to be excellent additions. The Group VA alloys while forming carbides only partially satisfied the proposed alloying criteria and their use as alloying additions should be limited to optimization of magnetic properties. Finally, the Group VIA alloys did not form transition metal carbides.

From all of the available data, a transition metal carbide system needed to be chosen for further study. The Group IVA alloying additions had the most promising alloying characteristics. They satisfied virtually all of the alloying criteria and had the additional advantage of forming binary carbides with only one type of stoichiometry with a TM/C ratio of 1 to 1. From this group, TiC was chosen as the best transition metal carbide system for further study. It had the lowest atomic weight which means that more precipitates could be formed for a given weight of addition. Furthermore, it gave the highest levels of measured energy product crystallized from the glass and maintained the highest level of energy product after the 950°C anneal. TiC precipitates were found in the ribbon heat treated at 750°C for one hour. After a 950°C for one day anneal, the average grain size in the TiC alloy was much smaller (117 nm less) when compared to the base

alloy. Abnormal grain growth is found to be an important mechanism for obtaining coercivity in samples with an otherwise large average grain size.

Next, a more extensive study was launched on determining the phase stabilities and the alloy chemistry of titanium, carbon, and titanium with carbon additions. This study was done with ingots since the scale of the microstructure was large and could be easily studied with the SEM. Since the alloy chemistry will be the same, the results could then be related to melt-spun ribbons which have a microstructure on a much finer scale. When titanium was added alone to melt-spun ribbons, titanium borides were formed. In the X=6 Ti alloy, the titanium essentially reacted with all of the boron leaving only Nd_2Fe_{17} phase. In the titanium with carbon alloys, titanium carbides are formed. Thus, in the Nd-Fe-B-Ti-C system, it was found that even though the binary TiB_2 phase is more stable than the binary TiC phase, TiC nevertheless forms in the 2-14-1 system. Phase formation in a multicomponent system is achieved only through a balance of free energies, and the formation of TiC is indicative of the low stability of the $Nd_2Fe_{14}C$ phase.

Depending on composition, the transition metal carbide or boride precipitates are found to form at high temperatures in the liquid, during cooling after solidification, and during heat treatment. The precipitates form on grain or phase boundaries. The titanium carbides typically formed as discrete particles while the titanium borides formed generally in a globular bunched up fashion. After a homogenization heat treatment, the equilibrium solubilities of Ti and Ti with C in the $Nd_2Fe_{14}B$ phase were found to be 0.47 wt% and $<= 0.06$ wt% respectively. Both the carbides and the borides are found to have excellent high temperature stability and resist coarsening and dissolution at least to 1000°C.

Next, an investigation was launched to understand the solubility of titanium with carbon in the $Nd_2Fe_{14}B$ system. Discerning the solubility is inherent to understanding the alloying and precipitation processes. This solubility study included the liquid and solid

solubilities as well as the equilibrium and nonequilibrium solubilities. Samples processed by ingot casting and melt-spinning were examined. In ingots, the solubilities were directly measured using semiquantitative EDS analysis in the SEM. In melt-spun ribbons changes in intrinsic properties along with microstructural work in the Auger and TEM microscopes was used. The solubility limit of titanium and carbon in the liquid phase was found to be between X=2 to X=3 (4 to 6 at% Ti+C). Once the solubility limit of the liquid was exceeded, primary TiC precipitates formed in the liquid at high temperatures. The maximum solid solubility was found to equal the liquid solubility. The solid solubility was found to be cooling rate dependant with more transition metal dissolved in the melt-spun ribbons then in the as-cast ingots. The cooling rate dependance indicates the titanium and carbon exist in a supersaturated solid solution. The equilibrium solubility in the 2-14-1 phase was found to be less than or equal to 0.06 wt% Ti in homogenized ingots. In samples observed in the TEM, the effects of interaction volume and background intensity was minimized allowing a more accurate measure of the lower limits of solubility. Titanium could not be found anyplace in the 2-14-1 grains indicating that the equilibrium solubility limit is extremely low and below the detectability limits using EDS and PEELS.

Since the TiC additions have significant liquid solubility, and significant nonequilibrium solid solubility in the 2-14-1 and glass phases, a study was launched to investigate the changes in the intrinsic properties occurring with titanium and carbon dissolution. In order to evaluate the effects of each portion of the additions on the solidification behavior of $Nd_2Fe_{14}B$, a base alloy was modified with elemental additions of Ti or C and a compound addition of Ti with C. For each alloy, a series of wheel speed runs were undertaken. From this, the optimum wheel speeds and optimum energy products were determined. On the BHmax versus wheel speed plots, regions were identified in order to analyze the changes in phase formation brought about from the alloy

modifications. The compilation of the regional data of the modified alloys showed their effects on altering the cooling rate dependence of phase formation. It was found that the regions of properitectic iron formation, glass formation, and the optimum cooling rate could be changed by more than a factor of two through appropriate alloying additions. The effects of the alloy modifications can be visualized in a convenient fashion through the use of a model CCT diagram. The model CCT diagram was developed through general knowledge and from the experiments contained in this section. It represents phase formation during the solidification process under continuous cooling conditions for a wide range of cooling rates from rapid solidification to equilibrium cooling.

Since TiC additions were found to enhance the GFA of the base alloy, an investigation was launched to study this phenomenon in more detail. X-ray diffraction, magnetic measurements, and differential scanning calorimetry of as-quenched melt-spun ribbons indicate increasing enhancement of GFA with increasing amounts of TiC. The limit of the glass formation range and the amount of glass formed at a particular cooling rate also increased with TiC addition. Enhanced GFA was concurrent with changes in the intrinsic properties of the glass. The crystallization temperature as well as the transformation rate of crystallization was raised by TiC addition. The intrinsic magnetic properties of the glass were changed with reductions in saturation magnetization and Curie temperature (T_C) with increasing amounts of TiC addition. The intrinsic glass changes were related to changes in the local short range order of the glass. The trends in the intrinsic glass properties indicate that titanium and carbon dissolution are reducing the free volume by increasing the packing efficiency. These changes in local structure of the glass increase the glass stability which means that less undercooling is needed to prevent crystallization. Thus, at a particular cooling rate, a higher percentage of glass will be formed and the GFA is increased.

Next, the effects of Ti, C, and TiC on the crystallization characteristics of the amorphous phase was investigated. It was found that the as-crystallized energy product can be more than doubled over the base alloy. Two factors are attributed to this increase. First by raising the crystallization temperature through titanium additions, an increase in the nucleation rate of the hard magnetic phase occurs which resulted in a finer and more uniform grain size. Secondly, stable carbide and boride phases may serve as inoculation sites which promote uniform nucleation. In order to obtain high as-crystallized energy products, the alloying additions should have only nonequilibrium solubilities in the 2-14-1 phase and must not cause an overall reduction in the amount of hard magnetic phase or cause the formation of other soft magnetic phases.

BIBLIOGRAPHY

[1] William Scoresby, Magnetical Investigations, Longman, Brown, Green and Longmans, London, 1844, 35.

[2] C.D. Graham, Conference on Properties and Applications of Magnetic Materials, Illinois Institute of Technology, Chicago, 1987.

[3] William A. Cassidy, A Short Course on Permanent Magnet Materials, SJL Publishing Company, Hanna, IN., 1993.

[4] S.V. Vonsovskii, Magnetism, Vol.1, John Wiley and Sons, New York, 1974.

[5] Umberto Russo and Francesca Capolongo, Supermagnets Hard Magnetic Materials, Chap. 2, Kluwer Academic Publishers, Dordrecht, Netherlands, 1991.

[6] D. Hadfield, Permanent Magnets, John Wiley and Sons, New York, 1962.

[7] Rollin J. Parker, Advances in Permanent Magnetism, John Wiley and Sons, New York, 1990.

[8] K.H.J. Buschow and E.P. Wohlfarth, Ferromagnetic Materials, Elsevier Science Publishers, New York, 1988.

[9] David Jiles, Introduction to Magnetism and Magnetic Materials, Chapman and Hall, New York, 1991.

[10] J.F. Herbst, Review of Modern Physics, 63(1991), 819-897.

[11] Arthur L. Robinson, Science, 223(1984), 920-922.

[12] B.N. Das and N.C. Koon, Metall. Trans. A, 14(1983), 953-961.

[13] N.C. Koon and B.N. Das, J. Appl. Phys., 55(1984), 2063-2066.

[14] C.D. Fuerst and E.G. Brewer, J. Appl. Phys., 73(1993), 5751-5756.

[15] Masato Sagawa, Satoshi Hirosawa, Hitoshi Yamamoto, Setsuo Fujimara, and Yutaka Matsuura, Jap. J. App. Phys., 26(1987), 785-800.

[16] Ying-chang Yang, Xiao-dong Zhang, Lin-shu Kong, Qi Pan, Yong-tian Hou, Shuang Huang, Liu Yang, and Sen-lin Ge, J. Less Common Met., 170(1991), 37-44.

[17] J.M.D. Coey and H. Sun, J. Magn. Magn. Mater., 87(1990), L251.

[18] Y.Z. Wang and G.C. Hadjipanayis, J. Appl. Phys., 70(1991), 6009-6011.

[19] L. Withanawasam, G.C. Hadjipanayis, Robert F. Krause, "Enhanced Remanence in Isotropic Fe-Rich Melt-Spun Nd-Fe-B Ribbons", in 38th Annual Conference on Magn. Magn. Mater., Nov. 1993.

[20] V. Panchanathan, "Microstructure of High Remanence Nd-Fe-B Magnets with Reduced Rare Earth Content", in 38th Annual Conference on Magn. Magn. Mater., Nov. 1993.

[21] K.G. Knoch, G. Schneidner, J. Fidler, E.-Th Henig, H. Kronmüller, IEEE Trans. Magn., 25(1989), 3426-3436.

[22] J.F. Herbst, J.J. Croat, F.E. Pinkerton, and W.B. Yelon, Physical Review B, 29(1984), 4176-4178.

[23] R. Grössinger, R. Krewenka, X.K. Sun, R. Eibler, H.R. Kirchmayr and K.H.J. Buschow, J. Less Common Met., 124(1986), 165.

[24] N.C. Koon and R. Hasegawa, "Rapidly Solidified Crystalline Magnetic Alloys", in Proceedings of TMS-AIME Northeast Regional Meeting, May 1985.

[25] Ph. Tenaus, H. Lemaire and F. Vial, J. Magn. Magn. Mater., 101(1991), 328-332.

[26] Andreas Hütten, JOM, March(1992), 11-15.

[27] Y. Xiao, S. Liu, H.F. Mildrum, K.J. Strnat, and A.E. Ray, J. Appl. Phys., 63(1988), 3516-3518.

[28] W. Ervens, "Comparision of Properties of Nd-Fe-B and Sm-Co Permanent Magnets", in Nd-Fe Permanent Magnets - Their Present and Future Applications, Commision of the European Communities, Oct. 1984.

[29] J. Ormerod, J. Less Common Met., 111(1985), 49.

[30] R.W. Lee, E.G. Brewer and N.A. Schaffel, IEEE Trans. Magn., Mag-21(1985), 1958-1963.

[31] Raja K. Mishra, V. Panchanathon, and John J. Croat, J. Appl. Phys., 73(1993), 6470-6472.

[32] Dudley J. Kingsnorth, Ceramic Industry, Oct.(1992), 36-41.

[33] "Magnet Accounts", JOM, 43(1993), 33.

[34] D. Howe, Supermagnets, Hard Magnetic Materials, Ch. 24, Kluwer Academic Publishers, Netherlands, 1991.

[35] "Permanent Magnets-Nd-Fe-B and Ceramic Hard Ferrites Continue to Grow", Elements, Oct/Nov, 1993, 105-106.

[36] "Permanent Magnets Market to Expand", Ceramic Industry, 28(142), 28-29.

[37] C. Kittel and J.K. Galt, Solid State Physics, 3(1956), 437.

[38] B.D. Cullity, Introduction to Magnetic Materials, Addison-Wesley Publishing Company, Menlo Park, 1972.

[39] W.F. Brown, Jr., Rev. Mod. Phys., 17(1945), 15.

[40] E.C. Stoner and E.P. Wohlfarth, Trans. Roy. Soc., A240(1948), 599-642.

[41] Söshin Chikazumi, J. Magn. Magn. Mater., 54-57(1986), 1551-1555.

[42] J.D. Livingston, J. Appl. Phys., 57(1985), 4137-4139.

[43] J.D. Livingston, J. Appl. Phys., 52(1981), 2544-2548.

[44] Raja K. Mishra, Mat. Res. Soc. Symp. Proc., 96(1987), 83-92.

[45] H. Kronmüller and K.-D. Durst, Concerted European Action on Magnets, Ch.5.2, Elsevier Applied Science, New York, 1989.

[46] G.C. Hadjipanayis, R.C. Dickenson, and K.R. Lawless, J. Magn. Magn. Mater., 54-57(1986), 557.

[47] F.E. Pinkerton, and D.J. VanWingerden, J. Appl. Phys., 60(1986), 3685.

[48] G.C. Hadjipanayis and A. Kim, J. Appl. Phys., 63(1988), 3310.

[49] K.-D. Durst and H. Kronmüller, J. Magn. Magn. Mater., 68(1987), 63.

[50] H. Kronmüller, K.-D. Durst, and M. Sagawa, J. Magn. Magn. Mater., 74(1988), 291.

[51] J.D. Livingston, IEEE Trans. on Magn., Mag-23(1987), 2109-2113.

[52] F.E. Pinkerton, Mat. Res. Soc. Proc., 96(1987), 66.

[53] Tom E. Scott, "Structure and Properties of Steels", Department of Metallurgy, Iowa State University, 1975.

[54] Howard E. Boyer and Timothy L. Gall, Metals Handbook, Desk Edition, ASM, USA, 1985.

[55] R. Ramesh, G. Thomas, and B.M. Ma, MRS, 11(1989), 35-51.

[56] Shao-Xiong Zhou, P. Johansson, S.J. Savage, and Li-Ya Cui, IEEE Trans. Magn., 26(1990), 1739-1741.

[57] N. Yoshikoma, Y. Kasai, T. Watanabe, and S. Shibata, J. Appl. Phys., 69(1991), 6049-6051.

[58] K. Ohmori, Lin Li, and C.D. Graham, Jr., IEEE Trans. Magn., 28(1992), 2139-2141.

[59] Louis E. Toth, Transition Metal Carbides and Nitrides, Academic Press, New York, 1971.

[60] Edmond K. Storms, The Refractory Carbides, Academic Press Inc., New York, 1967.

[61] David R. Lide, Handbook of Chemistry and Physics, 71st Ed., CRC Press, Ann Arbor, 1990.

[62] T. Ya Kosolopova, Carbides, Properties, Production, and Applications, Plenum Press, New York, 1971.

[63] J.J. Croat and J.F. Herbst, MRS Bulletin, June(1990), 37-40.

[64] H.A. Davies, Rapidly Quenched Metals III, The Metals Society, London, 1978, 1-21.

[65] J.H. Hinken, Superconductor Electronic Fundamentals and Microwave Applications, Springer-Verlag Publishers, USA, 1989.

[66] John Clarke, "SQUIDS: Principles, Noise, and Applications", Ch.2, Superconducting Devices, Academic Press Inc., New York, 1990.

[67] Princeton Applied Research Model 4500, Instruction manual, EG&G Instruments, 1-6.

[68] Anthony Arrot, Physical Review, 108(1957), 1394-1396.

[69] E. Fuchs, H. Oppolzer and H. Rehme, Particle Beam Microanalysis Fundamentals, Methods, and Applications, VCH Publishers, New York, 1990.

[70] James W. Robinson, Undergraduate Instrumental Analysis, 3rd Ed., Marcel Dekker Publishers, New York, 1982.

[71] B.D. Cullity, Elements of X-Ray Diffraction, 2nd Ed., Addison-Wesley Publishing Company, Menlo Park, Ca, 1978.

[72] Raja K. Mishra, Earl G. Brewer, and Robert W. Lee, J. Appl. Phys. 63(1988), 3528-3530.

[73] C.S. Pande and S.P. Marsh, JOM, Sept.(1992), 25-29.

[74] Shiun Ling and Michael P. Anderson, JOM, Sept.(1992), 30-36.

[75] William F. Smith, Structure and Properties of Engineering Alloys, McGraw-Hill Publishing Company, New York, 1981.

[76] E.C. Bain and H.W. Paxton, Alloying Elements in Steel, 2nd Ed., American Society for Metals, Metals Park, OH., 1966.

[77] W.B. Morrison, J. Iron Steel Inst., 201(1963), 317.

[78] T. Gladman, JOM, Sept.(1992), 21-24.

[79] E.O. Hall, Proc. Phys. Soc., B64(1951), 747.

[80] N.J. Petch, J. Iron Steel Inst., 174(1951), 25.

[81] F.E. Pinkerton, Int. J. Powder Metal., 25(1989), 86.

[82] K.D. Durst and H. Kronmüller, J. Magn. Magn. Mater., 59(1986), 86.

[83] F.E. Pinkerton, Mater. Res. Soc. Symp. Proc., 96(1987), 65-81.

[84] C.J. Yang and R. Ray, J. Appl. Phys., 63(1988), 3525-3527.

[85] Y. Kitano, J. Shomomura, and M. Shimotomai, J. Appl. Phys., 69(1991), 6055-6057.

[86] Choong Jin Yang and Ranjan Ray, JOM, Sept.(1989), 42-45.

[87] P. Schrey, J. Magn. Magn. Mater., 73(1988), 260.

[88] W. Rodewald and P. Schrey, J. Magn. Magn. Mater., 83(1990), 206-208.

[89] T.W. Capehart, R.K. Mishra, and F.E. Pinkerton, J. Appl. Phys., 73(1993), 6476-6478.

[90] Howard E. Boyer and Timothy L. Gall, Metals Handbook, Desk Edition, ASM, USA, 1985.

[91] Y.L. Chen, IEEE Trans. Magnet., Mag-21(1985), 1967-1969.

[92] Lin Li, D.E. Luzzi, and C.D. Graham Jr., J. Appl. Phys., 70(1991), 6459-6461.

[93] R. Ramesh and G. Thomas, J. Appl. Phys., 67(1990), 6968-6975.

[94] R. Ramesh, G. Thomas, and B.M. Ma, J. Appl. Phys., 64(1988), 6416-6422.

[95] Tang Weizhong, Zhou Shouzeng, and Hu Bing, J. Magn. Magn. Mater., 94(1991), 67-73.

[96] A. Manaf, M. Leonowicz, H.A. Davies, and R.A. Buckley, J. Appl. Phys., 70(1991), 6366-6368.

[97] Janaf Thermochemical Tables, David R. Lide Jr., 3rd edition, American Chemical Society and the American Institute of Physics, 14(1985).

[98] George F. Comstock, Titanium in Iron and Steel, The Engineering Foundation, New York, 1955.

[99] George F. Comstock, Titanium in Steel, Pitman Pub. Corp., New York, 1949.

[100] H. Sandberg, Scandinavian Journal of Metallurgy, 2(1973), 233-241.

[101] Xing Feng and Ho Wen Wang, J. Magn. Magn. Mater., 94(1991), 49-52.

[102] Andreas HÜtten, JOM, March(1992), 11-15.

[103] Witold W. Cias, Phase Transformation Kinetics and Hardenability of Medium-Carbon Alloy Steels, Climax Molybdenum Company.

[104] E.C. Bain and H.W. Paxton, Alloying Elements in Steel, 2nd Ed., ASM, 1966.

[105] R.E. Reed-Hill, Physical Metallurgy Principles, 2nd Ed., Litton Educational Publishing, 1973.

[106] J.J. Croat and J.F. Herbst, MRS Bulletin, June(1988), 37-40.

[107] H.A. Davies, Rapidly Quenched Metals III, The Metals Society, London, 1978, Vol.1, 1-21.

[108] Masato Sagawa, Satoshi Hirosawa, Hitoshi Yamamoto, Setsuo Fujimura, and Yutaka Matsuura, Jap. J. Appl. Phys., 26(1987), 785-800.

[109] H.H. Stadelmaier, N.A. Elmasry, N.C. Liu, and S.F. Cheng, Materials Letters, 2(1984), 411-415.

[110] F.E. Pinkerton, Int. J. Powder Metall., 25(1989), 29-35.

[111] Raja K. Mishra, J. Magn. Magn. Mater., 54(1986), 450-456.

[112] J. Holc, S. Besenicar, and D. Kolar, J. Mater. Science, 25(1990), 215-219.

[113] Gerhard Schneider, Ernst-Theo Henig, Frank D. Missel, and Günter Petzow, Z. Mettalkde, 81(1990), 322-329.

[114] Adalbert Feltz, Amorphous Inorganic Materials and Glasses, Akademie-Verlag, Berlin, 1993.

[115] Raja K. Mishra, Tsung-Yao Chu, and L.K. Rabenberg, J. Magn. Magn. Mater., 84(1990), 88-94.

[116] V. Panchanathan, A.T. McMullen, and J.J. Croat, M. Doser, and R.W. Ribitch, J. Appl. Phys., 70(1991), 6465-6467.

[117] P.R. Sahm, H. Jones, and C.M. Adam, Rapid Solidification Materials and Technologies, Martinus, Nijhoff Publishers, Boston, 1986.

[118] S.R. Elliot, Physics of Amorphous Materials, The Pitman Press Limited, Great Britain, 1983.

[119] N.C. Koon and B.N. Das, Appl. Phys. Lett., 39(1981), 840-842.

[120] N.C. Koon, C.M. Williams, and B.N. Das, J. Appl. Phys.,52(1981), 2535.

[121] D.J. Branagan and R.W. McCallum, to be published.

[122] B.X. Gu, H.R. Zhai, and B.G. Shen, J. Magn. Magn. Mater., 97(1991), 40-44.

[123] Shen Bao-gen, Yang Lin-yuan, Guo Hui-qun, and Yang Fu-ming, J. Magn. Magn. Mater., 107(1992), 2021-2022.

[124] K.H.J. Buschow, D.B. De Mooij, and H.M. Van Noort, J. Less-Common Met., 125(1986), 135-146.

[125] Z. Altounian and D.H. Ryan, Materials Science and Engineering, 99(1988), 157-159.

[126] W.B. Muir, Z. Altounian, Tu Guo-hua, and Chen Wan-rong, J. Magn. Magn. Mater., 81(1989), 168-172.

[127] Shen Bao-gen, Ding Jun, Gu Ben-xi, Zhang Zhi-ying, H. Homborg, Zhao Jian-gao, and S. Methfessel, J. Magn. Magn. Mater., 92(1990), 53-58.

[128] B.X. Gu, B.G. Shen and H.R. Zhai, Phys. Stat. Sol. A, 117(1990), 283-289.

[129] L.X. Liao, and Z. Altounian, J. Appl. Phys., 66(1989), 768-771.

[130] P.H. Gaskell, Nature, 289(1981), 474-476.

[131] J.F. Herbst, J.J. Croat, F.E. Pinkerton, and W.B. Yelon, Physical Review B, 29(1984), 4176-4178.

[132] Anthony Arrot, Physical Review, 108(1957), 1394-1396.

[133] H.A. Davies, Rapidly Quenched Metals III, The Metals Society, London, 1978, Vol.1, 1-21.

[134] M.T. Clavaguera-Mora, M.D. Baro, S. Surinach, and N. Clavaguera, J. Mater. Res., 5(1990), 1201-1206.

[135] S. Surinach, M.D. Baro, M.T. Clavaguera-Mora, and N. Clavaguera, J. Non-Cryst. Solids, 58(1983), 209-217.

[136] Yan Xu, W.B. Muir, and Z. Altounian, J. Magn. Magn. Mater., 82(1989), 43-47.

[137] B.W. Corb and R.C. O'Handley, Physical Review B, 31(1985), 7213-7218.

[138] B.W. Corb, R.C. O'Handley, and N.J. Grant, Physical Review B, 27(1983), 636-641.

[139] Shen Bao-gen, Zhang Jun-xian, Yang Lin-yuan, Guo Hui-qun and Zhao Jian-gao, Mater. Scien. and Engin., A133(1991), 162-164.

[140] Jun-Xian Zhang, Bao-Gen Shen, Lin-Yuang Yang, and Wen-Shan Zhan, Phys. Stat. Sol. a., 122(1990), 651-655.

[141] B.D. Cullity, Introduction to Magnetic Materials, Addison-Wesley Publishing Company, Reading, Ma, 1972.

[142] A. Coleman, Materials Science and Engineering, 23(1976), 161-167.

[143] John L. Walter, Materials Science and Engineering, 39(1979), 95-99.

[144] C.D. Fuerst and E.G. Brewer, J. Appl. Phys., 73(1993), 5751-5756.

[145] R.W. Lee, E.G. Brewer, and N.A. Schaffel, IEEE Trans. Magn., Mag-21(1985), 1958-1963.

[146] J.J. Croat, IEEE Transactions on Magnetics, 25(1989), 3550-3554.

[147] W.B. Muir, Z. Altounian, Tu Guo-hua, and Chen Wan-rong, J. Magn. Magn. Mater., 81(1989), 168-172.

[148] C.M. Hsu and R.W. McCallum, to be published.

[149] Z.C. Zhong, X.K. Sun, Zhang Zhi-dong, Liu Wei, and Y.C. Chang, J. Less Common Metals, 170(1991), 55-61.

ACKNOWLEDGMENTS

I would like to thank first and foremost my parents; Ken and Shar Branagan for without their constant support, guidance, and advice this dissertation would not have been possible. In fact this dissertation is dedicated to them. Next, I would like to thank the rest of my family which will soon include my fiance; Kerry Bell. Her foresight, strong will, and dedication has only strengthened my own.

I have had many friends that have helped me along the way and .... I can not possibly mention them all. First, I would like to mention Dr. R.W. McCallum (Bill) for without his scientific knowledge and guidance, I would not have obtained this Ph.D. In addition, his way of dealing with others and perceptions on how the world really works helped immensely in my development as a professional. I was also strongly influenced by the teachings of Master Yong Chin Pak who teaches martial arts but more importantly self-respect, respect for others, and self confidence. Listening to Master Pak only reaffirmed my family values and his guidance allows me to walk tall in an unfriendly world.

In any job, the people that make up the work environment are very important to the success or failure. In this regards, I would like to thank Dr. M.J. Kramer (Matt) and K.W. Dennis (Kevin), who not only helped me greatly scientifically but are also good friends. I would also like to thank Patti Boone, who always knew what to do and kept things rolling right along. I have had many friends in graduate school and many fond memories but I can not thank them all. Those that especially come to mind are Dr. Jeff Shield, Brian Merkle, and Minseo Park. I will also remember the glass blowers, machinists, and facilities people, who always seemed busy yet took the time to say hello. Finally, I would like to thank my friends Dr. John Engel and Kevin Howes. We spent many days afield together in the country; fishing on ponds and hunting pheasants, ducks, turkeys, and deer.

Looking back over my graduate years, I can remember vividly all the trials and tribulations of being a graduate student; the effort involved blood, sweat, and tears and yet,.... this was the best time of my life. I feel that my graduate years were successful not merely from a scientific perspective but because I accomplished much and did not sacrifice family or friends.

This work was performed at Ames Laboratory under Contract No. W-7405-eng-82 with the U.S. Department of Energy. The United States government has assigned the DOE Report number IS-T 1719 to this dissertation.

APPENDIX A

PUBLICATIONS

Accepted:

D.J. Branagan and R.W. McCallum, "Solubility of Ti with C in the $Nd_2Fe_{14}B$ System and Controlled Carbide Precipitation", J. Alloys and Compounds, in press.

D.J. Branagan and R.W. McCallum, "Altering the Cooling Rate Dependance of Phase Formation During Rapid Solidification in the $Nd_2Fe_{14}B$ System", J. Magn. Magn. Mater., in press.

Submitted:

D.J. Branagan and R.W. McCallum, "An SEM Study of Precipitation Phenomenon in Stoichiometric $Nd_2Fe_{14}B$ Alloys Modified with Titanium and Titanium with Carbon", J. Magn. Magn. Mater., pending.

D.J. Branagan and R.W. McCallum, "The Effects of Ti, C, and TiC on the Crystallization of Amorphous $Nd_2Fe_{14}B$", J. Magn. Magn. Mater., pending.

EPILOGUE

HARD WORK DOES OPEN CLOSED DOORS

NEVERTHELESS;

***EFFICIENCY* IS THE KEY!**